# NTNU

Norwegian University of
Science and Technology

# Advanced small-scale characterization of hydrogen embrittlement in nickel and nickel alloys

## Sondre Fossheim

<u>Problem Text</u>

THE NORWEGIAN UNIVERSITY
OF SCIENCE AND TECHNOLOGY
DEPARTMENT OF ENGINEERING DESIGN
AND MATERIALS

# MASTER THESIS SPRING 2018
# FOR
# STUD.TECHN. SONDRE FOSSHEIM

**Advanced small-scale characterization of hydrogen embrittlement in nickel and nickel alloys**

*Avansert nano-skala karakterisering Av hydrogensprøhet i nikkel og nikkel legeringer*

The candidate is supposed to cut and prepare micro cantilever samples of nickel and nickel alloys. Optimization of the fibbing parameters for different alloys and composition as well as the orientations will be performed. In addition to preparation of cantilevers the candidate will be responsible in mechanical testing of cantilevers with and without hydrogen.

**Formal requirements:**
Risk assessment of experimental activities shall always be performed. Experimental work defined in the problem description shall be planed and risk assessed up-front and within 3 weeks after receiving the problem text. Any specific experimental activities which are not properly covered by the general risk assessment shall be particularly assessed before performing the experimental work. Risk assessments should be signed by the supervisor and copies shall be included in the appendix of the thesis.

The thesis should include the signed problem text, and be written as a research report with summary both in English and Norwegian, conclusion, literature references, table of contents, etc. During preparation of the text, the candidate should make efforts to create a well arranged and well written report. To ease the evaluation of the thesis, it is important to cross-reference text, tables and figures. For evaluation of the work a thorough discussion of results is appreciated.

The thesis shall be submitted electronically via DAIM, NTNU's system for Digital Archiving and Submission of Master's theses.

Afrooz Barnoush

Professor/Supervisor

NTNU
Norges teknisk-
naturvitenskapelige universitet
Institutt for produktutvikling
og materialer

# Preface

This report is written as a partial requirement for a Master's degree in Mechanical Engineering at the Norwegian University of Science and Technology (NTNU). The thesis is conducted at the Department of Engineering Design and Materials. The report serves as a documentation of the performed work.

Extensive work has been put into sample preparation as well as fabrication and fracture testing of microcantilevers to study the mechanisms of hydrogen embrittlement. A large number of cantilevers have been produced during this project, but due to the project's timeframe, it was not possible to test all of them. The experimental work reported in this thesis has been conducted with guidance from professor Afrooz Barnoush and Ph.D. candidate Tarlan Hajilou.

During the project, there have been some delays in the cantilever fabrication due to downtime of the Focused Ion Beam at the NTNU NanoLab. Furthermore, the availability of the Focused Ion Beam has also been limited due to its high demand.

I had the pleasure of guiding and teaching a total of 8 intern students from different universities in Europe while I was working on the project. This was a great opportunity to introduce other students to nanotechnology and hopefully contribute to an increased interest in the nanomechanical testing of microcantilevers.

A risk assessment of the planned work was mandatory and is presented in Appendix A: Risk assessment.

# Abstract

The demand for high strength materials is increasing in the modern industrial development. With more challenging applications and extreme environments, it is essential that materials are able to meet capacity and safety requirements. Due to their high corrosion resistance and higher strength at high and low temperatures, nickel-based alloys (Ni-based alloys) have particularly become valuable materials in demanding applications. However, the material properties of nickel can dramatically change when it is exposed to environments with hydrogen. This phenomenon is known as hydrogen embrittlement (HE) and is a type of deterioration which can be associated with corrosion. The ingress of hydrogen can seriously reduce the ductility and load-bearing capacity of the material, causing cracking and brittle fracture at stresses below the yield stress. HE has long been an area of intensive study but is still not completely understood. In particular, its detection is one of the most complicated aspects of the problem as the phenomenon affects metallic materials differently. Rapid nanotechnology development offers the opportunity to execute small-scale fracture experiments. Furthermore, the development of new nanomechanical testing methods has made it possible to observe the local effect of hydrogen in metals, which potentially can lead to an enhanced understanding of the fracture properties in the presence of hydrogen, required stress levels for crack propagation and ultimately explain the underlying mechanisms that control HE.

The sample materials in this project include; NiS, pure Ni, solution annealed Ni725, precipitation hardened Ni725, over aged Ni725 and solution annealed Ni718. Samples were prepared by surface grinding and electropolishing. Electron Backscatter Diffraction (EBSD) analysis of each sample surface was conducted to determine crystal orientations and grain boundary (GB) types. Subsequently, preferred sites on the sample surface were selected and a Focused Ion Beam (FIB) was utilized to fabricate a number of 6, 8 or 10 microcantilevers on each sample, either to include a GB (bi-crystalline cantilevers) or within grains (single-crystalline cantilevers), with dimensions of approximately 3x3x14μm. Microcantilevers were loaded in a controlled manner to obtain load-displacement data by utilizing a Hysitron TI950 TriboIndenter. Hydrogen enhanced cracking along GB was studied in NiS and pure Ni by performing bi-crystalline microcantilever bending tests in air and during cathodic charging. Bending tests were also performed on precipitation hardened Ni725 single-crystalline microcantilevers, but only in air. After the bending tests, high-resolution Scanning Electron Microscope (SEM) imaging was performed to evaluate the crack propagation path.

Fracture did not occur for BC NiS cantilevers tested in air, but cracks propagated along the GB plane, suggesting that there is a critical amount of sulfur (S) segregants in the GB. S segregation to the GB causes a reduction in the GB's cohesive strength, which will reduce the stress needed for intergranular failure below the stress needed to operate GB dislocation sources i.e. transgranular failure. For all NiS cantilevers charged by H, it was clearly shown that the presence of H causes HE by promoting crack initiation and crack propagation along the GB, as the bending tests resulted in a complete opening of the GB. With increasing amounts of H present in the GB, the intergranular failure is accelerated. It is therefore proposed that H accommodates the transition from ductile to brittle cracking along GBs. However, since the H-charged pure Ni cantilevers did not exhibit intergranular failure, it is found that the H-induced intergranular brittleness is strongly dependent on the amount of impurities segregated to the GB. There exists a synergetic relationship between S and H leading to GB decohesion, and when there is a critical amount of either S or H present in the GB the intergranular cracking will be accelerated. Thus, when GBs are involved, the H-enhanced decohesion (HEDE) mechanism is presumably the most relevant among the proposed mechanisms for H-assisted cracking.

# Sammendrag

Etterspørselen av materialer med høy styrke øker i den moderne industrielle utviklingen. Ettersom applikasjoner blir mer teknisk utfordrende og miljøer mer ekstreme, er det viktig at materialer er i stand til å oppfylle de kapasitets og sikkerhetskrav som stilles. Nikkel (Ni) legeringer er spesielt verdifulle materialer i denne sammenhengen, på grunn av deres høye korrosjonsmotstand og tilfredsstillende styrke ved lave og høye temperaturer. På den annen side kan material egenskapene til nikkel dramatisk endres når det blir eksponert for miljøer med hydrogen. Dette fenomenet er bedre kjent som hydrogensprøhet, hvilket forverrer materialet og kan kobles til korrosjon. Inntrengingen av hydrogen i et metall kan dramatisk redusere materialets duktilitet og bærekapasitet, og kan i ytterste konsekvens føre til sprekkdannelse og sprøtt brudd ved spenningsverdier lavere enn materialets opprinnelige flytespenning. Hydrogensprøhet har lenge vært et område med intens forskning, men man har fortsatt ikke lyktes i å oppnå en helhetlig forståelse av problemet. Spesielt har karakteriseringen av fenomenet vært et svært vanskelig aspekt ved problemet, ettersom hydrogensprøhet påvirker ulike materialer på forskjellige måter. Hurtig nanoteknologi utvikling har gitt muligheten til å utføre små-skala brudd eksperimenter, og utviklingen av innovative nanomekaniske testmetoder har gjort det mulig å observere den lokale effekten av hydrogen i metaller. Dette kan potensielt føre til en økt forståelse av materialers bruddegenskaper ved hydrogens tilstedeværelse, kvantifisere spenningsnivåer som fører til sprekkvekst og forklare de underliggende mekanismene som kontrollerer hydrogensprøhet.

Prøvematerialene som har blitt behandlet i dette prosjektet inkluderer; NiS, ren Ni, solution annealed Ni725, precipitation hardened Ni725, over aged Ni725 og solution annealed Ni718. Prøvene ble fremstilt ved overflatesliping og elektropolering. Elektron tilbakespredning diffraksjons (EBSD) analyse ble utført for hver prøve for å bestemme krystallografiske orienteringer og korngrense typer. Foretrukne områder på prøveoverflaten ble deretter valgt, og en fokusert ionestråle (FIB) ble benyttet til å produsere 6, 8 eller 10 micro-bjelker på hver av prøvene, hvor bjelkene ble produsert for å inkludere en korngrense (bi-krystallisk bjelke) eller ble produsert i et korn (enkelkrystallisk bjelke), med dimensjoner på ca. 3x3x14μm. Micro-bjelkene ble belastet på en kontrollert måte for å oppnå lastforskyvningsdata ved å bruke en Hysitron TI950 TriboIndenter. Hydrogenforfremmet sprekkdannelse langs korngrenser ble studert for NiS og ren Ni ved å utføre bøye eksperimenter for de bi-krystalliske micro-bjelkene i luft og under katodisk ladning. Bøye eksperimenter ble også utført for enkelkrystalliske bjelker av precipitation hardened Ni725, men kun i luft. Etter bøye eksperimentene ble det tatt bilder av micro-bjelkene ved hjelp av et elektronmikroskop (SEM) for å kunne evaluere sprekkvekstens utbredelse.

Lasting av bi-krystalliske NiS bjelker i luft resulterte ikke i brudd, men sprekkvekst fant sted langs korngrensen, noe som tyder på at en kritisk mengde svovel (S) har segregert til korngrensen. S segregering til korngrensen forårsaker en reduksjon i korngrensens kohesive styrke. Dette vil føre til at spenningen som trengs for intergranulært brudd reduseres til et nivå som er mindre enn det spenningsnivået som trengs for å operere dislokasjonens kilder i korngrensen, dvs. transgranulært brudd. Lastingen av NiS bjelker ved hydrogen produksjon viste tydelig at tilstedeværelsen av H forårsaker hydrogensprøhet ved å fremme sprekkinitiering og sprekkvekst langs korngrensen, da bøyetestene resulterte i en fullstendig åpning av korngrensen. Med økende mengder hydrogen tilstede i korngrensen, akselereres intergranulært brudd. Det er derfor forslått at hydrogen forårsaker overgangen fra duktil til sprø sprekkvekst langs korngrenser. Siden de hydrogenladede bjelkene av ren Ni ikke viste intergranulært brudd, er det imidlertid funnet at den intergranulære sprøheten er sterkt avhengig av mengden legeringselementer som er segregert til korngrensen. Det eksisterer et synergisk forhold mellom S og hydrogen som fører til dekohesjon av korngrensen, og når en kritisk mengede av enten S

eller hydrogen er tilstede i korngrensen vil den intergranulære sprekkveksten akselereres. Dermed, når korngrensener er involvert, er antagelig hydrogenforfremmet dekohesjon (HEDE) mekanismen den mest relevante blant de foreslåtte mekanismer for hydrogen-assistert sprekking.

# List of abbreviations

| | |
|---|---|
| HE | Hydrogen Embrittlement |
| H | Hydrogen |
| HEDE | Hydrogen – Enhanced Decohesion |
| HELP | Hydrogen – Enhanced Localized Plasticity |
| AIDE | Adsorption – Induced Dislocation Emission |
| FIB | Focused Ion Beam |
| SEM | Scanning Electron Microscope |
| EBSD | Electron Backscatter Diffraction |
| TEM | Transmission Electron Microscopy |
| AFM | Atomic Force Microscopy |
| BC | Bi-Crystalline |
| SC | Single-Crystalline |
| GB | Grain Boundary |
| Ni | Nickel |
| NiS | Nickel Sulfur |
| S | Sulfur |
| Fe | Iron |
| Pd | Palladium |
| O | Oxygen |
| M | Metal |
| FCC | Face Centered Cubic |
| BCC | Body Centered Cubic |
| HCP | Hexagonal Close Packed |
| L-D | Load-Displacement |
| Hg | Mercury |
| $HgSO_4$ | Mercuric Sulfate |
| In-situ | In Situation |
| Ga | Gallium |
| IPS | Inverse Pole Figure |
| GND | Geometrically Necessary Dislocations |
| SAV | Superabundant vacancy |
| wppm | Weight Parts per Million |
| DOSE | Distribution of Site Energies |
| T-site | Tetragonal Site |
| O-site | Octahedral Site |
| ETEM | Environmental Transmission Electron Microscope |
| SFE | Stacking-Fault Energy |
| KAM | Kernel Misorientation Map |

# Table of Contents

# 1. Introduction

Hydrogen (H) is a typical and familiar interstitial element, found in a wide range of materials. Interstitial atoms have a significant impact on materials and are most often the decisive factor for the mechanical properties of metals and alloys. H is known to have a degrading effect on the fracture properties of materials, causing a dramatic reduction in ductility and load-bearing capacity. This phenomenon is therefore commonly termed hydrogen embrittlement (HE) as it can result in premature catastrophic failure. H's effect on mechanical properties of steels was first reported in 1874, and today the problems associated with HE has attracted worldwide attention as a consequence of the increasing demand for high strength alloys. So far, many scientific studies have tried to explain the driving mechanisms of this problem, but despite all the time and resources HE still remains a debated uncertainty and a costly technical challenge in many industries. HE has especially become a critical research topic in the oil and gas and petrochemical industries. Many offshore installations experience environmental H assisted cracking, due to the production of $H_2$ from cathodic protection.

The influence on mechanical properties when dissolved H interacts with the crystal lattice and crystal defects in a material is an extremely complex process. Traditionally, the effects of dissolved H on metals and alloys have been captured by conventional macroscale mechanical tests, in which the response of a macroscale sample to a mechanical load is measured. However, it is highly demanding to decouple the macroscopic tests from H absorption and transport processes. The effects of H occur in distinct locations with higher H concentrations, as the interactions of H with the lattice is a discrete localized process over time and space. Although the macroscopic tests provide important qualitative information, the fundamental understanding of the HE phenomenon demands tools and tests of higher resolution.

Due to the rapid development in nanotechnology, it has become possible to conduct small-scale fracture experiments. A Focused Ion Beam offers direct micro-and nanoscale material removal anywhere on a solid surface, making feasible the fabrication of microcantilever samples. Fracture experiments can be conducted by utilizing a nanoindenter to perform bending tests on these microcantilevers, in which a load is applied with the indenter tip at the edge of the free extremity of the microcantilever. Furthermore, by designing an electrochemical setup in combination with a nanoindentation system it is possible to perform bending tests on microcantilevers electrochemically charged by H. This provides the opportunity to test cantilevers *in-situ*, which will eliminate the possibility of H depletion during testing. Thus, the development of innovative nanomechanical testing methods makes it possible to observe the local effect of hydrogen in metals, which potentially can lead to an enhanced understanding of the fracture properties in H environments, required stress levels for crack propagation and ultimately explain the underlying mechanisms that control HE.

The present work focuses on nanomechanical fracture experiments of single-crystalline and bi-crystalline microcantilevers, in air and charged by H. The theoretical background will initially discuss the process in which H enters a metal, followed by fundamentals of material fracture and deformation of micro-sized samples. The proposed mechanisms for H-assisted failure will also be discussed. Additionally, different microcantilever fabrication methods and some theory regarding the instruments involved in the experiment will be presented. The experimental procedure is thoroughly explained in chapter 3. It will consist of the sample preparation, the selection of ideal microcantilever milling sites by utilizing Electron Backscatter Diffraction analysis, the fabrication of microcantilevers by utilizing a Focused Ion Beam and the in-situ and air bending of microcantilevers by means of a nanoindenter. The results are presented and discussed in chapter 4. Chapter 5 presents the conclusion, which is followed up by a list of proposed future work based on the microcantilever production and experimental findings in this project.

# 2. <u>Background</u>

## 2.1 Hydrogen in metals

### 2.1.1 Hydrogen Entry

The degradation of metals and alloys comes from environmental hydrogen (H) and the first stage in the process of HE is undeniably when H enters the material, an interaction occurring either in a gas phase or in a liquid phase. H is traditionally considered as an undesirable impurity in metals and alloys. Its presence is associated with the initiation of porosity and corrosion, and Hs specific behavior in different metals contributes to the worsening of the materials technological and exploitative properties. From a chemical and thermodynamic perspective, the H entry is considered as a complex process with many dependent parameters. But because of its significance in the overall HE process, this will be the main focus in the following section.

**Gas – Solid Interaction**

The most appropriate way to explain the gas-solid interaction is to define it in terms of a three-stage sequence: (1) physisorption, (2) chemisorption and (3) adsorption.

(1) Physisorption is the formation of a fluid multilayer, due to the bonding van der Waals forces between a surface and an absorbent. The reaction is characterized by being completely reversible, occurring instantaneously and with a following change in enthalpy equal to the gaseous adsorbent's heat of condensation. (2) Chemisorption involves the chemical reaction between the adsorbent molecules and the surface atoms with short-range chemical forces and is thus limited to a monolayer. It is characterized by being slowly activated and is either slowly reversible or irreversible, where the formation of a one-center polarized covalent bond between an absorbent atom or molecule and a material surface atom represents the change of enthalpy or heat of adsorption. Atomic H on transition metals is formed through dissociative chemisorption, in which the change of enthalpy reflects the bond energies of a M (metal)-H and H-H pair. It was stated that such bond energies are 276 kJ/mol for Ni-H pairs. In comparison, the Ni-Ni bond energies are approximately 70 kJ/mol, when the metal-metal bond energy is considered 1/6 of the heat of sublimation. This is a clear indication that chemisorption is essential for HE. However, there are materials which also has significantly higher M-H bond energies than M-M bond energies, without any clear signs of HE. Consequently, the dissociative chemisorption mechanism alone is not sufficient for HE. (3) Adsorption is the final step. This is where the formations from dissociative chemisorption penetrate the metal surface and diffuse into the material lattice. Whether dissolved H inside the transition metal is present as atomic H, $H^-$ or $H^+$, has long been a subject of discussion. Specifically, the discussion concerns the degree of polarization, as the reaction between H and metal lattice atoms must result in a polarized covalent bond. The hydride form is most supported, although there is still disagreement related to its charge. [1], [2].

Figure 1 shows the potential energy curve in the vicinity of a metal surface. The left side indicates the potential energy of the H gas phase and metal, $H_2 + M$, and is initially zero, while the right side represents the potential energies of H dissolved in the metal. As shown on the left side, by H dissolution in the metal, the potential energy of the metal-H system can either be lowered (exothermal reaction) or increased (endothermal reaction). The interactions between the metal surface and H are visible in the interface region. When the system's potential energy level in the metal lays below that of the H gas molecule and the metal, the H absorption occurs,

that is when the reaction is exothermal [3]. Specific H locations in the metal lattice will be discussed further in section 2.1.2 and 2.1.3.
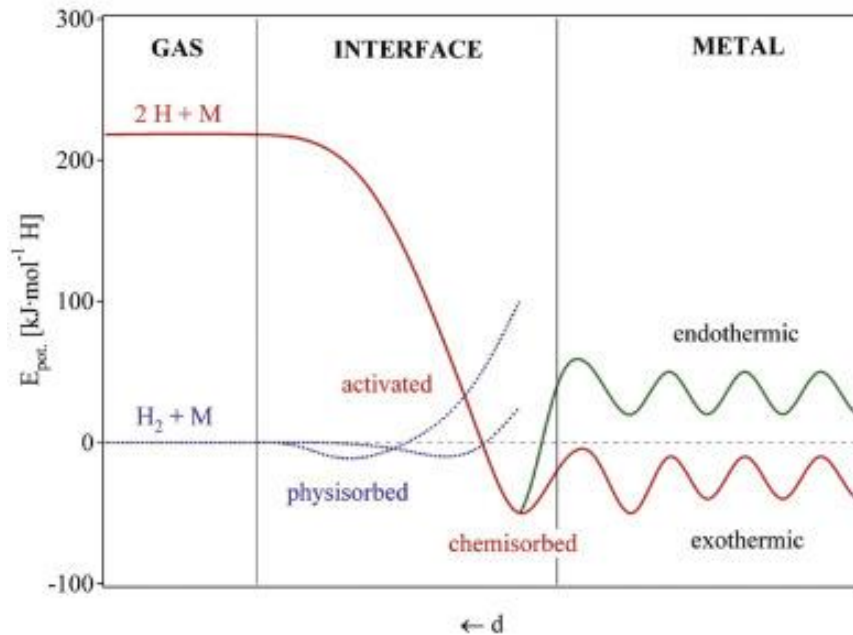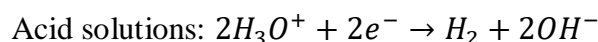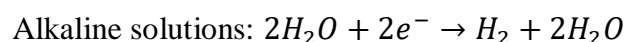


Figure 1:  Potential of H approaching a metallic surface [4].

**Solid – Hydrogen Interaction in Aqueous Environments**

The entry of H into metals are in many cases present in aqueous environments. Dissolution of steels in strong acids provokes severe H entry, due to the intense development of $H_2$. On the other hand, metallic reactions in neutral electrolytes have slower $H_2$ production but are indeed important due to their economic consequences in several industries. One of them is the oil and gas industry. The cathodic protection of high-strength steel structures in H ion rich seawater causes a reduction reaction in which $H_2$ molecules are evolved at the cathodic surface. However, the reaction between metals and neutral solutions could also occur when a metal surface is in contact with a thin layer of air-saturated water condensate. The cathodic reaction in aqueous electrolytes evolves H and the H evolution reaction depends on the type of electrolyte

$$\text{Alkaline solutions: } 2H_2O + 2e^- \rightarrow H_2 + 2H_2O$$

$$\text{Acid solutions: } 2H_3O^+ + 2e^- \rightarrow H_2 + 2OH^-$$

Due to the presence of a dense water dipole network in the electrolyte and the adsorption conflict between various elements on the metal surface, the boundary of a metal-electrolyte interaction is a much more complex and involved interface as that of a metal-gas interaction. Metal-electrolyte interfaces consist of fully and partially solvated ions and are easiest defined by a model of two plates. The metal with its surface charge represents the first while the nearest solvated ions, held together by electrostatic forces, define the other (outer Helmholtz plane). Specific adsorption occurs when an ion loses its salvation barrier and form a chemical bond with the metal surface. In the interaction, these ions cause more charge at the metal surface and a counter charge in the layer is therefore needed for charge compensation. Consequently, the interface will experience a potential drop during adsorption. A schematic representation of the interface model is shown in Figure 2 (a) and the potential drop across the interface is illustrated in Figure 2 (b). When considering the entry of H into metals in an electrolyte, the metal type becomes essential. There are several metals that can absorb H, in which an alternative reaction

path for the chemical or electrochemical desorption of H atoms is provided. The amount of H that enters into the metal is typically small compared to the total amount produced at the cathode, and its entry rate depends on several variables. The nature of the metal, composition and thermodynamic record, the surface conditions, the current density of the cathode, electrolyte composition, the potential of the electrode, pressure and temperature are all variables potentially affecting the H entry rate. [1].
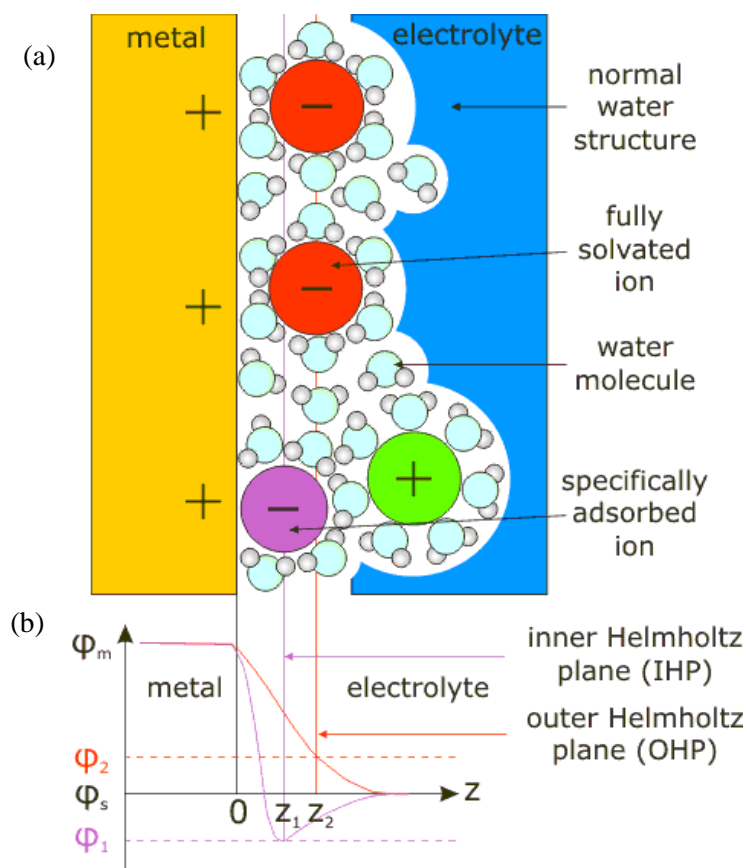


Figure 2: (a) Schematic illustration of the metal-electrolyte interface with partially and fully solvated ions. (b) Potential drop of interface with specific ion adsorption (thin line) and non-specific ion adsorption (thick line) [70].

2.1.2 Hydrogen in Perfect Metals

H is a common interstitial in metals. In the conventional crystalline host lattice, H locate at interstitial sites, due to its small size. The direct interstitial location of H is difficult to determine, due to Hs low solubility and high diffusivity in metals. Nevertheless, it is known that the commonly preferred occupancy is interstitial sites with tetragonal (T-site) and octahedral (O-site) symmetry for simple lattice structures, such as face-centered cubic (FCC), body-centered cubic (BCC) and hexagonal close-packed (HCP), shown in Figure 3. As the H atom occupies a site, the host lattice distorts in which the total energy of the system increases due to the contribution of strain energy. The size of the interstitial site therefore becomes an important indication for its occupation by H [4]. By first principles calculations for FCC, BCC and HCP Fe crystals, He Y. et al. [5] reported that FCC and HCP structures predominantly fills H at O-sites while BCC structures prefer H mainly at T-sites. Moreover, it was stated the H diffusion coefficient for the BCC crystal was higher than that of the FCC and HCP crystals and that H had higher mobility in the presence of a vacancy in the BCC Fe crystal.
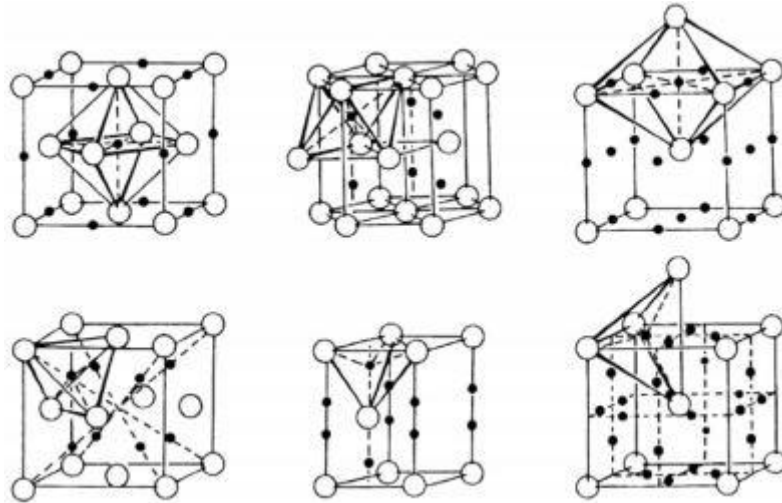
5

Figure 3: O-site and T-site for FCC (left). O-site and T-site for HCP (middle). O-site and T-site for BCC (right) [4].

Although H atoms in solid solution are common at interstitial sites of the regular lattice, these atoms usually amount for only a part of the total H atom content. However, the interstitial sites are dominating in number and control the transport and separation of H at different trap sites.

2.1.3 Hydrogen in Defective Metals

It has been stated that the solubility of H in metals also depends on their microstructure, purity and distribution of dislocations. D. S. Dos Santos and P. E. V. De Miranda [6] observed that amorphous alloys dissolve greater amounts of H in solid solution, due to their great disordered atomic structure. They also stated that H trapping defects in the metallic microstructure result in a major reduction in the H mobility. This is because H tends to diffuse to the defects and becomes bonded to them. Consequently, this effect contributes to an increased amount of dissolution sites, thus effectively increasing the H solid solubility.

Because of H atoms small size and thus their significant mobility in materials, the altering of the H-metal system properties becomes important and interesting. There are several consequences of the high H mobility in metals. However, for understanding the mechanisms of HE the most important effect is Hs ability to easily redistribute and segregate at lattice defects. The structural lattice defects of a metal are created in its thermal and mechanical processes. Compared to normal interstitial sites in the material lattice, the potential energy of H close to lattice defects is significantly reduced. This interaction gives rise to H being trapped by defects and decreasing the defects' formation energy. Each defect tends to interact with H in a specific way, and the interaction becomes critical for HE as the structures and densities of defects changes and the H concentration around defects vary. Several trap sites are shown in Figure 4, including the conventional interstitial sites as discussed in section 2.1.2. Although effects of the different trap types have been observed, the separation of the individual H effect contributions has proven to be challenging [7].
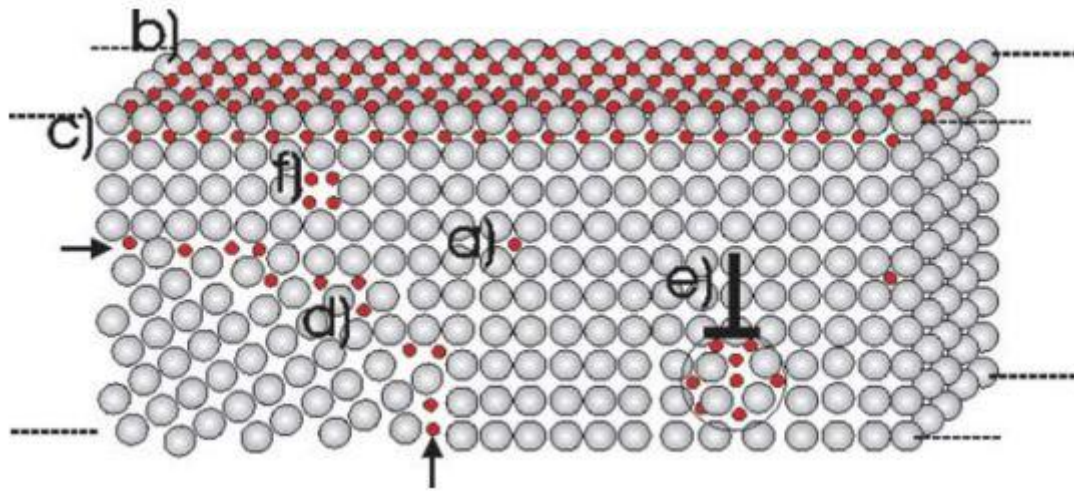
6

Figure 4: A schematic presentation of defects in a nanoscaled film and accumulation of H atoms in the low-concentration range. a) Conventional H solubility in the metal lattice. b) Surface trap sites. c) subsurface trap sites. d) Gran boundaries. e) Edge dislocations, with an expected cylindrically shaped region of H segregation. f) Vacancies [7].

### 2.1.3.1 Hydrogen Interaction with Grain Boundaries

A perfect single crystal contains sites of one energy only. By introducing a defect to a crystal and restrict the interaction with H to the nearest interstices, we obtain a two-level system. Furthermore, when going from zero- to one- and two-dimensional defects, it is realistic to expect a more diverse distribution of site energies (DOSE) rather than a distribution of just two. There is a competition for the occupancy of H between the various DOSE sites. When H occupies the sites of lowest energy, the total energy of the entire system is reduced while the entropy is increased by filling sites present in large numbers. The H segregation at GBs is recognized as central to the influence of H on mechanical behavior, and materials containing high densities of these defects have been intensively studied. However, despite all the research of these interactions a predictive understanding has not yet been reached. This is primarily because of the often imprecise and incomplete information concerning the boundary's atomic structure, which prevents quantitatively analysis of H energetics. Moreover, due to the presence of nonmetallic elements in metal GBs, such as oxide, carbide and nitride precipitates, complications of nonmetallic bonding arise. It is expected that GBs will have multiple binding energies due to their structural complexity. For boundaries with a well-defined orientational relationship it is therefore realistic to imagine a smaller number of such energies, while for interfaces of less continuity the energetics becomes more complex [7].

On the other hand, it is stated that the concept of a site energy distribution is appropriate to study the segregation of H at GBs with the concept of a two-level system. Mütschele and Kirchheim [8] suggested that a qualitative interpretation of the H concentration dependence of the diffusion coefficient becomes possible when considering that symmetric boundaries have a long-range periodic arrangement of atoms and that there will be a spectrum of site energies that can, for a polycrystalline sample containing a variety of different types of grain boundaries, be represented by a Gaussian distribution, as shown in Figure 5. The H segregation in Pd GBs was studied, and it was stated that at low H concentrations the H atoms would be trapped within the energetically deep sites of the Gaussian distribution, as the interstitial lattice offers sufficient vacancies for H. Consequently, the diffusion coefficient of the boundary becomes even lower than within the grains. With increasing H concentration, the sites of higher energy have to be occupied, and the diffusion coefficient will increase due to the decrease of the average

activation energy. In this case, the GBs provide paths for accelerated diffusion where the diffusion coefficient becomes greater than within the grains. Thus, the diffusion of interstitial H at GBs does not rely on vacancies. Arantes et al. [9] observed similar diffusion effects for H in Ni GBs, where the experimental results of GB diffusion revealed diffusion rates significantly larger than in the crystalline matrix.
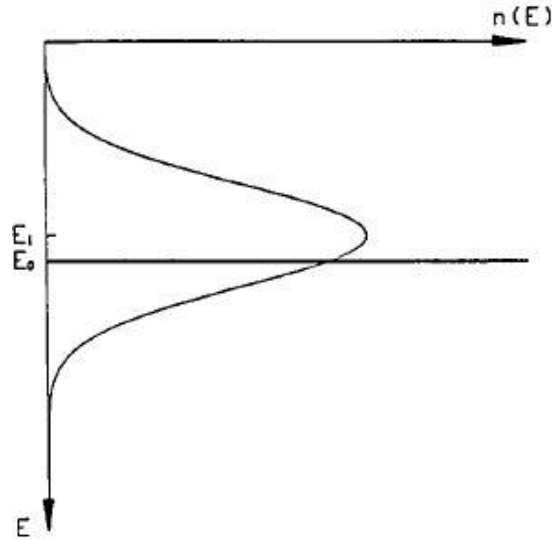


Figure 5: The proposed distribution of site energies, $n(E)$. The Gaussian distribution around $E_1$ corresponds to sites in the GB while the line $E_0$ is sites within the grains. The difference between them gives the spectrum of site/segregation energies. [8].

A. Oudriss et al. [10] investigated the effects of grain size and GBs on the diffusion and trapping of H in pure nickel (Ni). It was found that GBs were preferable sites for diffusion and trapping of H but varied with the nature of the GB. Acceleration of H diffusion along the GBs was claimed to be due to mainly high-angle GBs since they have a disordered structure, and thus diffusion becomes easier because of the large excess of free volume. Furthermore, the investigation showed that usually preferred areas for H segregation were GBs with low misorientation ($\Sigma$1) and special GB types ($\Sigma$3-$\Sigma$29). Considering their ordered structure (low-high misorientation), it was claimed that the GBs are accommodated by various defects (vacancies, dislocations) representing potential H traps, which can influence the diffusion mechanisms.

## 2.2 Micro – Failure Behavior

### 2.2.1 Brittle Fracture

A brittle fracture occurs without noticeable deformation and with rapid crack propagation. The crack motion direction is almost perpendicular to the applied tensile stress, producing a relatively flat fracture surface. Materials that fail in a brittle manner will have fracture surfaces of distinctive patterns, where any signs of gross plastic deformation will be absent. On a macroscopic level, some brittle fracture surfaces of steels may have a series of V-shaped "chevrons" markings that have been formed in the vicinity of the fracture cross-section and are pointing back to the crack initiation site. Others may contain lines or ridges that radiate from the origin of the crack in a fanlike pattern. When considering brittle fracture on a microscopic level, the crack propagation for most brittle crystalline materials corresponds to the sequential and repeated rupture of atomic bonds along specific crystallographic planes, as illustrated in Figure 6. This fracture process is commonly termed "cleavage" and is established as transgranular since the fracture cracks pass through the grains. As a result of the changes in orientation of the cleavage planes from grain to grain, the cleavage fracture is forced to re-initiate at grain boundaries in a different orientation. Consequently, the fracture surface is often characterized by a faceted texture. Crack propagation may also occur along grain boundaries, which is the case for some alloys [11], [12], [13]. The segregation of impurity elements to grain boundaries causes a weakening or embrittlement of the grain boundary regions, resulting in a reduction in ductility and toughness. This type of fracture is said to be intergranular, and its fracture surface is typically featured by the three-dimensional nature of the grains. In the initiation of a brittle fracture, the crack tip is dominated and surrounded by an annular zone of linear elastic deformation behavior. This implies that the initiation toughness will dominate the material fracture resistance with only a small portion of additional resistance to crack extension beyond crack initiation. When little energy is required to extend the crack beyond initiation, in which the sample will fail unstably, determination of the material toughness becomes problematic since no measurement of fracture resistance is possible beyond initiation [66], [67].
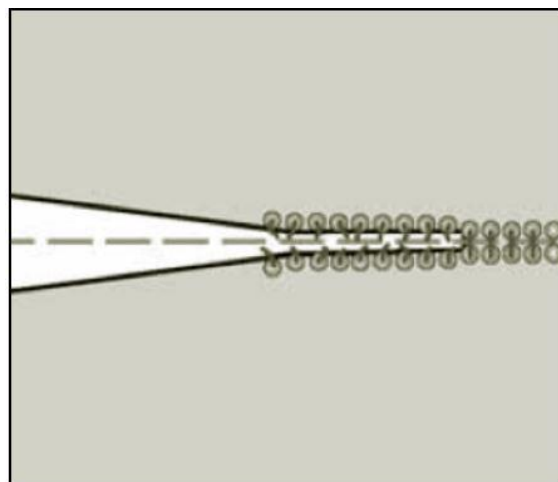

Figure 6: Cleavage fracture [69].

### 2.2.2 Ductile Fracture

In contrast to brittle fractures, the behavior of ductile fractures exhibits extensive plastic deformation. The ductile fracture process is associated with slow crack propagation where large amounts of energy is absorbed before fracture. Normally, this process occurs in several stages. First, local strains and stresses will arise at the crack tip as the sample is loaded, and at sufficient

levels cause microvoids to nucleate in the interior of the cross-section. Subsequent, with persisting deformation, the microvoids grow, congregate, and will eventually coalesce to form a crack. The microvoid coalescence process causes continuous crack growth until final fracture ensues by the rapid crack propagation. One can imagine the material as being "pulled" apart, leaving a fracture surface with an irregular and fibrous appearance. Microscopically, a ductile fracture is explained in terms of nucleation and the extension of dislocations, as illustrated in Figure 7. Its macroscopic failure mode has a continuous process of ductile tearing instead of a point fracture, in which the tearing resistance reflects the material toughness. Tough materials exhibit significant tearing resistance to incremental crack propagation. For some materials, predominantly elastic conditions may even continue to exist throughout the process. Ductile fractures are characterized by plastic deformation domination at the crack tip, and thus, the material fracture resistance increases with crack growth. [66], [67].
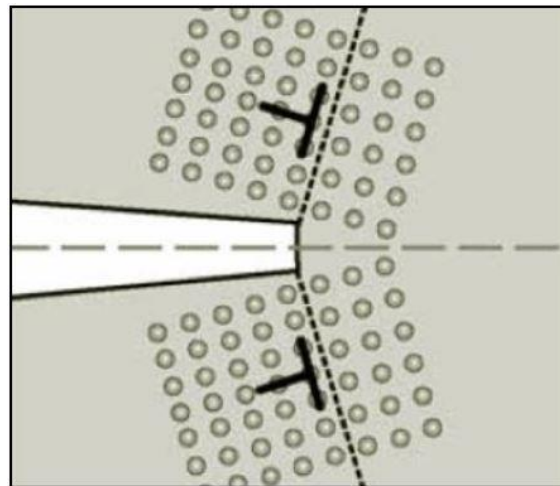


Figure 7: Ductile fracture [69].

2.2.3 FCC Deformation

The plastic deformation of metals occurs with the motion of dislocations, and the stress required to move a dislocation depends on the atomic bonding and the crystal structure. Crystalline materials exhibit inhomogeneous plastic deformation in which the deformation takes place on specific slip systems. In FCC metals slip occurs in closed-packed <110> directions within the {111} planes. The four unique {111} planes with the three independent <110> directions constitute twelve slip systems, in which several slip systems may exist for a particular crystal structure. For a polycrystalline material, slip usually occurs in the grains with favorably oriented slip systems when the resolved shear stress reaches a critical value. The difference in strain between elastic and plastic grains results in an increase in local stresses that eventually will initiate plastic deformation in the elastic grains. The development of high internal stresses can for example be a result of the formation of dislocation pile-ups at GBs. Several slip systems can be activated with increasing strain, work hardening and crystal rotation. Obstacles for dislocation motion will cause the material strength to increase as the dislocation lines are required to bow. Moreover, by decreasing the structural scale to the nano-regime, even higher stresses are required to bow dislocation lines and the material strength is increased significantly. Since the stress levels needed for dislocation motion in the nano-regime are high, small alterations in length scale or crystal orientation will significantly influence the possibility of dislocation motion at a given stress level. Therefore, as a result of the length scale distribution, smaller features will remain elastic even at noticeable applied strain levels. However, local stresses high enough to cause breaking of atomic bonds can arise from the strain difference

between plastic and elastic grains. The issue of the sample size effect will be discussed in more detail in section 2.2.4.

Internal stresses developed due to strain difference between plastic and elastic domains can cause brittle fracture in conventional single-phase metals. This occurs if the friction stress (stress required for dislocation motion) is high, recovery of dislocation substructure is difficult or if there is a shortage in the number of available slip systems. Unlike BCC metals, which significantly increases the friction stress as the temperature is decreased, conventional FCC metals do not exhibit a ductile-to-brittle transition. This is because spontaneous dislocation emission from the crack tips in FCC metals prevents the stresses to be raised to levels high enough for breakage of atomic bonds i.e. cleavage. Usually, tensile specimens of pure single-phase FCC metals fracture in a completely ductile manner. On the other hand, brittle fracture is possible for nanostructured FCC metals, even in single-phase materials. For such materials, cleavage is accommodated by two factors, (1) high stress levels needed for dislocation motion and (2) inhomogeneity of plastic deformation. The brittle fracture of FCC nanostructures will occur as a result of the difficulty in moving dislocations due to the dimensional constraint and the development of large internal stresses from the strain difference between adjacent layers and grains [14].

## 2.2.4 Sample Size Effect
The mechanical properties and behavior of metallic samples are expected to change as the sample size or the deformed volume reduces to the micrometer regime. Consequently, macroscale materials behavior may not be directly applicable to the micro – and nanoscale. Significant size effects have been observed for metallic materials with the characteristic length scale of non-uniform plastic deformation approaching the micrometer regime. In general, it is recognized that the smaller the sample size the more resistant the sample material becomes against plastic deformation. Traditional plasticity theories and their constitutive models do not hold any internal length scale and are therefore not capable to predict the size dependence of material behavior at the microscale. To gain more insight into this phenomenon, macroscopic cracking and atomic fracture have been connected through conventional plasticity theories. However, this has proven to be difficult since the conventional plasticity theories lack the ability to adequately model the stress-strain behavior at the small scale. In order to accurately describe deformation at the microscale, this highlights the necessity of a microscopic understanding of plasticity.

## 2.2.4.1 Crack Tip Plasticity
When considering the failure of metals, the stress intensity factor is a parameter of interest. However, this parameter is only fully satisfied for ideally brittle materials while most metals tend to fail after a certain amount of plastic deformation. Consequently, corrections must be applied to the linear elastic fracture mechanics as a crack tip experience moderate yielding. These corrections are simple, and it is stated that they also may be applicable to materials that exhibit small-scale yielding at the crack tip [15]. The stress intensity factor of a material also tends to become more inaccurate with increasing ductility. This is because the calculations of the stress intensity factor consider the stresses at the crack tip to be infinite, while in reality there will exist a plastic zone in the vicinity of the crack tip limiting the stresses to finite values. The plastic zone is determined by a certain radius from the crack tip, where the yield stress is exceeded and deformation initiates. Overall, plasticity significantly contributes to energy adsorption in crack propagation, which is reflected by the formation of a blunt crack tip as the crack tip deforms plastically. The blunt tip will considerably increase the amount of work needed for further crack propagation.
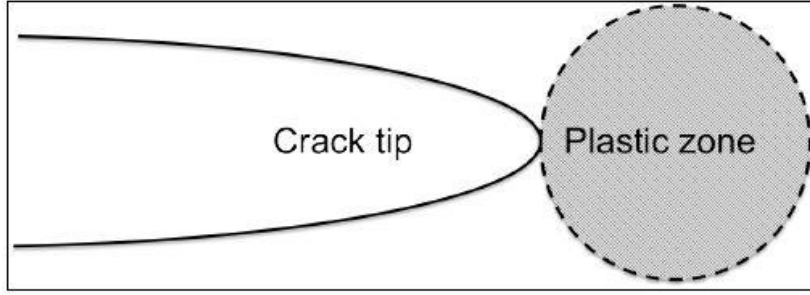
Figure 8: Plastic zone near the crack tip.

Deformation of a material in an inelastic manner, like plasticity, causes relaxation of the crack tip stresses and as the inelastic region at the crack tip increases, the elastic stress analysis becomes more inaccurate. In the plastic zone, the material carries less stress compared to the stress levels that would be present in the material if it remained elastic. The stress must redistribute when yielding occurs. Since the stress cannot exceed the yield, the forces that would be present in an elastic material cannot be carried an elastic-plastic material. Therefore, to accommodate for these forces the size of the plastic zone must increase. The size of the plastic zone can be estimated by a simple force balance and is expressed as [68]

Plane stress
$$r_p = \frac{1}{\pi}\left(\frac{K_{IC}}{\sigma_y}\right)^2 \tag{1}$$

Plane strain
$$r_p = \frac{1}{6\pi}\left(\frac{K_{IC}}{\sigma_y}\right)^2 \tag{2}$$

For an elastic, perfectly plastic material it has been shown that the material outside the plastic zone is stressed in a manner analogous to the crack being positioned in the center of the plastic zone. It is therefore possible to account for the softer material in the plastic zone by defining an effective crack length, somewhat larger than the actual crack size [68].

$$a_{eff} = a + \frac{r_p}{2} \tag{3}$$
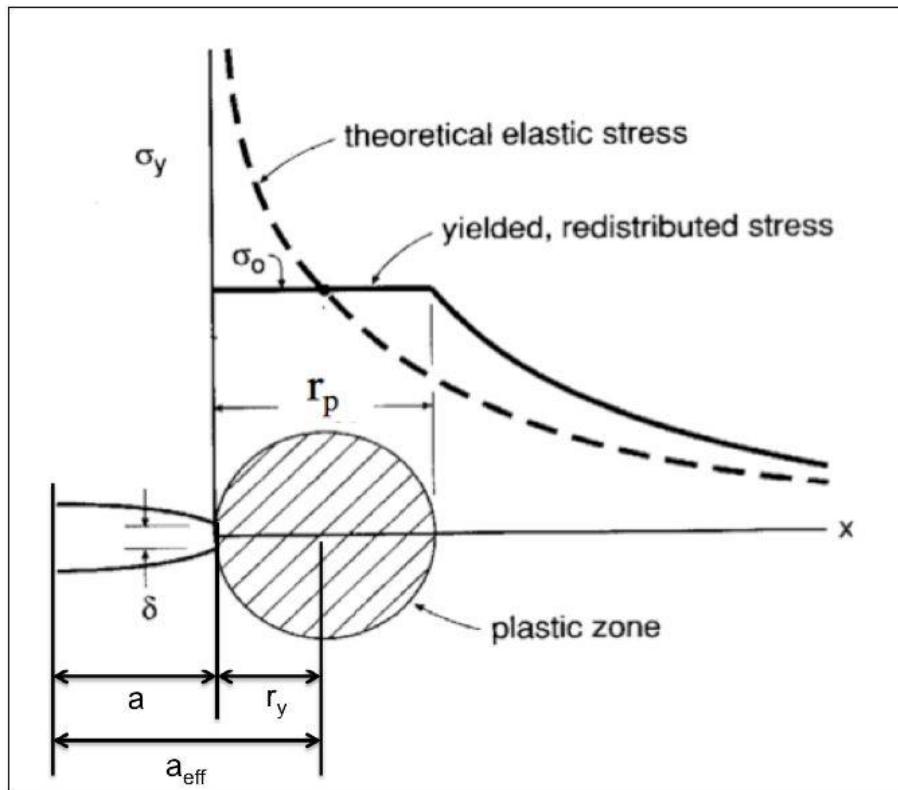
Figure 9: Plastic zone [68].

Due to the extent of plasticity, relative to the specimen dimension, the crack tip plasticity becomes more important as the sample size becomes smaller. To be able to apply linear elastic fracture mechanics, it is essential that the size of the plastic zone is much smaller than the crack length. At high stresses, plastic distortion will typically occur, which will cause the linear elastic solution to no longer be applicable close to the crack tip [49]. In cases of more extensive yielding, it is therefore necessary to utilize alternative crack tip parameters regarding non-linear material behavior.

2.2.4.2 Stress State

As a crack is advancing due to loading, stress will distribute in the vicinity of the crack tip. It is important to mention that there are three fundamental modes by which a load can operate on a crack. Each mode will effect a different crack surface displacement, where Mode I is a tensile mode, Mode II is a sliding mode and Mode III is a tearing mode. Due to the nature of the experiment in this thesis, only Mode I will be treated in the ensuing discussion. Depending on the thickness of the sample, the stress state has two extreme conditions. For a thin sample, the stresses through the thickness cannot vary substantially because of the absence of stresses normal to a free surface, and the stress state will become biaxial. An extreme condition of plane stress is therefore said to exist, where the material behaves with high plasticity since there are no out-of-plane stress components while out-of-plane deformation can be significant. At the other extreme the sample is thick, and the crack is limited by the surrounding material resulting in a triaxial stress state. This is known as the plane strain condition, where the crack tip is loaded to higher stress with little yielding, behaving in a more brittle manner. The two extreme conditions are illustrated in Figure 10.
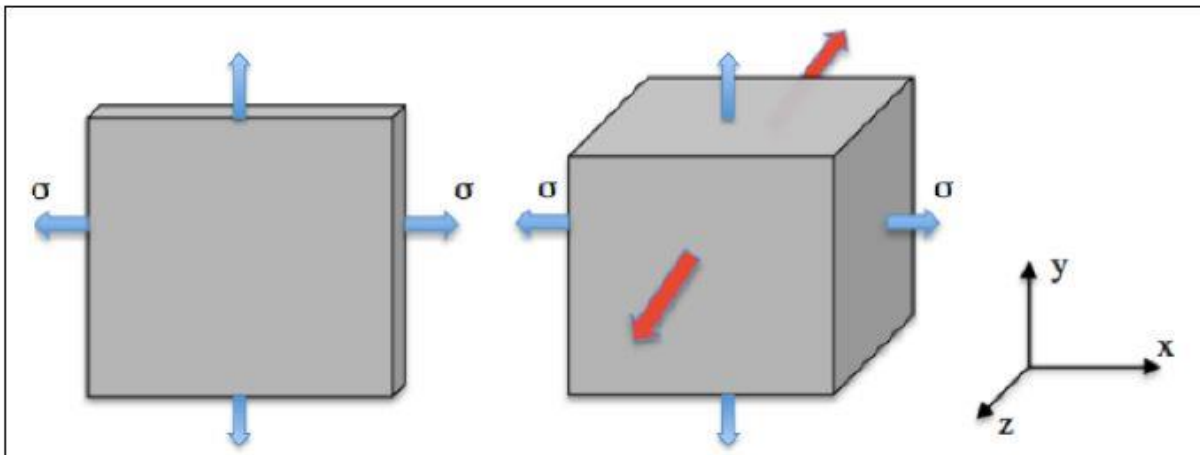
Figure 10: Left: plane stress, right: plane strain.

The stress state is often crucial for the fracture behavior. Whether the specimen is dominated by a stress state of plane strain rather than plane stress is a consequence of the critical thickness. At the sides of a thin specimen, the through-thickness directional stress must be zero since there are no normal forces working here. Since the specimen is thin there will not be enough room for the stress to reach considerable values within the material. However, for a thick specimen, the material adjacent to specimen center will behave as a constraint, disabling the lateral contraction of the material near the center. This will lead to zero strain in the through-thickness direction and a tensile stress will be present as the material is prevented from contraction.

The maximum shear stress available to drive plastic flow is reduced by the triaxial stress state at the crack tip near the center of a thick specimen. It can be claimed that the inability to contract laterally limits the mobility of the material and that the reduction in the extent of available plasticity is due to an increasing sample size. The small size of microscale samples causes the crack tip stress field to be located close to the free surfaces. At this scale, it is therefore assumed that higher order stresses do not exist.

### 2.2.4.3 Dislocation Activity

In the last few decades, it has been evident that especially the mechanical properties concerning the yield strength and flow stress changes as the deformed volume or specimen size is reduced to the microscale. The deformation mechanisms of macroscale materials may differ from that of the micro – and nanoscale, and a fundamental understanding of uniform and gradient dominated deformation at the microscale is therefore important for the successful design of small-scale materials. The strain gradient plasticity model is one of the most commonly used theories to capture a mechanical size effect at small sample sizes. This theory claims that the flow stress is not only controlled by the plastic strain, but also by the strain gradient. In the deformation field dislocations, commonly termed as geometrically necessary dislocations (GNDs), will compensate the strain gradient. Specifically, the GND is an additional storage of dislocations needed to accommodate the shape alteration as a result of any non-uniform plastic deformation. The density of the GNDs is linked to the strain gradient, where high strain gradients will result in a high dislocation density, and it can be shown that an increase in the dislocation density leads to an increase in the yield and flow stress. In other words, the presence of strain gradients in the deformation field attributes the increase in yield and flow stress of plastic deformation. For a cantilever that is being bent due to loading, a number of GNDs will emerge to accommodate the curvature. The dislocations will not contribute to plastic strain but will behave as barriers to the activity of other statically stored dislocations, thus contribute to work hardening of the material. When a non-uniform plastic deformation takes place, there will

be more storage of material defects than compared to uniform deformation at the same strain level, and when the characteristic length of deformation becomes small enough the effect of these defects becomes evident. However, since these effects are negligible at the macroscale, they would not be significant for a bending test in the millimeter regime, or above [16].

The work of Motz et al. [17] attempted to explain the size effect with a strain gradient plasticity approach. Cantilevers of different thicknesses, ranging from 7,5 to 1 µm, were milled with a focused ion beam and loaded with a nanoindenter, and the results indicated a strong size effect. Furthermore, if the deformation of the beam is assumed to be under a plane strain condition, it was stated that the strain gradient is equal to the curvature of the plastically deformed region of the beam. Figure 11 shows the existence of a simple arrangement of GNDs to accommodate strain gradient, where they assume arrays of dislocations, which perform a small amount of tilting of the crystal. A direct measurement of the strain gradient is difficult, but for the simple dislocation arrangement in Figure 11, it was claimed that there existed a direct correlation between strain gradient and the gradient of the crystal orientation. The local crystal orientation was measured after loading by utilizing electron backscattering diffraction (EBSD), and the increase in flow stress due to the GNDs was calculated. A large mismatch between the experimental results and strain gradient plasticity theory was found, and it was stated that the strain gradient plasticity model could not explain the strong dependency of the flow stress and thus the large size effect. In reality, the dislocation arrangement will be different from the simple arrangement in Figure 11. Activation of dislocation sources on more than one slip system is more likely, resulting in a complex dislocation arrangement. In this case, the number of GNDs will be higher. However, in order to explain the size effect due to an even more complex dislocation arrangement, would require an unlikely degree of dislocation density. The paper therefore suggests that the size effect can be explained by a combination of three mechanisms; strain gradient plasticity, a reduction in the number of available dislocation sources and dislocation pile-up at the center of the beam.

Figure 12 shows a more realistic dislocation distribution, where the pile-up of dislocations are in the center of the beam. To avoid complications, only one slip system is chosen. The slip system is aligned by an angle of 45° to the beam axis, which is the plane of maximum shear stress. For each slip plane, a certain number of dislocation sources are assumed, which will limit the number of active slip planes. The dislocation source works as a dislocation dipole, where one dislocation is moved to the surface of the beam forming a step, while the other dislocation is moved to the center of the beam. But since the shear stress decreases approaching the center and reverses its sign at the center, the dislocation that is moved to the center cannot move freely across the beam center. Consequently, the emitted dislocations will form a pile-up at the center, shielding the dislocation source. The bending moment (applied stress) must be increased for further deformation.
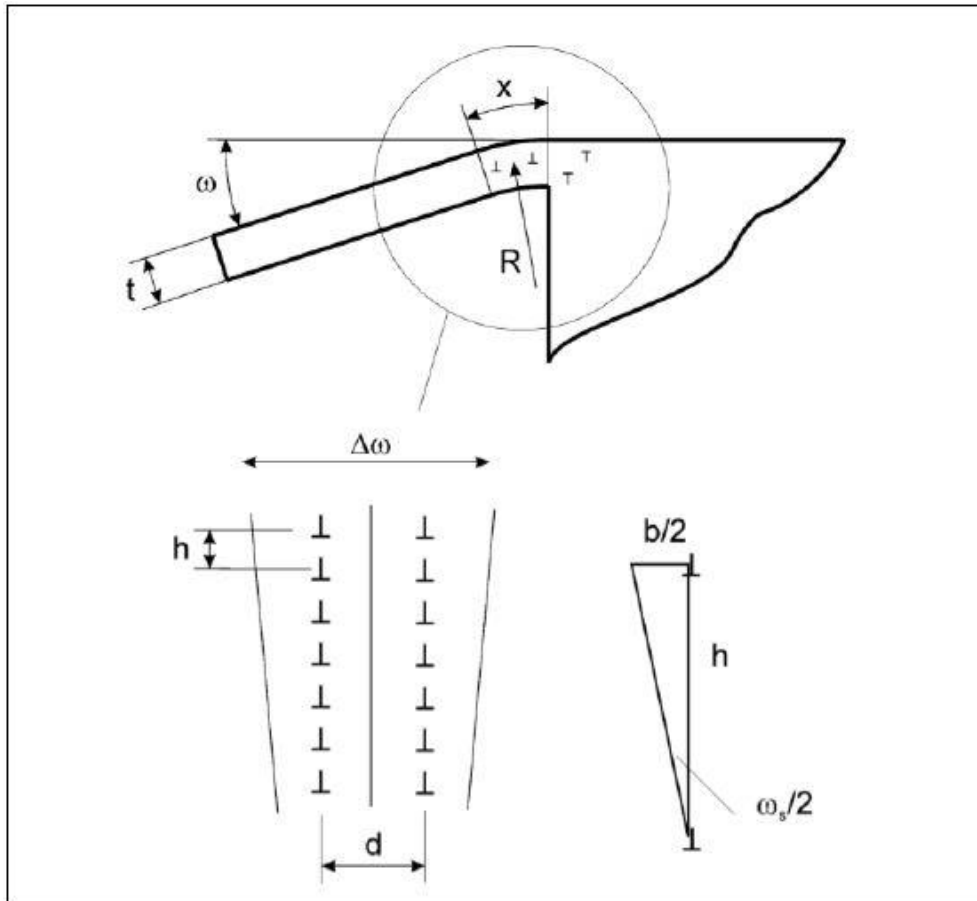
Figure 11: Geometric set-up of bending beams and dislocation arrangement of GNDs to accommodate the strain gradient [46].
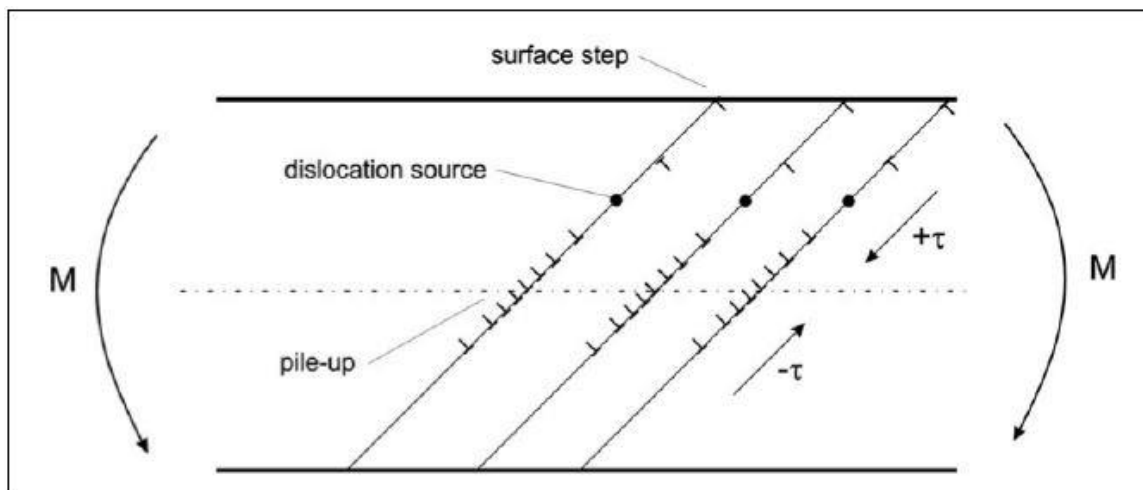


Figure 12: Possible underlying dislocation mechanism for the deformation of the micro-beams [46].

The applied strain gradient determines the total number of GNDs. Now, with the assumption that only one dislocation source is available, all GNDs must be put on one slip plane, resulting in a massive pile-up at the beam center and consequently in a significant pile-up stress. However, an increase in the number of available dislocation sources allows the GNDs to

distribute over several slip planes and the pile-up stresses will decrease. In the case of a large amount of available dislocation sources, the GNDs can distribute more or less uniformly and one can neglect this pile-up effect. Reducing the beam thickness has two effects. The deformed volume will decrease and therefore the possibility of finding dislocation sources is decreased. Also, there will be a reduction in the length between the dislocation source and the beam center. These effects support the dislocation pile-up at the center and increase the flow stress. This becomes evident in Figure 13, where it is shown that for high dislocation source densities the contribution of the pile-up effect is small, and almost negligible when compared to the strain gradient contribution. On the other hand, the pile-up effect becomes dominant as the source density is reduced, from which the high flow stresses can be explained.
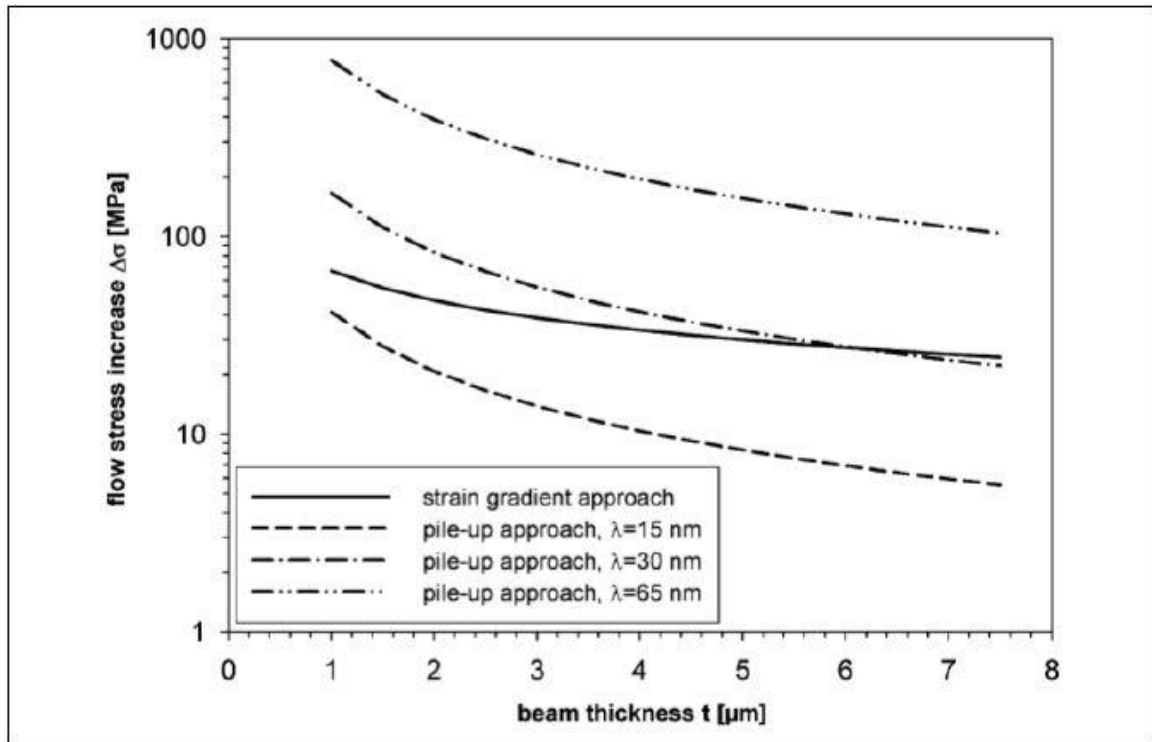


Figure 13: A comparison of the flow stress contributions of the pile-up and strain gradient approach with different mean dislocation source spacing, $\lambda$, depending on the beam thickness [46]

A different approach is taken by Demir et al. [18]. Instead of the impact of GNDs, a mean field breakdown theory is discussed, in which the local availability of dislocation sources is claimed to dominate the mechanical size effect. The thicknesses of the cantilevers ranged between 0,7 and 5 µm and were bent with a nanoindenter. After calculating the cantilever's yield strength, the following size effect was found; smaller is stronger. But the GND density estimated from misorientation maps did not explain the resulting size effect. It is stated that GNDs can contribute to the flow stress after pre-straining, that is when the GNDs build up. However, with small critical strains used to define the yield strength, it is explained that the size dependency also will occur in samples that are not pre-strained. Therefore, the paper concludes that the size effect is a result of the local availability of dislocation sources.

Plastic deformation may be hindered by a reduction in the number of available dislocation sources in the small deformed volume. A limitation of the available dislocation sources will result in these sources having a very high activity, but due to the back stress of the emitted dislocations, a source can become inactive. In such a case, the source is only reactivated by

applying a higher stress and thus the flow stress increases. Moreover, with a small defect density, the possibility of finding a sufficient number of dislocation sources decreases, and the strength of the material will increase as the material becomes dislocation starved. A high ratio of surface volume may also explain a dislocation starvation condition [46].

Different mechanical behavior that contributes to the size effect has been presented in this chapter, including strain plasticity, dislocation pile-up at the beam center and limitation of available dislocation sources. Due to the fact that the contributions are not independent of each other, a simple arithmetic addition of the contributions is not promising. A strict separation is not possible since dislocations of the different processes will influence each other.

## 2.3 Hydrogen Embrittlement Models

Significant research efforts have been conducted to describe the underlying and driving mechanisms of HE and based on empirical approaches and numerical simulations several micromechanical models have been proposed. Through direct observation, some of the effects of HE is quite obvious. However, the advanced HE models explaining H-assisted fracture are hypotheses that need experimental verification. One certain aspect of the HE controversy is that there are many viable mechanisms of the H-assisted failure and that the search for a single mechanism to explain all experimental observations is destined to fail. Having received large support, there are today a few established models for non-hydride-forming metallic materials. The models are commonly used separately or in a combination to describe the HE effects.

### 2.3.1 Hydrogen – Enhanced Decohesion (HEDE)

This model was first reported by Troiano in the 1960's, suggesting that the presence of atomic H at an introductory fracture zone will degrade the fractural behavior. The mechanism is anticipated to be most significant at GBs and interfaces, where H is captured and spread along a crystallographic plane. Due to the charge transfer from the host metal to the H atom, H will contribute to a weakening of the interatomic bonds across these planes. Consequently, the decrease in the crystal's cohesive strength will provoke embrittlement and reduce the needed work for fracture. For heterogonous interfaces, the concentration of H on the free surfaces depends on the adsorption energy. However, it should be noted that a pure thermodynamic approach may be insufficient for describing the realistic conditions, which are commonly determined by the kinetics of the separation process when the free surfaces are formed. The HEDE mechanism is schematically represented in Figure 14.
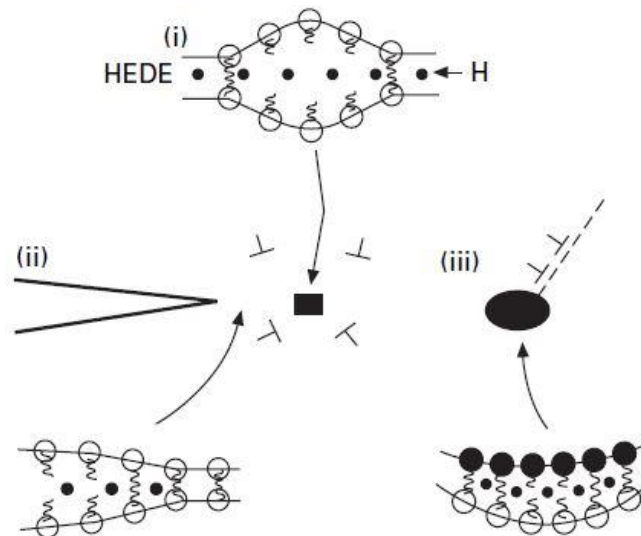


Figure 14: A schematic representation of the HEDE mechanism, involving tensile separation of atoms due to the weakening of interatomic bonds by (i) H in the lattice, (ii) absorbed H, (iii) H at precipitates – matrix interfaces [19].

Mcmahon et al. [20] discussed the added effect of H in the lattice or near a GB in steels. Is was stated that H-induced brittle fracture of steels is a stress-controlled phenomenon which is a result of the combination of hydrogen dissolved in the crystal lattice and embrittling impurities segregated at GBs. As a result of high stresses generated by the precipitation of H at impurity inclusions, crack initiation will take place. Since H is a unique element due to its extremely high mobility and its strong attraction to an expanded crystal lattice, it was explained that as a microcrack nucleus began to spread away from the inclusion H would be drawn to the core of the crack tip. Subsequently, H will be carried with the tip as it spreads, similar to which H is

transported by gliding dislocations. However, the attraction to the crack tip will be much stronger because of the greater lattice expansion. Consequently, by assuming that H decreases the cohesive energy, the cohesion at the crack tip will decrease as the crack propagates and gathers H. Furthermore, the tendency for H-induced cracking increases with increasing yield strength. As high yield strength allows higher stress, two effects will follow: (1) Due to the large atomic volume of dissolved H in Fe, H will move to locations of the crystal lattice that are enlarged by a tensile stress. Therefore, H is collected at locations of stress concentration. This is a quite fast process because of the significant high diffusivity of H in Fe. (2) The reduction of cohesive strength of Fe due to the presence of H, in which the combination of increased H concentration and elevated stress leads to the formation of a crack when critical conditions are reached. It was, therefore, claimed that H-induced cracking is controlled by three variables; the purity of the steel, the H pressure and the hardness of the steel.

The degradation effect of H on the cohesive strength is supported by both computational models and indirect experimental observations. First principles density functional theory calculations confirmed that the cohesive strength of a $\alpha$-$Al_2O_3$ single crystal decreases with increasing H concentration [21]. Results from calculations in the [0 0 1] direction, showed a decrease in the cohesive strength from 48.9 GPa to 39.6 GPa with increasing H concentrations from 0 to 4900 wppm. Furthermore, indirect evidence of the HEDE mechanism was observed during an examination of HE in FeSi - and Ni – single crystals [22]. The crack tip opening angle was measured as a function of H pressure, and at constant temperatures, the crack tip opening angles for both single crystals increased with decreasing H pressures. This clearly corresponds to metals having a higher degree of surface toughness at lower pressures of H. In the opposite case, the crack tip opening angles decreased as the H pressure increased, which is an indication of Hs decohesion effect. Through the interpretation of features on the fracture surface, HEDE quickly became one of the most recognized and established HE mechanisms. However, there are still conflicting opinions about its role in the brittle fracture process. M. L. Martin et al. [23] investigated the underlying microstructure of the flat featureless regions of an H-induced fracture surface, which are interpreted as evidence for HEDE. The fracture surface was extracted by FIB machining and investigated with high-resolution scanning electron microscopy (SEM), atomic force microscopy (AFM) and transmission electron microscopy (TEM). Examinations immediately beneath the fracture surface revealed a fracture feature topology with fine-scale undulations that are associated with an underlying dense arrangement of dislocations, and thus not consistent with the HEDE mechanism. Instead, it was suggested that H contributes to establishing the dislocation substructure and local H concentration, resulting in increased crack ability in that specific location. The latter emphasizes the need for describing the H-deformation interactions with respect to plasticity and will be discussed further in section 2.3.2.

In general, the weakness of HEDE is the lack of direct supporting evidence. There is no direct experiment describing the decrease of the interatomic force-displacement relationship due to dissolved atomic H in metals or alters the elastic characteristics and surface energy based on the bonding.

## 2.3.2 Hydrogen – Enhanced Localized Plasticity (HELP)

The HELP mechanism and its role in embrittlement is primarily supported by experimental observations. Beachem [24] proposed that H in a solid solution would increase dislocation activity and enlarge a plastic area in front of the crack tip, which contained more inclusions acting as void nuclei. These observations state that the presence of H in a solid solution decreases the barriers to dislocation motion and will increase the magnitude of deformation that occurs in a localized region in the vicinity of the crack tip. Although, not being conclusive, the mechanism is also referred to in the understanding of macroscopic measurements of reduced material yield stress and other softening events when H is present [25], as well as for microscopic observations of enhanced dislocation mobility after in – situ H charging strain tests [26], [27]. It presents the local plasticity and strain softening of a material, and thus explaining the hydrogen – enhanced plastic failure which appears macroscopically brittle. HELP is commonly described in two mechanisms; (1) H increases dislocation mobility, leading to material softening and (2) H reduces dislocation – dislocation interactions facilitating planar slip and increases dislocation pile-up, allowing further deformation of the material and leading to the start of damage [28].
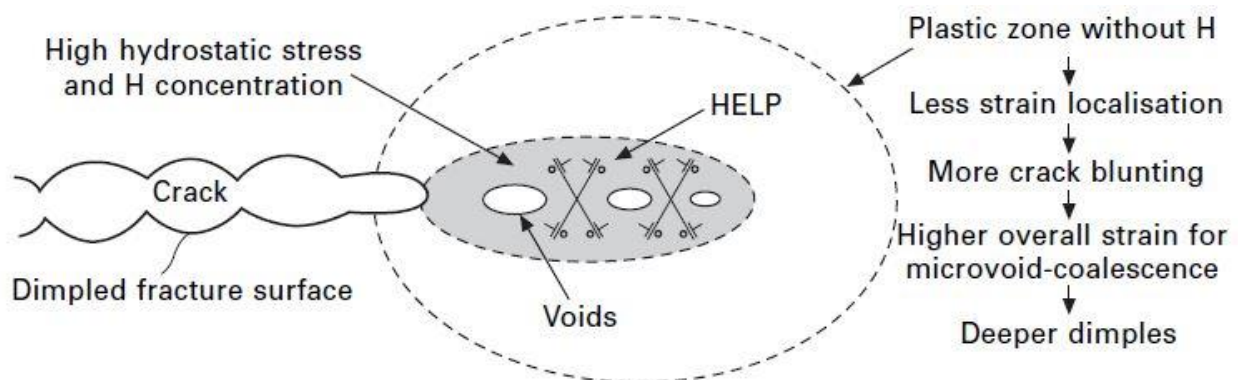


Figure 15: A schematic representation of the HELP mechanism, involving a microvoid-coalescence process, with plasticity localized in regions of high H concentrations [15].

Although the mechanism is widely accepted as an explanation of the H-enhanced plastic failure, oppositional observations have been reported. Through an in – situ transmission electron microscopy (TEM) small-scale experiment on samples deformed in tension, Ferreira et al. [29] reported that neither of the two mechanisms is present. The paper implies that a third mechanism should be considered; (3) H interacts with other defects to alter the ability of those defects to hinder dislocation motion. J. Song et al. [30] investigated H's potential influence on edge dislocation mobility and pile-up structures in Fe. Their molecular simulation showed that H decreases the dislocation mobility rather than enhances it. Moreover, when a load was applied the simulation also revealed that the pile-up structure is independent of the presence of H, implying that the atmosphere of H offers no measurable shielding of dislocation interactions. These results also indicate that the two, often suggested, mechanisms for HELP are not active. Consequently, other HELP mechanisms have been developed and studied in more detail.

An important effect was documented in an analysis of essential elements of HE associated with brittle intergranular fracture in high-strength steels [31]. In the presence of H, it was shown that the locally stress-controlled fracture can be modeled as the result of three major sequential microscopic events: (i) dislocation interactions against GB carbide, (ii) interface failure of the carbide, (iii) decohesion along the GB resulting in intergranular fracture. The interesting discovery was that the three events potentially are accelerated by the presence of H, in which the first event (i) is due to the HELP mechanism and events (ii) and (iii) are due to the HEDE

mechanism. In other words, the description presents a synergistic interaction between the HELP and HEDE – mechanisms in the development of H-induced fracture. The simultaneous action of the mechanisms was also reported in the impact testing of H-induced low carbon steel [32], [33]. It was claimed that the initial dominant activity of HELP was followed by a sudden transition to HEDE when a critical amount of H concentration was reached, indicating that the simultaneous action of the two mechanisms is dependent on the local H concentration. A mixed mode of fracture characterizes the coexistence of the mechanisms, with the simultaneous presence of brittle transgranular fracture features, primarily by HEDE, and locally ductile, fine microvoid coalescence fracture features due to HELP activity. The decline in ductility is due to the simultaneous effect.

The existence of superabundant vacancies (SAVs) in metals and alloys is well known, and experiments have shown that H facilitates their preservation. With the presence of SAVs inside a metal or alloy, a dislocation can meet or even pick up the SAVs, working as obstacles along its gliding path, or SAVs can be attracted toward it. When H-stabilized SAVs is present, the behavior of dislocations is thus expected to change [34]. In a recent study, the hydrogen/vacancy effect on dislocation behavior was investigated through cyclic compression loading of an aluminum pillar inside TEM [35]. The experiment provided clear evidence that dislocation locking will take place in the presence of H. However, the observed locking effect is not from H atoms acting alone. It was proposed that the segregation of hydrogenated vacancy to a dislocation results in the locking effect. Obviously, this observation is not in compliance with the HELP mechanism, but the effect of hydrogenated vacancy is relevant for the modeling of HE and will need further analysis.

### 2.3.3 Adsorption – Induced Dislocation Emission (AIDE)

Lynch [36] suggested that the surface effect of the absorption of H at crack tips is a crucial factor in HE. The AIDE model claims that absorbed H on the crack surface reduces the formation energy of dislocations at the crack tip. Consequently, the dislocation generation rate will increase. The HELP and AIDE models are similar in that the resulting local plasticity causes HE. However, in the AIDE model, it is the external H on the crack surface and not the internal in the bulk which influences the dislocation dynamics. In other words, HELP focuses on the dislocation mobility enhanced by H, while AIDE focuses on the enhancement of the dislocation injection from the surface [37].

Due to the high stresses required for dislocation emission, it will be accompanied by general dislocation activity in the plastic zone, which results in the formation of small voids at particles or at slip-band intersections. Therefore, dislocation emission is the primary cause for crack growth, but void formation ahead of the crack tip also contribute. The void formation also maintains small crack-tip radii and small crack-tip opening angles. AIDE could also occur at tips of voids, given that a sufficient amount of H diffuses or is transported by dislocations to the voids ahead of cracks. The latter is not an essential requirement of the mechanism. [38].

## 2.4 Focused Ion Beam (FIB) Milling

A FIB combines imaging with a precision machining tool, where the imaging capabilities are similar to those of a scanning electron microscope (SEM). The FIB is a lithographic method with the advantage of short wavelengths, thus allowing higher resolution, but without the disadvantages displayed by the low mass of electrons. It produces and guides a flow of high energy ionized atoms of a massive element. The ionized atoms are focused onto the sample for the purpose of milling the surface and as a method of imaging. Due to the ions' greater mass, surface atoms can easily be removed from their positions while secondary electrons from the surface allow the ion beam to image the sample during, before and after the lithography process. The FIB uses a liquid-metal ion source at the top of its column to produce the ions. Subsequently, the ions are pulled out and focused into a beam by an electric field. Then, they pass through openings and are scanned over the sample surface by an accelerating voltage. Although the FIB system by itself has a wide range of functions and applications, there are some disadvantages associated with only using an ion beam. These disadvantages include sample destructive imaging at higher magnifications and less accurate control of the milling [39].

### 2.4.1 Ion-Solid Interactions

Energetic particles entering a solid lead to the initiation of several processes in the area of interaction. A small part of the particles is backscattered from the surface layers, while the rest are slowed down in the solid. Although the ion-solid interactions are essential in the FIB application, the ions' effect on the sample material can be a cause for concern. The kinetic energy of the ions hitting the surface of a sample is proportional to the applied voltage on the FIB, and can in some cases, be large enough to cause irreparable damage to the imaged sample area. The types of damage include atomic sputtering, ion emission, localized heating and ion implantation in the sample surface.

When an ion hits the sample surface and collides with the surface atoms, the transfer of the ion's kinetic energy to a surface atom is either elastic or inelastic, as shown in Figure 16. In inelastic collision, some of the ion energy is transferred, by the ion's momentum, to either the surface atoms or electrons in the sample. This is called electronic energy loss and will lead to ionization which is followed by the emission of secondary electrons and electromagnetic radiation from the sample. In order to provide a topographic image of the sample surface, the emission of these secondary electrons is necessary. The elastic collision is the collision of ions into the sample where the incident ion makes a kinetic collision with an atom and transfers a part of the kinetic energy to the atom. The recoiled atom successively collides with another atom and induces a cascade collision, also known as nuclear energy loss. In this process, some of the recoiled atoms are emitted or sputtered from the sample surface, mostly as neutral particles and partly as positively or negatively charged ions. The mean path of the emitted sample particles is shown in Figure 17. If the primary beam current is low little material is sputtered, while for high primary currents sputtering can remove a great amount of material. The sputtering effect enables the precise local removal of material i.e. milling. [40].
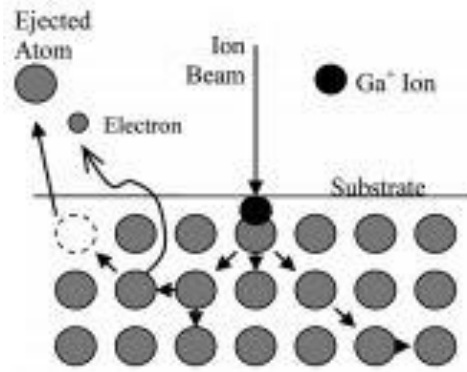
Figure 16: Schematic illustration of the interaction between a $Ga^+$ and a solid. The $Ga^+$ ion causes the emission of electrons, but also atoms in the crystal lattice [41].
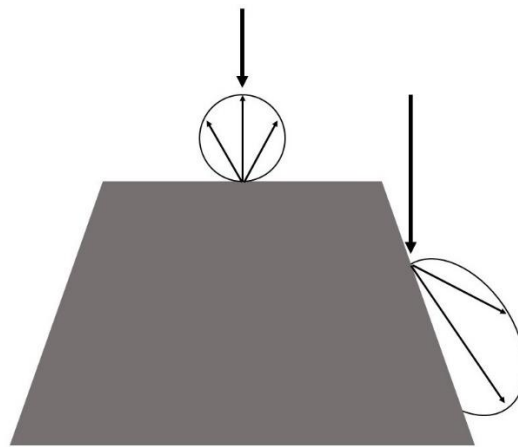


Figure 17: The mean path of the emitted sample particles relative to the incident angle.

2.4.2 The Dual-Beam Microscope

The dual-beam allows imaging and sample modification without having to physically move the sample, as it combines an SEM and FIB into one system. The two beams are placed in fixed positions with a relative angle of $52°$. Co-focusing enables the two beams to intersect at a shared point on the sample surface with a working distance of approximately 4 mm, as illustrated in Figure 18. Commonly, this point is called the coincidence point and is the optimized position for the majority of operations taking place within the microscope. To minimize surrounding contaminants, the sample is situated on a stage inside a chamber with a vacuum system. Moreover, the stage can be tilted, allowing alterations in the sample-beam orientation. The chamber is also equipped with detectors, which enables the microscope to form high-resolution images by collecting secondary electrons. A schematic overview of the dual-beam microscope is presented in Figure 19.
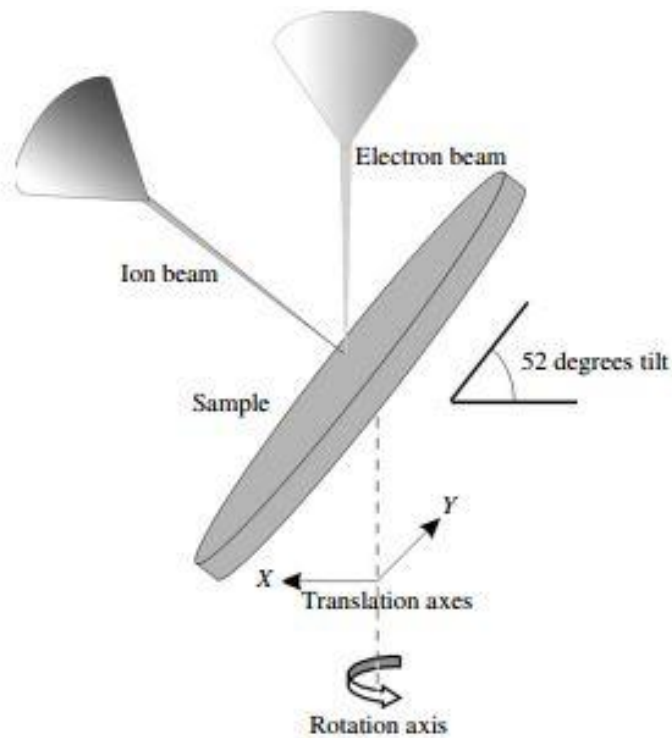
Figure 18: The dual-beam system, where both beams are co-focused at the coincidence point on the sample surface [36].
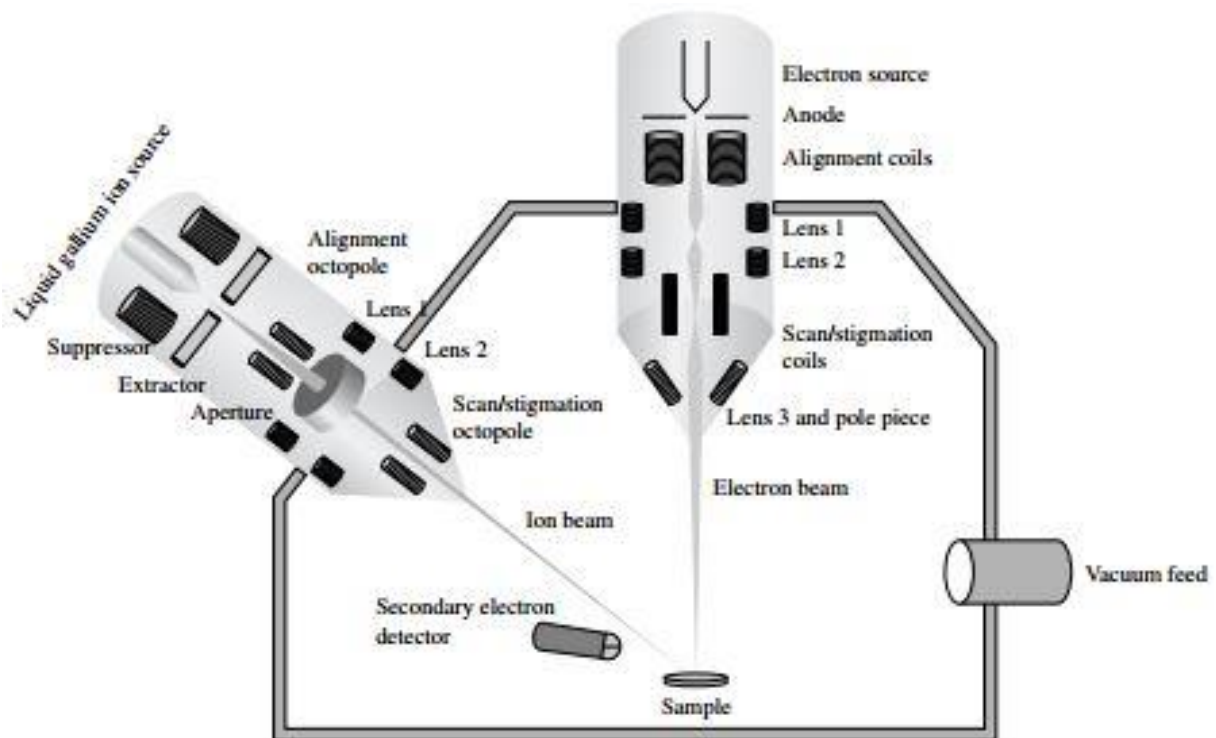


Figure 19: Schematic representation of the configurations of a two-beam FIB system (dual-beam) [36].

An important aspect in understanding the FIB is to consider the beam source, shown in Figure 20. The ion column consists of a reservoir of heavy-metal Ga atoms. In the reservoir Ga is heated to near evaporation, resulting in the flow of Ga which eventually will wet a heat-resistant

tungsten needle. The needle tip is located immediately above the extractor, which is an annular electrode concentric with the needle tip. Due to a potential difference between the needle tip and the extractor opening, an intense electric field is created which causes liquid Ga to be drawn into a Taylor-cone. Since the cone tip is small enough, the aperture's extraction voltage can pull Ga from the needle tip and ionize it by field evaporation. Subsequently, ion emission will occur, and the ions begin to accelerate down the column and towards the sample surface. The extraction current is regulated by both the suppressor and the extractor, where the suppressor and extractor correspond to the fine and coarse controls of the emitted ion distribution respectively. The suppressor uses an applied electric field of positive potential (up to + 2 kV) when it works together with the extractor to maintain a constant beam current. This is especially important during milling operations, where a constant beam current supports the control of the etching rate. Adjusting the suppressor voltage leads to a change in the extractor current, which implies that the extraction current can be regulated without changing the voltage of the extractor. This is preferable since a change in the extractor voltage can result in a spatial displacement of the Taylor-cone and beam drift on the sample surface. [36].
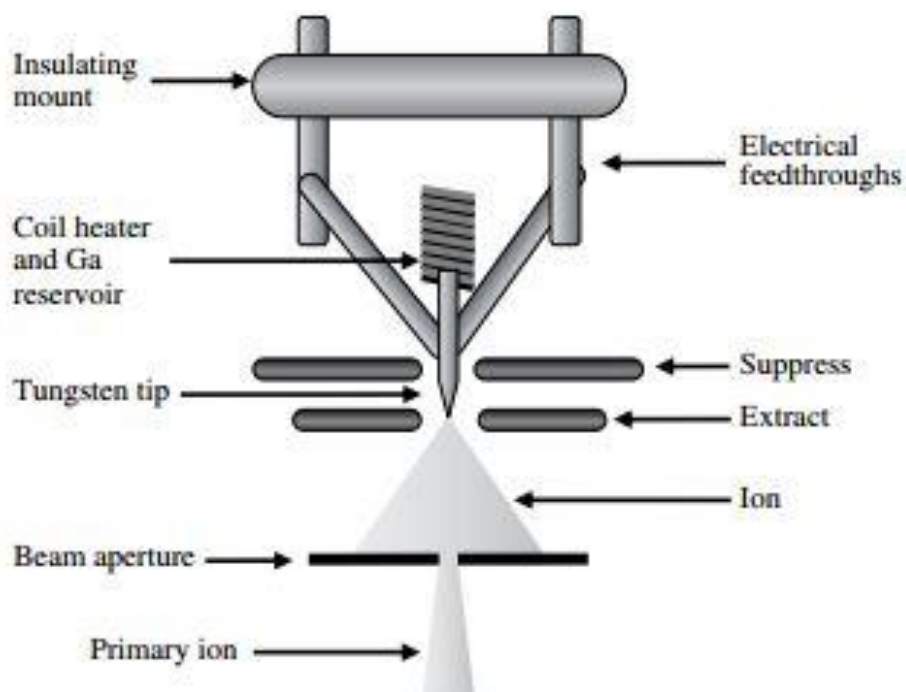


Figure 20: Cross-section of a Ga ion source in the FIB [36].

## 2.4.3 Sputtering Yield

During the cascade collision process within a solid, which is caused by the kinetic collision between an incident ion and a surface atom, some atoms are ejected from the sample surface. The sputtering yield is defined as the number of atoms removed from a solid surface per incident ion. Precise milling of geometries at the nanoscale is completely dependent on this effect, but a quantitative approach to the sputtering yield is difficult. This is mainly because of its dependence on several varying factors such as the sample material, sample topography, crystal orientation, and ion beam incidence angle. From a milling perspective, it would be preferable to obtain as even sputtering rate as possible. This would enhance the overall control and predictability of the milling operation, but an even sputtering rate becomes problematic when milling in areas of varying microstructure, grain orientation and topography. Low sputtering yield is a result of little collision between the $Ga^+$ ions and sample atoms, which is the case when the ion experiences a free path and can easily move deep into the sample. In contrast, high collision between $Ga^+$ and sample atoms result in high sputtering yield. Whether the ion

path is free or not is in most cases determined by the spacing of the sample atoms, and thus by the grain orientation. Figure 21 a) and b) illustrates how the spacing of sample atoms, due to grain orientation will affect the sputtering yield. Furthermore, since more material will escape near a free surface area, the sputtering yield will also be affected by the surface topography, as shown in Figure 21 c).
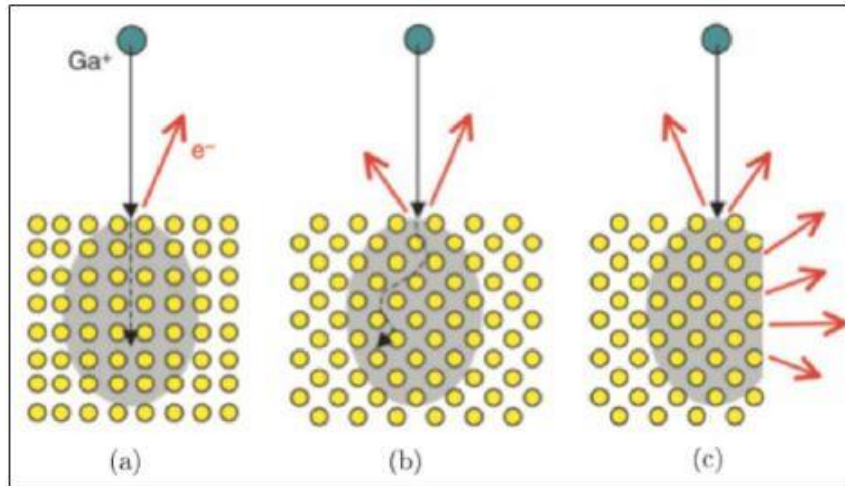


Figure 21: Schematic illustration of the sputtering yield and the effects of crystal orientation a), b) and surface topography (c) [37].

2.4.4 Redeposition

The redeposition effect is a serious obstacle in nanostructure milling. Especially since such milling operations require high accuracy and predictability. Sputtered atoms can be ejected from the sample surface into a gas phase, and since these atoms are not in their thermodynamic equilibrium there is a change that they will condense back into the solid phase as they collide with any solid surface nearby. Thus, some of the ejected atoms may hit the already sputtered surface and redeposit onto it, which alters the sputter profiles. Redeposition particularly becomes a challenge in milling operations involving specific geometries. These operations often include several milling steps and pattern geometries, and redeposition of sputtered material on already milled surfaces will change the sputtered profile and create unwanted features. Redeposition also restrains the milling patterns' depth. When the beam mills further into the solid sample, the sputtered material will remain in the crater instead of being ejected out of it, causing a "competition" between sputtering and redeposition. Furthermore, it is very hard to predict the location of the redeposited material, which obviously will make the milling more unpredictable and less controllable. However, there exist some degree of predictability as the ejected atoms from the sample surface will emerge with a variety of paths, where geometrical effects due to structural features will affect the location of the redeposited material.

2.4.5 Fabrication of Microcantilevers

The FIB machining technique enables milling of micro-scale cantilever samples, from which the opportunity to perform micro-scale fracture experiments arises. This will allow a local evaluation of the mechanical properties and it becomes possible to investigate selected areas within crystalline materials. In the cantilever milling process, a specified amount of material is removed from a defined area on the sample surface, where the overall milling quality strongly depends on the beam's controllability. Microcantilever testing and research have in recent times experienced growing attention, which consequently has led to a variety of milling methods. The following section will separate the most typical methods and describe their procedures.

The first method involves milling directly on the sample surface [42], [43], [44], [45], [46]. Here, a freestanding cantilever is produced by removing the material underneath it, in which the sample needs to be tilted during milling. The milling of the first cantilever bottom edge is performed by tilting the sample 45˚ relative to the ion beam. For the other one, the sample is rotated 180˚. It is worth mentioning that a square cross-sectional cantilever will not be possible to produce in this method, due to the stage movement configurations in the FIB. This method will, on the other hand, concern cantilevers with cross-sections symmetric on the vertical axis while asymmetric in the rectangular axis. The most commonly produced cross-sections in this method include the triangular cross-section and the pentagon cross-section, as shown in Figure 22. However, the selection of one of these cross-sections is not indifferent, as their cross-sectional differences will facilitate distinct mechanical behaviors and should, therefore, be based upon the experimental purpose. Loading a cantilever with a pentagon cross-section will, for instance, maintain a constant crack width during the initial crack growth.

A great advantage with this method is that it requires little sample preparation, as the sample surface only needs basic grinding and electropolishing. Furthermore, since cantilevers potentially can be milled at any site, the method is flexible when considering where to fabricate, thus offering large prospective areas. On the other hand, significant amounts of material must be removed in the milling procedure, and if assuming a proportional relation between the milling time and the amount of removed material, the overall milling operation will indeed become very time consuming, particularly if the experiment requires a series of cantilevers.
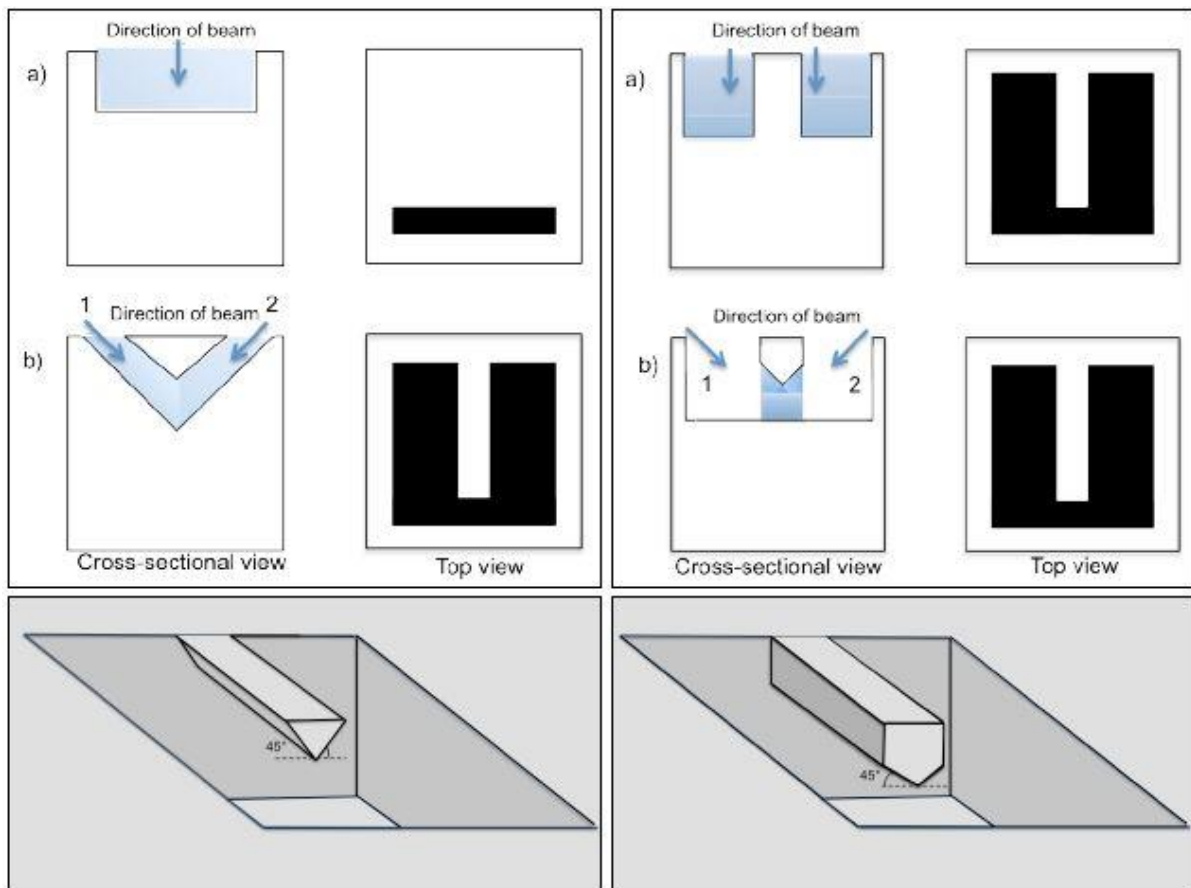


Figure 22: Schematics of cantilever fabrication directly on the sample surface and the main steps of the milling procedure. Triangular cross-section (left) and pentagon cross-section (right).

The second method utilizes the space around the sample edges. Regions close to the sample edge offers the opportunity to fabricate cantilevers with a rectangular cross-section [47], [48], [49], [17]. Following this method, it is possible to produce both horizontal and vertical cantilevers, as shown in Figure 23. A sample rotation of 90˚ relative to the ion beam is needed to remove base material for the horizontal cantilever while no sample tilt is required for the fabrication of vertical cantilevers. The vertical cantilevers will, however, require deeper milling into the sample in order to obtain an appropriate cantilever height. There is always a degree of unpredictability when milling into the sample, as areas identified on the sample surface may differ from the areas in the subsurface. For instance, in the case where an area of interest has been determined by means of EBSD mapping, only the surface is scanned and characterized while the subsurface area remains undetermined. To avoid milling in an unfit area due to subsurface complications, simple verification techniques can be performed, as presented in section 3.6 for GB verification when milling BC cantilevers.

Obviously, since the fabrication of cantilevers in this method is constrained to areas around the edges of the sample, the number of potential milling areas are limited. Furthermore, in order to achieve cantilevers of satisfactory quality, the samples will need high surface quality and sharp edges and thus a more thorough sample preparation is required. Nevertheless, this method offers cantilevers with a rectangular cross-section, which implies that the crack width will remain constant during loading.
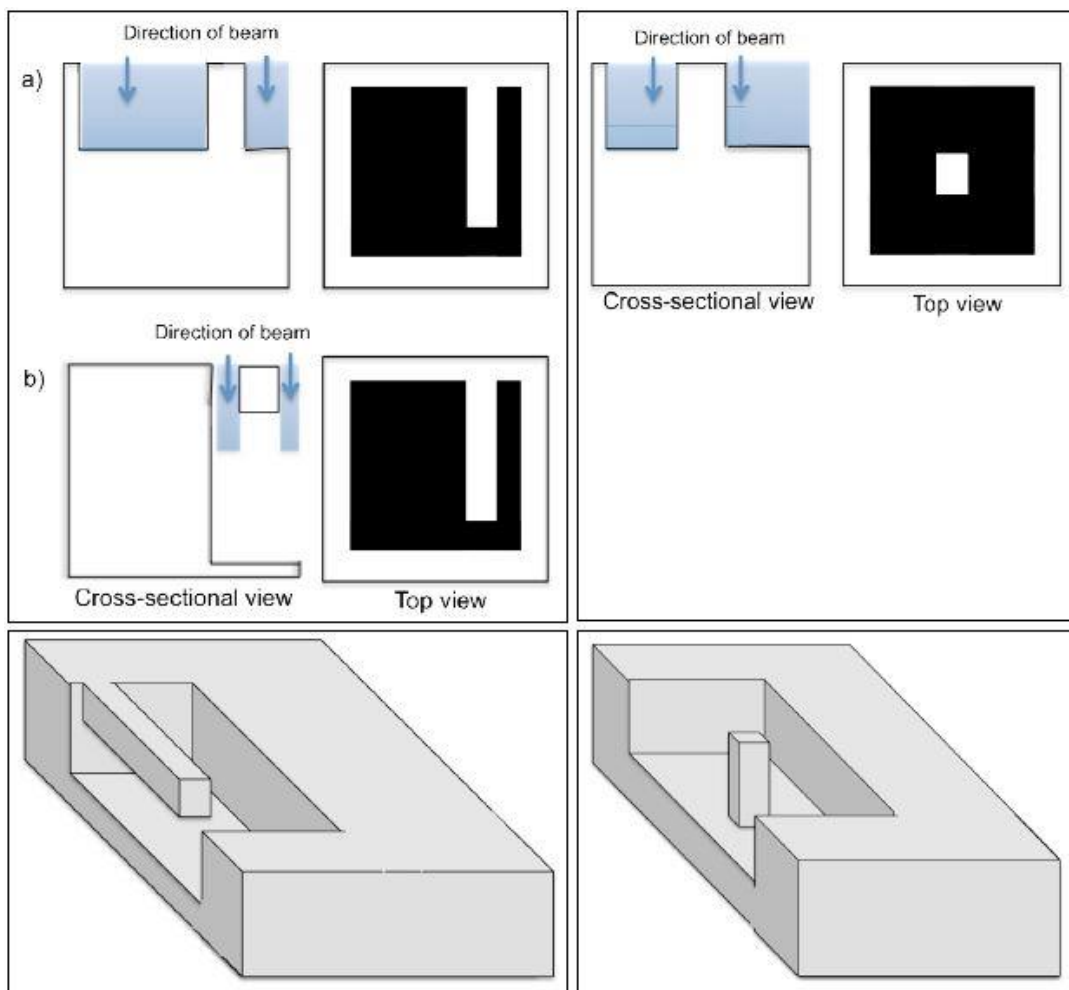


Figure 23: Schematics of cantilever fabrication on the sample edge and the main steps of the milling procedure. Horizontal cantilever (left) and vertical cantilever (right), both with a rectangle cross-section.

The third method involves milling cantilevers on thin lamellas. As the width of these lamellas is in the micrometer range, the milling procedure is significantly simplified and since scarce amounts of material are removed the milling time is drastically reduced. Cantilevers in this method are also fabricated with a rectangular cross-section, as shown in Figure 24. Furthermore, the cantilevers can be machined at any site on the thin film, granting flexibility to the specific area selection. However, for desired cantilever quality, a comprehensive and cautious sample preparation is needed.

Cantilevers fabricated by this method are extensively utilized in the testing of thin films [50], [51]. Although the FIB unquestionably is an efficient milling tool for thin film cantilevers, it is also possible to produce similar thin film samples by altering the purpose of a transmission electron microscopy (TEM) sample. TEM utilizes the ion slicing technique as a preparation method to manufacture thin freestanding lamellae at the micro-scale. In contrast to pure FIB milling, the use of the ion slicing technique in the initial sample preparation step will most likely decrease the ion damage, which is mainly because of the use of argon rather than gallium and lower acceleration voltage [52].
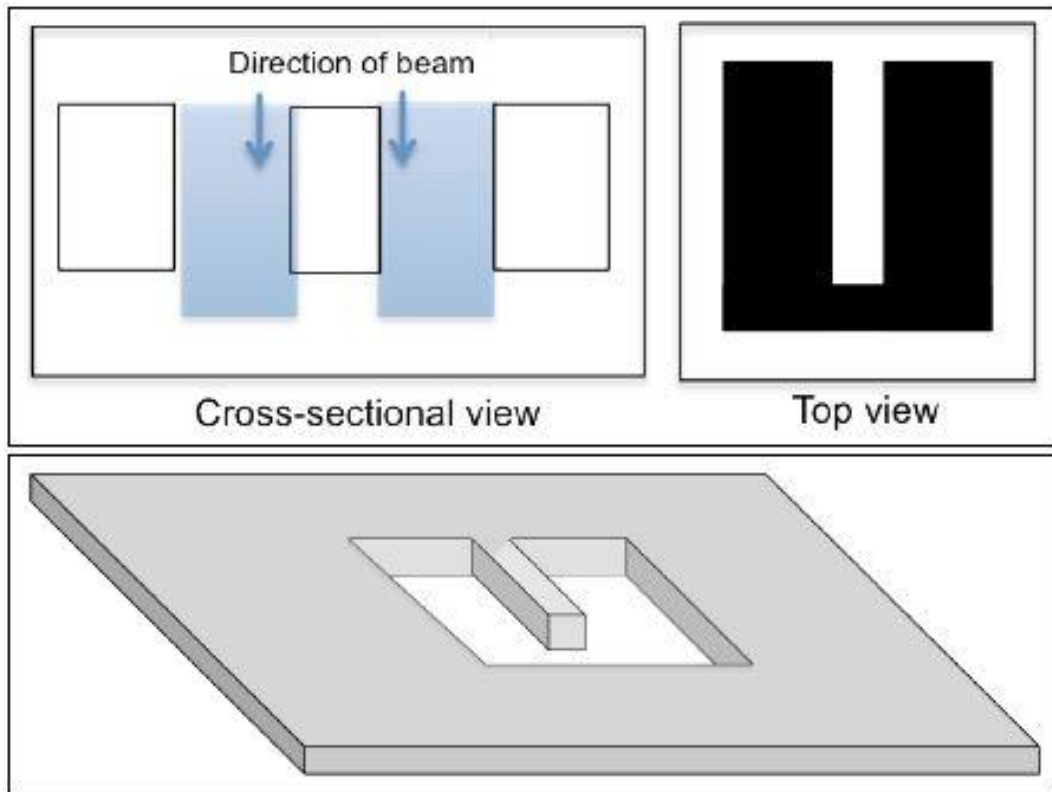


Figure 24: Schematics of cantilever fabrication with rectangular cross-section directly on the thin film sample and the main steps of the milling procedure.

## 2.5 Electron Backscatter Diffraction (EBSD)

EBSD is a microstructural crystallographic characterization technique to study crystalline or polycrystalline materials, and is commonly employed as an additional characterization technique to a SEM. This allows routinely characterization of individual grain orientations, local texture, point-to-point orientation correlations and phase identification on material surfaces.

In order to detect the electrons, that are accelerated by the electron beam and diffracted by the atomic layers in a crystalline sample, a phosphor screen is situated within the SEM chamber. As the diffracted electrons hit the phosphor screen they are detected, from which EBSD patterns are generated. These patterns, commonly called Kikuchi patterns, are characterized by a regular arrangement of parallel bright bands on a steep continuous background. The Kikuchi patterns are a geometric projection of the lattice planes in the crystal on the flat phosphor screen. One can think of the lattice planes being stretched out to intersect the phosphor screen in the center of the lines of their related Kikuchi bands, as shown in Figure 25. As a result, it is possible to obtain direct information about the crystalline structure and crystallographic orientation of the respective grains from which the patterns originate.
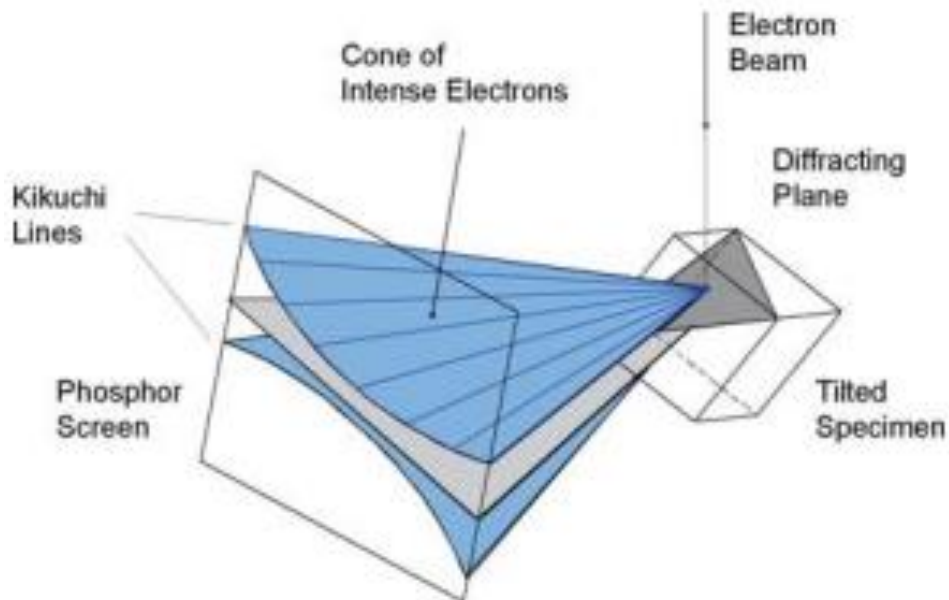


Figure 25: Schematic illustration of the incident electron beam on a sample with a given unit cell orientation and a specified diffracting plane causing backscattered Kikuchi diffraction. The edges of the Kikuchi band are defined by the two diffracting cones, where the geometric projection of the diffracting plane onto the phosphor screen is the center of these cones [50].

In the EBSD setup, the Kikuchi patterns are formed by a stationary electron beam directed onto the grain of interest, in which the spatial and depth resolution of the EBSD will depend on sample tilt, sample density and the beam's accelerating voltage. Typically, the sample surface is tilted approximately 70° relative to normal incidence of the electron beam, as shown in Figure 26. The reason for this steep inclination is because of the steep forward scattering of electrons. Thus, the intensity of the generated Kikuchi patterns will decrease with less surface inclinations. Moreover, the EBSD is a fully automated system. A quantitative texture analysis requires a statistically significant number of individual grain orientations, and a manual collection of such data by an operator would be extremely time consuming and inconvenient. The only input required by the automated EBSD system is the step size of the sample stage. The SEM is

controlled by the EBSD software, where the beam will raster across the sample on a user specified and pre-defined grid. At each point in the grid the beam will stop to acquire the Kikuchi patterns, index the orientation and record the coordinates as well as the orientation vectors. [53].
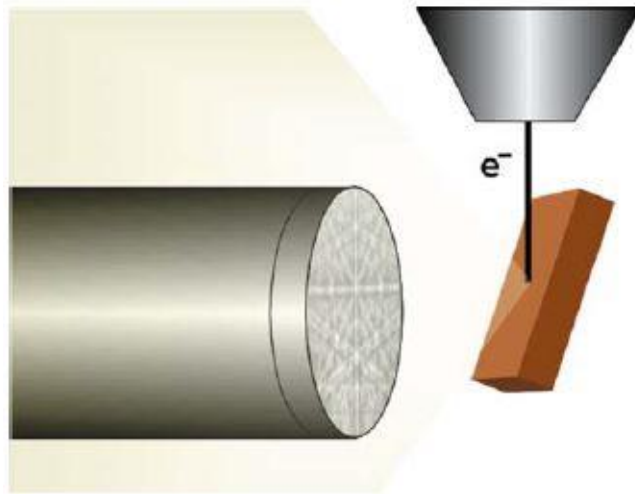


Figure 26: Schematic illustration from inside the SEM chamber of the electron beam, the tilted specimen (~70˚) and the Kikuchi patterns on the phosphor screen [50].

# 3. Experimental Procedure

## 3.1 Sample Materials

Table 1 lists the sample materials used in this project. The samples had a circular surface with a diameter of 12mm. After the samples had been prepared, they were fixed in a cylindrical sample holder, as shown in Figure 27.

| Sample materials |
|---|
| NiS |
| Pure Ni |
| Solution annealed Ni725 |
| Precipitation hardened Ni725 |
| Over aged Ni725 |
| Solution annealed Ni718 |

Table 1: List of sample materials.



Figure 27: Sample holder.

## 3.2 Sample Preparation

A crucial prerequisite for the EBSD analysis is the quality of the sample surface, in which the smooth sample surface is obtained through several preparation stages. The alloy sample was cut from a coil by EDM (electrical discharge machining), with 12 mm diameter.

The preparation of the sample surface was performed with stepwise mechanical grinding, using grinding discs of decreasing roughness; P500/30,2µm, P800/25,8µm, P1000/18,3µm, P2000/10,3µm, P4000/2,5µm. Between each step the sample was rotated 90˚ relative to the previous step and a microscope was utilized to ensure that all grinding scratches were parallel in one direction. During mechanical grinding the sample surface layer is subjected to substantial deformation, from which a precise crystallographic surface characterization is not possible. To get valid EBSD results, the damaged surface layer was fully removed by electropolishing. Electropolishing is a critical process, involving the variables of material voltage and time, which triggers the sample to corrode either locally or even across the entire surface. Therefore, it is important to quickly rinse the sample with alcohol and constantly verify the sample surface

in an optical microscope. The optimal electropolish conditions for the samples was defined with a cell voltage of 13V at 30s. A sample surface roughness of maximum ~1nm μm^-2 was finalized by the electropolish, using a mixture of 95% methanol (CH3OH) and 5% sulfuric acid (H2SO4). It should be mentioned that a more standard approach to sample surface preparation is to polish the surface with diamond polishing after grinding. In this way the overall surface roughness will be lower before the electropolishing stage. However, in this experiment it was found that electropolishing results were better with some initial surface roughness.

Following grinding and polishing, the sample surface was marked with a macro indenter. The first indent was made in the center of the sample, which was identified by measuring the horizontal and vertical sample radiuses. As illustrated in Figure 28, the indented area was 2.4x2.4mm with an even indent spacing of 1,2mm. Two reference indents were made in the bottom right corner to prevent coordinate confusion when the sample is rotated.
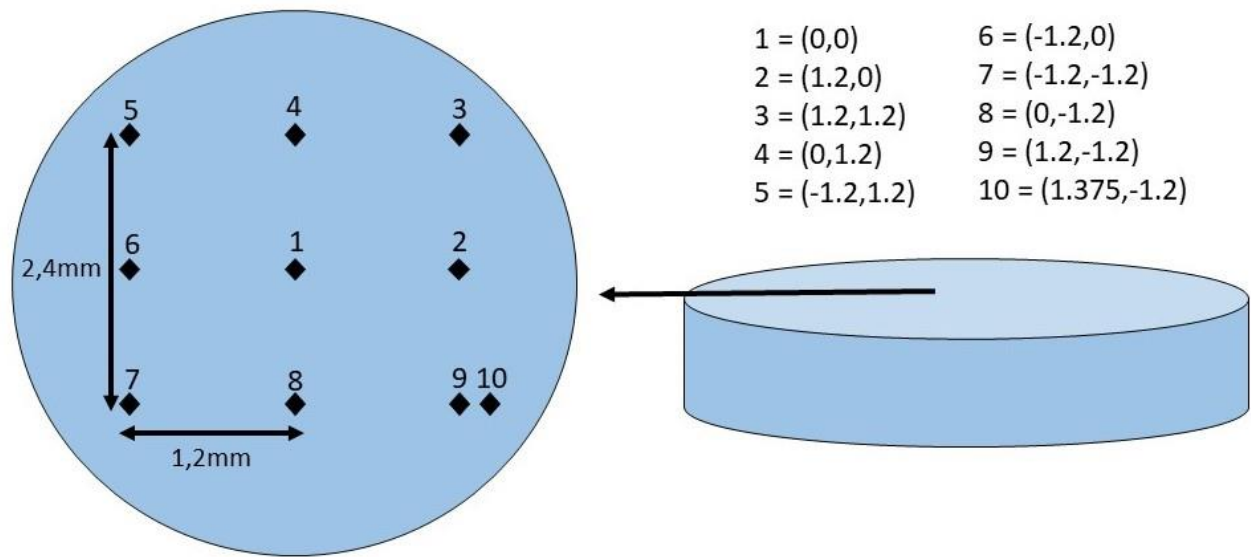


Figure 28: Surface marking.

## 3.3 EBSD Analysis

To locate suitable sites for cantilever milling on the sample surface, the surface grains need to be analyzed. The data from an EBSD analysis can be utilized to determine the crystallographic orientation, size and misorientation of grains within a selected surface region. In this work, the EBSD analysis were performed using a high-resolution Nordif EBSD detector installed in a FEI Quanta FEG 650 Environmental SEM, with four overlapping scan quadrants of 1.2x1.2mm, as shown in Figure 29.
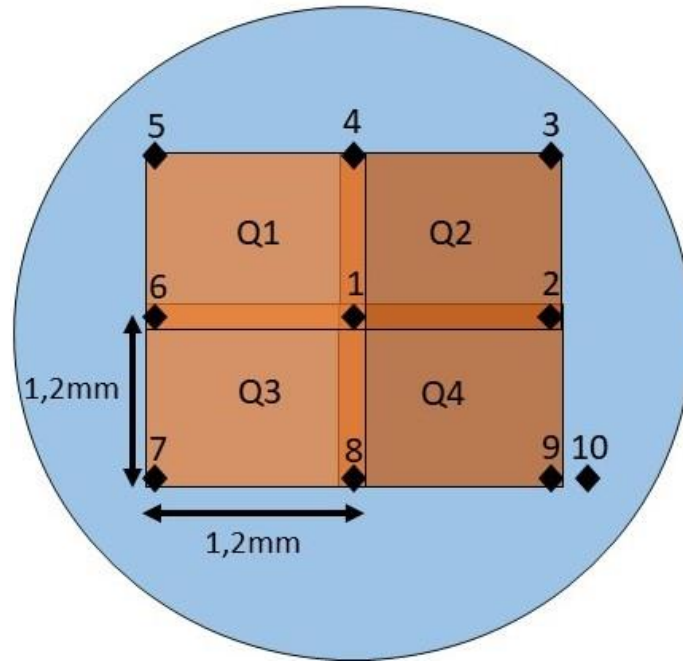
Figure 29: Scanning quadrants on the sample surface.

The sample was mounted on an inclined stage, which gave the sample surface a 70° tilt relative to the electron beam. For the SEM image to show the same surface grid alignment as in Figure 29, the sample had to be manually rotated and adjusted on the stage. The stage was mounted inside the SEM chamber and adjusted so that the sample surface was facing the phosphor screen. After defining the sample working distance, the phosphor screen was pushed into the chamber towards the sample surface. The final EBSD sample setup is shown in Figure 30.
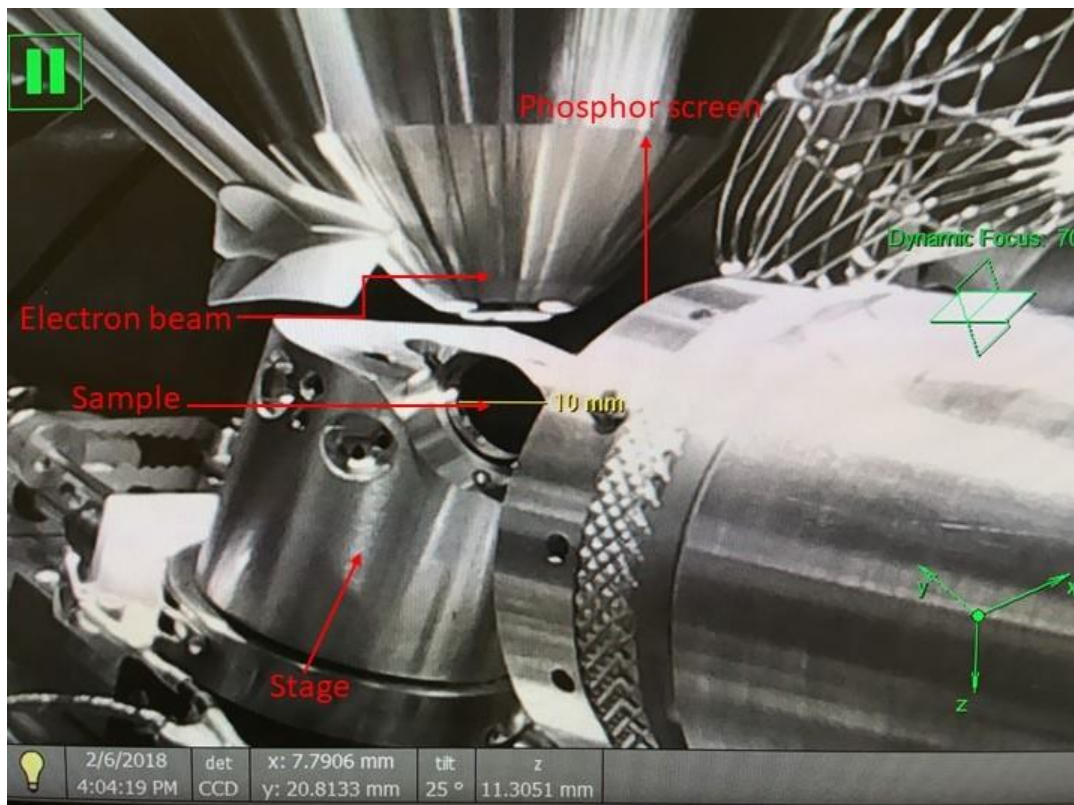


Figure 30: EBSD setup inside SEM chamber.

To make accurate measurements of the crystal orientation, the Nordif software requires a precise point source calibration. Therefore, 2 calibration points were selected in each corner of the quadrant and 1 acquisition point was selected in the middle of the quadrant. For reliable results, it is important that these calibration points show clear diffraction patterns (Kikuchi patterns). To ensure high-quality diffraction patterns it was first of all essential to prepare a high-quality surface. Clear patterns were also obtained by avoiding overlaying patterns and by removing the background light to ensure that light bands in the pattern were well defined. EBSD parameters used are presented in Table 2 and Figure 31 shows the achieved diffraction pattern quality.

| Parameter | Value | Parameter | Acquisition settings | Calibration settings |
|---|---|---|---|---|
| Acceleration voltage | 20,0kV | Frame rate | 23fps | 18fps |
| Working distance | 10.9mm | Resolution | 292x292px | 292x292px |
| Tilt angle | 70˚ | Exposure time | 42978µs | 55055µs |
| Step size | 5µm | Gain | 10 | 6 |
| Resolution | 1000x1000px | | | |

Table 2: EBSD scan parameters.
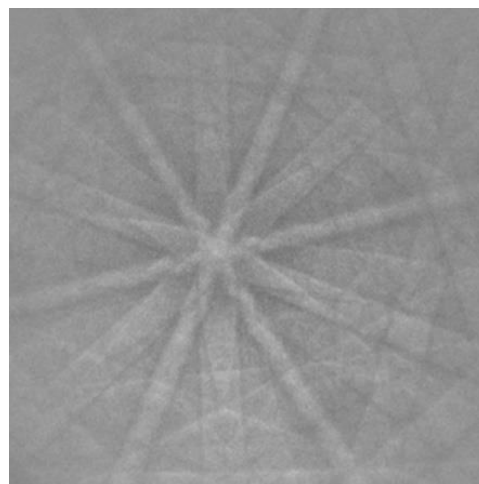


Figure 31: An example of the achieved diffraction pattern quality

As indicated in Table 2, the scan step size was set to 5µm. This means that for every 5µm within the defined scan area, a diffraction pattern is captured and stored by the Nordif software. To extract and convert these diffraction patterns into a corresponding grain orientation map TSL OIM data collection was utilized. By selecting the calibrated quadrant as the background, this software collects and converts the diffraction patterns from each point scan and gives a color-coded map of the quadrant. The color-coded map is a direct interpretation of the surface grains within the quadrant, where each color represents a specific crystallographic orientation normal to the sample surface.

Since the purpose of this analysis was to locate and identify a suitable cantilever milling site, it should be mentioned that it was not always necessary to scan all four quadrants. A suitable milling site was sometimes located after scanning just two or even one of the quadrants. Furthermore, the efforts in preparing a high-quality sample surface was critical for a valid EBSD analysis. If the surface layer is influenced by corrosion or severe deformation, the diffraction patterns become unclear resulting in an unreliable representation of the surface grains and their respective orientations.

## 3.4 Selection of Milling Sites

The results from the EBSD analysis were assessed in TSL OIM analysis, from which grains and GB's of interest were highlighted based on information about grain orientation, grain size, and grain misorientation. To ensure comparable and consistent behavior of all samples during beam loading, the selected milling sites included grains of similar orientation. Subsequently, the direction of the cantilever axis relative to the surface grain was determined. Depending on whether the cantilevers were going to include a GB i.e. bi-crystalline cantilevers or were to be milled within a single grain i.e. single-crystalline cantilevers, the procedure of determining their milling sites and directions were persistent for all samples. The following will present the principals and methods that was applied for determining the milling site and cantilever axis direction for the NiS bi-crystalline sample and the Ni 725 solution annealed single-crystalline sample. See Appendix A: EBSD maps and selected milling sites, for EBSD maps and milling locations for all samples.

### 3.4.1 Bi-Crystalline Milling Sites

In order to determine a suitable location for bi-crystalline (BC) cantilevers, it was essential to locate straight GBs with sufficient length to accommodate the number of cantilevers. Then the GB properties were considered. As discussed in section 2.1.3.1, GBs of higher energy are expected to trap larger amounts of H. Therefore, preferred GBs had a high misorientation angle i.e. high angle GBs, as they are expected to have higher energy. When a suitable GB had been identified a cross-section of the sample surface was milled to examine the GB orientation in the sample subsurface, as presented in Table 4 in section 3.5. To ensure ideal stress conditions for crack propagation during cantilever loading, it was desirable that the GB's orientation through the subsurface was oriented perpendicular to the sample surface.

Since the GB was to be placed 2 μm onto the cantilever from the cantilever base, the cantilever would include a supporting grain and a deflecting grain. To increase the possibility that the GB would open during cantilever loading, it was necessary to define the direction of the cantilever according to the soft and hard crystallographic direction of each grain. The grain that had the softest crystallographic orientation was selected as the deflecting part of the cantilever, while the hard grain was selected as support.

The selected GB and milling site for the cantilevers on the NiS sample is shown in Figure 32 (a). They were oriented so that the grain of the supporting part of each cantilever had a [1 0 1] normal orientation and the grain of the deflecting part had a [1 1 1] normal orientation. Thus, the crystallographic direction of the cantilevers was selected as <1 0 0> for the hard grain and <1 1 0> for the soft grain [54], as shown in Figure 32 (b). The selected GB type was a high angle Σ5 GB with a misorientation of 35,9 at [1 -23 1] (P1: [12 3 11] P2: [21 4 4]). An SEM image of the selected GB is shown in Figure 32 (c).
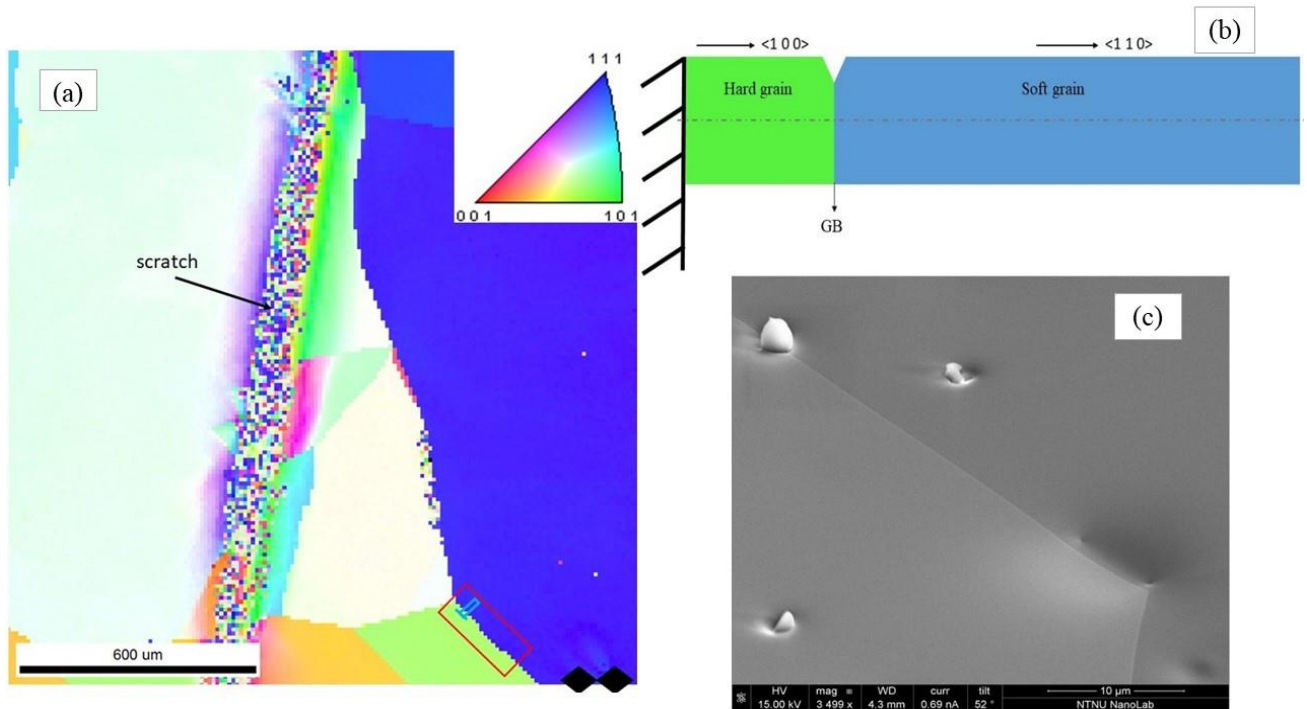
Figure 32: (a) Color-coded map (IPS map) of NiS sample surface region. The marked area with red rectangle show the tested GB. (b) Selected crystallographic axis directions of BC NiS cantilevers with respect to the hard and soft grain. (c) SEM image of selected GB.

### 3.4.2 Single-Crystalline Milling Sites

Milling sites for single-crystalline (SC) cantilevers on the Ni725 solution annealed superalloy were selected within [1 0 1] normal oriented grains. To increase the possibility of observing crack growth during in-situ cantilever loading, the tensile stress direction of the cantilevers, i.e. the cantilever axis, was oriented parallel with the cleavage plane of the sample, hence the cubic <1 0 0> direction [55], [71].

In order for the cantilever axis to be arranged parallel with the <1 0 0> grain direction, they had to be rotated accordingly inside the selected grain. The rotation angle was determined by identifying the <1 0 0> direction from the EBSD data and then measure its relative angle with a horizontal reference line. By aligning the cantilevers according to the horizontal line between two indents in the quadrant, the correct milling orientation was accessed by rotating the grain, hence rotate the FIB stage, clockwise according to the determined angle.

The selected grain for cantilever milling is shown in Figure 33 (a). Figure 33 (b) shows the [1 0 1] cubic orientation of the selected grain, and its corresponding <1 0 0> direction. The parallel arrangement between the cantilever axis and the <1 0 0> direction was obtained by a 37˚counterclockwise stage rotation relative to the horizontal reference line.
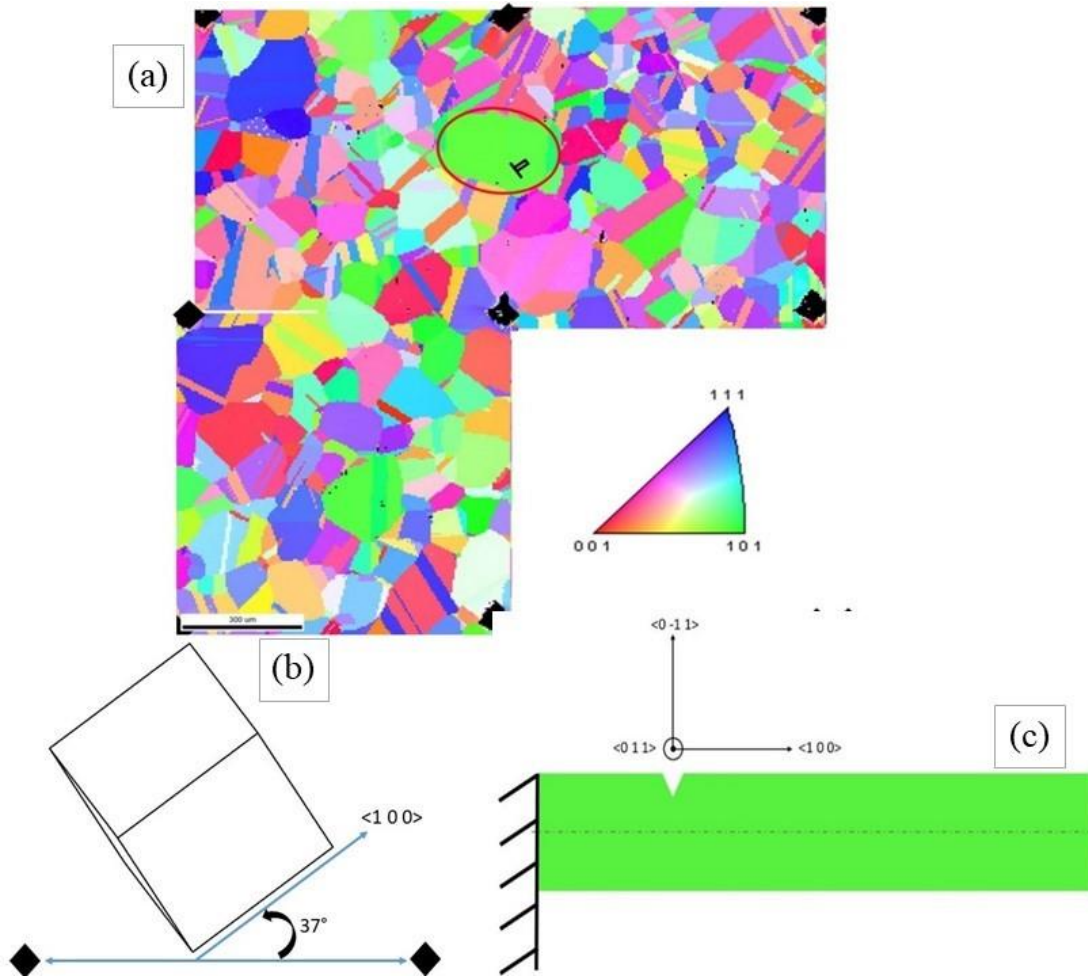
Figure 33: a) Color-coded map (IPS map) of Ni725 solution annealed sample (3 quadrants). The marked area with red circle show the tested grain. b) Cubic grain orientation with corresponding direction, <1 0 0>, parallel to the cleavage plane, as well as needed counterclockwise grain rotation for parallel alignment between cantilever axis and cleavage plane. c) Respective crystallographic directions of SC Ni725 solution annealed cantilevers.

## 3.5 Micro-Cantilever Milling

The cantilever milling was conducted on a FEI Helios DualBeam FIB system at NTNU NanoLab. Initially, the EBSD map was used to locate the area of interest on the sample surface. The milling process was then initiated according to the correct milling site alignment given by the respective EBSD analysis. The total number of cantilevers milled on each sample and cantilever type is listed in Table 3.

| Sample | Number of cantilevers | Cantilever type |
|---|---|---|
| NiS | 10 | BC |
| Ni | 8 | BC |
| Ni725 solution annealed 1 | 8 | SC |
| Ni725 solution annealed 2 | 6 | BC |
| Ni725 pre. hardened | 6 | SC |
| Ni725 over aged | 8 | SC |
| Ni718 solution annealed | 6 | SC |

Table 3: Overview of type and number of cantilevers milled on each sample.

As presented in section 2.4.5, there are different methods for producing cantilevers. In this experiment, the cantilevers were produced with a pentagonal cross-section by milling into the sample surface, hence Figure 22 (right). The milling process was divided into different steps with respective milling parameters, as shown in Table 4. There was no observable variation in milling properties of the different sample materials when comparing the accumulated milling depth in real time and the estimated effective milling time. The same milling parameters was therefore used for all materials in each step. Initial steps of the milling process were executed with a relatively high ion beam current, due to the substantial material removal. As a consequence of the material re-deposition during milling, it was essential to have sufficient clearance between the cantilevers. The safety distance between each cantilever was therefore set to 25µm. It was also important to remove enough material beneath the cantilever to secure space for an unknown beam deflection during loading. The beam current and pattern dimensions were gradually reduced in the following steps to accurately obtain the desired cantilever dimensions along with sharp edges and high-quality surfaces.

Since high currents were used, current build-up occurred on the sample during milling and imaging. This resulted in an ion beam drift, which sometimes could be in the micrometer range and thus influenced the positioning of the milling patterns. The extent of the drift depends on the magnitude of the current, in which higher currents promote higher drift rates. It was therefore necessary to image the surface multiple times with the ion beam, to control that the patterns were positioned correctly. Furthermore, it was essential to negotiate the beam drift by positioning the milling patterns with a safety margin (200 – 400 nm) from the cantilever edges in order to prevent excessive material removal.

To obtain angled bottom edges of high quality, step 4 was divided into two parts. For time efficient material removal, the first part had higher current. The desired surface quality and final dimensions was then adjusted by removing the remaining material with a much lower current in the second part. However, due to drift and small tolerances there was a danger of removing too much material in the final cleaning, and hence get incorrect dimensions. In order to ensure that the correct amount of material was removed, the milling progress had to be frequently controlled by imaging the milling area with the ion beam. Consequently, the milling operation became more time consuming and the sample surface was exposed to $Ga^+$ contamination. To avoid excessive ion imaging, the effective milling time of the first controlled bottom edge milling was established as a reference time for the remaining bottom edges. But since the amount of material to remove slightly varied from cantilever to cantilever, it was extremely difficult to predict appropriate milling durations and avoid control imaging. Another method was thereby tested. When desired material removal was achieved for the first bottom edge, the value of the accumulated milling depth was recorded. Subsequently, the milling of the remaining bottom edges was stopped when the accumulated milling depth reached the exact same value. For all bottom edges, it was found that appropriate amounts of material had been removed when the accumulated depth value reached 1,5 µm.

The milling in Step 1, 3 and 5 was executed with several rectangular milling patterns, with the respective alignments as illustrated in Table 4. Each pattern, generated in the FIB software, was defined with a milling direction so that the pattern would mill towards the cantilever or cantilever base, creating a wall. The pattern directions included bottom to top, right to left and left to right milling. Bottom to top milling was utilized to define the length of the cantilever and create the supporting cantilever base, while right to left / left to right milling was utilized to define the cantilever width. At first, each pattern was separately generated and defined with a specific milling direction, before being positioned according to the cantilever. However, after the milling, despite accurate pattern alignment, small milling deviations were observed for each milling pattern. Instead of generating each pattern separately in the FIB software, more
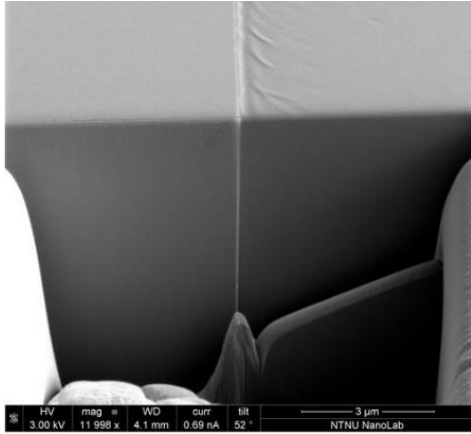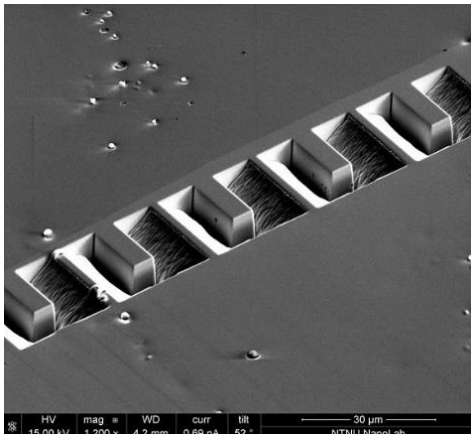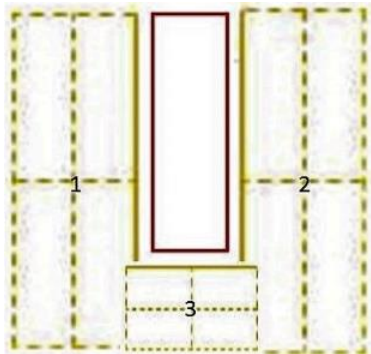
consistent milling was revealed when only one milling pattern with a specific direction was generated and then copied to generate the remaining patterns. The copied milling patterns were rotated to define their respective milling directions. A 180˚ rotation of a copied left to right pattern generated a right to left pattern, while the bottom to top patterns was obtained from a counterclockwise rotation of 90˚.

Because of the sample size effect, discussed in section 2.2.4, a sharp notch was milled on the cantilevers to obtain stress concentrations so that local crack propagation could be observed. For SC cantilevers the notch was milled 2 μm from the cantilever base, while for BC cantilevers the notch was milled on the GB positioned 2 μm from the cantilever base. Pre-notching the cantilevers is a complicated step in the milling process and there were critical factors to consider. Since the notch milling was based on a thin line pattern with a defined milling depth, the notch depths did not reach a desired constant value for all cantilevers. Instead, there was a slight variation in notch depths among the cantilevers. The reason for this is the re-deposition of sputtered material. As the line pattern mills deeper into the cantilever, the sputtered material will eventually be prevented from ejecting out of the thin notch. Consequently, sputtering and re-deposition will interact in a repetitive cycle and the notch will not reach the desired depth. When the notches were examined after the line milling it was also observed a deviation in notch depth on each cantilever side. This is due to an image drift in which the actual milling occurs a small distance away from where the milling pattern is defined. Depending on the drift direction, this will cause a small difference in the notch depths on each side. Furthermore, the milling pattern itself has a small initial drift at the moment the milling is initiated. To handle the notch variations, due to material re-deposition and drift, an area between two cantilever pits was selected for notch adjustment, before pre-notching the cantilevers. In this area, series of notches were milled to stabilize the image drift and measure the milling deviation due to initial pattern drift. Desired notch depth was achieved by adjusting the milling depth of the line pattern, i.e. the z value of the pattern, according to the reduction in milling depth due to re-deposition. The adjusted line pattern was then used to mill notches on the cantilevers. To compensate for the initial pattern drift, the line pattern was shifted the same distance as the measured milling deviation. Although image drift becomes stable after some time, precautions were always taken. Before starting the line milling an image was taken to check for pattern movement, due to image drift. If pattern movement was observed, the line pattern was adjusted back to its position, and a new image was taken after one minute of waiting to see if the image had stabilized. Since the total milling time of the notch is only 2 seconds there is a low possibility that critical image drift will occur during milling. It was therefore important to initiate milling immediately after no distinctive pattern movement. Furthermore, to ensure sharp notch tips, the line pattern was oriented parallel to the drift direction. Because of drift during notch milling, a line pattern oriented perpendicular to the drift direction will carry the risk of creating a wider notch with a resulting blunt notch tip.

In order to precisely position the indenter at the desired loading position a hole was milled on the top surface of the cantilevers. However, there is a large risk of damaging the cantilever by approaching it directly with the indenter. A more gentle and secure approach was achieved by milling a cross-mark at a known and aligned distance away from the hole. This will be further discussed in section 3.8.

When finished, the cantilevers had to be closely examined for any unwanted re-deposition, which potentially could ruin the experiment. To locate any re-deposition, the cantilevers had to be viewed from several directions and additional milling was necessary for removal and cleanup. Re-deposition can be located at discrete locations, as sputtered material ejected from the sample emerges with a variety of trajectories, and geometrical effects from specific features will affect its location.

Table 4: Millings steps with corresponding milling parameters.

|  | **STEP 0:** Examine GB orientation in subsurface<br>**Stage tilt angle:** 52˚ i.e. ion beam perpendicular to sample surface<br><br>1. Cross-section cut<br>**Milling pattern:** 10x10 µm rectangle<br>**Milling depth:** z = 10 µm<br>**Scan method:** Regular cross-section milling with multiscan<br>**Acceleration voltage:** 30kV<br>**Ion beam current:** 9,3nA<br><br>2. Wall cleaning<br>**Milling pattern:** Rectangle fitted to wall<br>**Depth:** z = 5 µm<br>**Scan method**: Cleaning cross-section milling<br>**Acceleration voltage:** 30kV<br>**Ion beam current:** 2,8nA |
| --- | --- |
|  | **STEP 1:** Pit milling<br>**Stage tilt angle:** 52˚ i.e. ion beam perpendicular to sample surface<br>**Beam reference pattern:** 16,5x4 µm rectangle with surface measurement<br>**Milling patterns:** 1 and 2: 25x10 µm rectangles, 3: 8x8 µm square<br>**Milling depth:** z = 16 µm<br>**Scan method:** Regular cross-section milling with multiscan. 1: left to right, 2: right to left, 3: bottom to top<br>**Acceleration voltage:** 30kV<br>**Ion beam current:** 9,3nA<br>**Effective milling time:** ~30 min. per cantilever<br>**Pattern alignment:**<br> |

| | **STEP 2:** Milling angled bottom edges |
|---|---|
|  | **Stage tilt angle:** 7˚ |
| | **Beam reference pattern:** 16x5 µm rectangle without correction measurement, aligned with bottom edge of cantilever |
| | **Milling pattern:** Rectangle adjusted to remove material beneath the cantilever side surface, defined by the beam reference pattern |
| | **Milling depth:** z = 12 µm |
| | **Scan method:** Regular cross-section milling with multiscan, Top to bottom |
| | **Acceleration voltage:** 30kV |
| | **Ion beam current:** 6,5nA |
| | **Effective milling time:** ~10x2 min. per cantilever |
| | **Pattern alignment:** |
| |  |
| | When all cantilevers were milled on one side, the stage was rotated 180˚ to access the other side. |
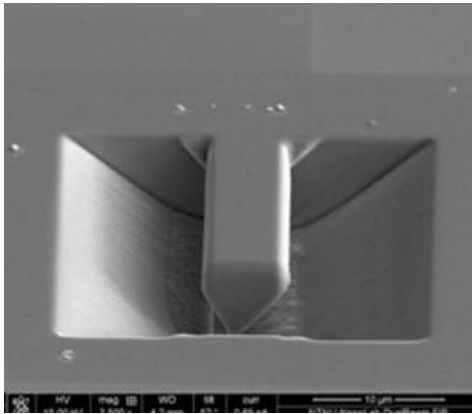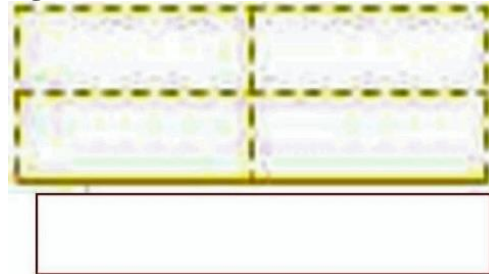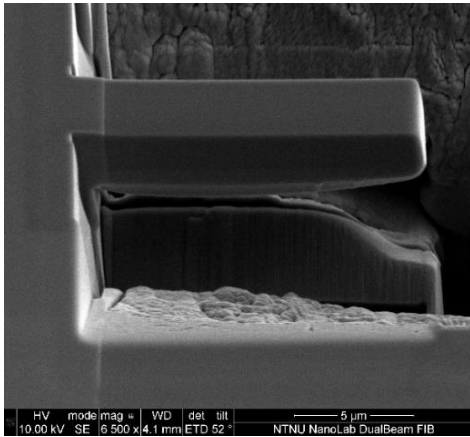
**STEP 3:** Reducing length and width

**Stage tilt angle:** 52° i.e. ion beam perpendicular to sample surface

**Beam reference pattern:** 16x3,5 µm rectangle without correction measurement

**Milling patterns:** All five milling patterns were rectangular, carefully adjusted according to the areas to remove

**Milling depths:** 1 and 2: z = 3 µm, 3: z = 4 µm, 4 and 5: z = 3 µm

**Scan method:** 1 and 2: Regular cross-section milling with multiscan, 3: Cleaning cross-section milling, 4 and 5: Cleaning cross-section milling. 1 and 2: bottom to top, 3: bottom to top, 4: left to right, 5: right to left

**Acceleration voltage:** 30kV

**Ion beam current:** 2,8nA

**Effective milling time:** ~7 min. per cantilever

**Pattern alignment:**

To obtain smooth corners, the bottom to top patterns were executed before the side patterns to allow small pattern adjustments if necessary
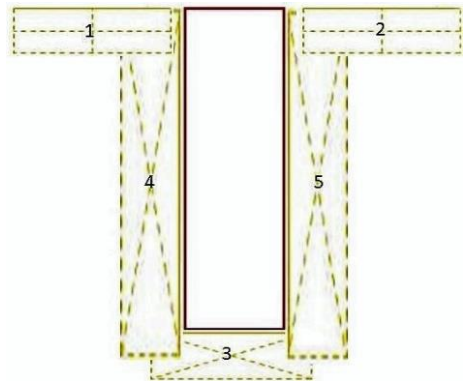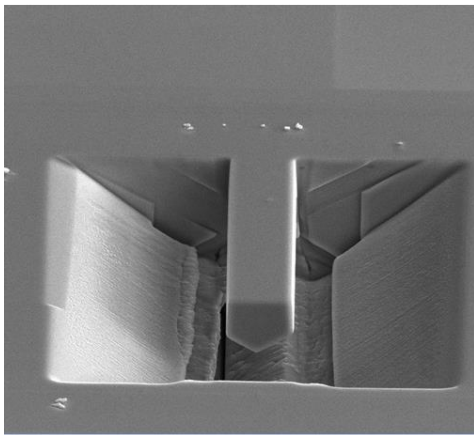
**STEP 4:** Completing angled bottom edges

1. High current for faster material removal
**Stage tilt angle:** -9˚
**Beam reference pattern:** 16x4,3 μm rectangle without correction measurement, aligned with bottom edge of cantilever
**Milling pattern:** Rectangle adjusted to remove material beneath the cantilever side surface, defined by the beam reference pattern
**Milling depth:** z = 3 μm
**Scan method:** Regular cross-section milling with multiscan, Top to bottom
**Acceleration voltage:** 30kV
**Ion beam current:** 0,46nA
**Effective milling time:** ~8x2 min per cantilever

2. Low current for sharp edges and high surface quality
**Stage tilt angle:** -9˚
**Beam reference pattern:** 16x4,125 μm rectangle without correction measurement, aligned with bottom edge of cantilever
**Milling pattern:** Rectangle carefully adjusted according to the area to remove
**Milling depth:** z = 3 μm
**Scan method:** Regular cross-section milling with multiscan, Top to bottom
**Acceleration voltage:** 30kV
**Ion beam current:** 93pA
**Effective milling time:** ~10x2 min. per cantilever

**Pattern alignment (for 1 and 2):**
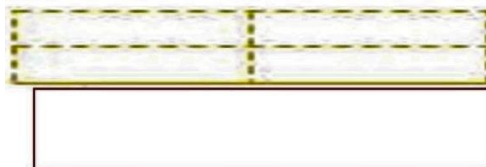


As in step 2, after all cantilevers had been milled on one side, the stage was rotated 180˚ to access the other side.
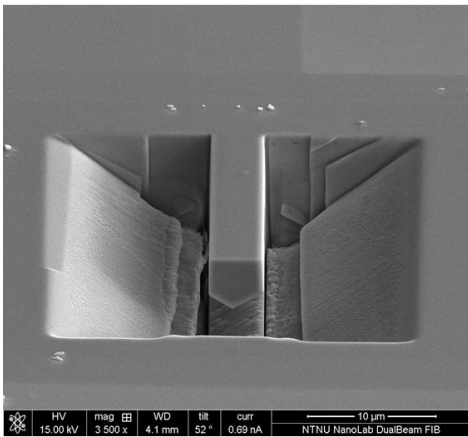
**STEP 5:** Final cleaning of all side edges
**Stage tilt angle:** 52˚ i.e. ion beam perpendicular to sample surface
**Beam reference pattern:** 15,5x3 µm rectangle without correction measurement
**Milling patterns:** All five milling patterns were rectangular, carefully adjusted according to the areas to remove
**Milling depths:** 1 and 2: $z = 0,5$ µm, 3: $z = 2$ µm, 4 and 5: $z = 2$ µm
**Scan method:** All five milling patterns were executed with cleaning cross-section milling. 1 and 2: bottom to top, 3: bottom to top, 4: left to right, 5: right to left
**Acceleration voltage:** 30kV
**Ion beam current:** 0,28nA
**Effective milling time:** ~15 min. per cantilever
**Pattern alignment:**

Like step 3, patterns defined for bottom to top milling were executed before the side patterns to allow adjustments for a smooth transition between cantilever edges and the supporting edge.
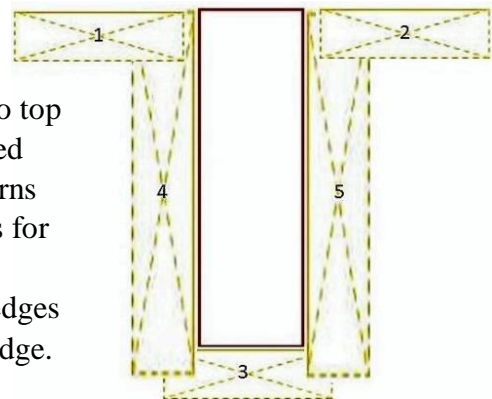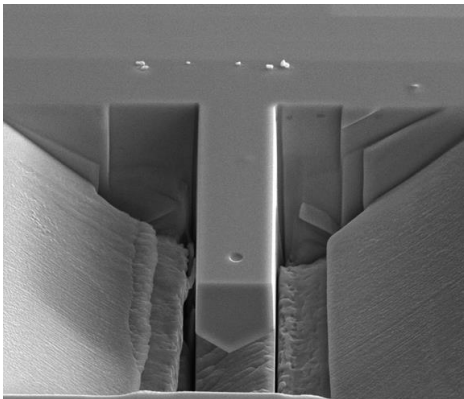
| | **STEP 6:** Milling the loading point |
|---|---|
|  | **Stage tilt angle:** 52˚ i.e. ion beam perpendicular to sample surface<br><br>**Beam reference pattern:** A primary rectangle with a length of 14 µm from the cantilever base and an identical width as the measured cantilever width after step 5. To highlight the center line of the cantilever, a secondary rectangle was used, with the same length as the primary rectangle but with half the width. The corner of the secondary rectangle, at the cantilever center line, was used as the aiming point for the hole milling. Measurement without correction<br><br>**Milling pattern:** Circle with a diameter of 0,6 µm<br>**Milling depth:** z = 0,15 µm<br>**Scan method:** Regular cross-section milling with multiscan, outer to inner<br>**Acceleration voltage:** 30kV<br>**Ion beam current:** 93pA<br>**Effective milling time:** ~3 sec. per cantilever<br>**Pattern alignment:**<br><br><br><br>Initial pattern drift of the circle pattern was measured in an area outside the cantilever site before milling was initiated. When the circle pattern was placed at the corner of the secondary reference pattern on the cantilever, it was shifted the same distance as the measured deviation to obtain the desired distance between the hole and the cantilever base. |

| | |
|---|---|
|  | **STEP 7:** Numbering and milling of cross-mark<br>**Stage tilt angle:** 7°<br>**Beam reference pattern:** Rectangle with an insignificant width (was set to 2 µm) as long as one of its top corners was aligned in the center of the loading point on the cantilever. The length of the rectangle was set so that the lower corner of the rectangle could reach a point directly beneath the hole on the surface at the other side of the cantilever pit (usually defined between 17-21 µm). A 6x6 µm square pattern was then used to center the cross at the lower rectangle corner. Surface measurement<br>**Milling pattern:** Lines, diagonally adjusted to exactly intersect the reference square at its corners and to make roman numerals for numbering<br>**Milling depth:** $z = 0,5$ µm<br>**Acceleration voltage:** 30kV<br>**Ion beam current:** 93pA<br>**Effective milling time:** ~2-15 sec. per cantilever<br>**Pattern alignment:**<br><br>The numbering of each cantilever was done with roman numerals, within an acceptable distance from the cross-mark (not too far away/not too close). |
|  | **STEP 8:** Notch<br>**Stage tilt angle:** 52° i.e. ion beam perpendicular to sample surface<br>**Beam reference pattern:** Rectangle with an identical width as the measured cantilever width after step 5. Surface measurement<br>**Milling patterns:** Line, adjusted with respect to the width of the cantilever and the initial pattern drift<br>**Milling depth:** $z = 1$ µm<br>**Acceleration voltage:** 30kV<br>**Ion beam current:** 9,7pA<br>**Effective milling time:** ~2 sec. per cantilever |

## 3.6 In-situ Electrochemical Cantilever Bending Setup

The in-situ microcantilever loading experiments were conducted on a Hysitron TI950 TriboIndenter system with an integrated miniaturized cylindrical Teflon cell, which was fitted to the nanoindenter sample holder. Three electrodes were used in the electrochemical setup, consisting of a counter-, working-, and a Hg/HgSO$_4$-reference electrode. In order to maintain the dimensional integrity of the cantilevers during the in-situ bending test it was important to

avoid local corrosion on the sample surface. A glycerol-based solution was therefore selected as the electrolyte for the electrochemical charging. The glycerol-based solution was saturated with borax (1.3 mol/l) and diluted with 20 volume percent water.

The sample was fitted in the cell so that the sample surface would be in contact with the electrolyte, then an o-ring was placed on top of it to prevent electrolyte leakage between the cell wall and the sample edge. A thin platinum disc had to be fitted around the top of the cell in order secure connection with the electrolyte and the counter electrode. Another o-ring was pushed over the platinum disc to prevent electrolyte leakage on the cell top. To enable a smooth connection between the platinum ring and the counter electrode, a thin platinum wire was led under the top o-ring and the platinum disc, from which the wire-ring connection was fixed underneath the ring. During the assembly of the electrochemical cell, it was essential to secure the all the fittings as tight as possible to secure the connection of the electrodes and prevent electrolyte leakage. When all the parts had been included in the cell, it was pushed into a machined hole on the sample holder. To improve the connection between the sample at the bottom of the cell and the working electrode, the sample holder hole was coated with a thin aluminum foil. The working electrode was then connected to the sample by clamping it onto one of the sample holder bolts. Subsequently, the reference electrode was connected to the cell by pushing a double junction polyethylene tube, containing electrolyte, into a hole on the cell wall. The whole system was positioned inside the chamber of the TriboIndenter. Solution was then injected into the cell from outside the chamber through the double junction polyethylene tube connected to a syringe. Consequently, one of the tubes in the double junction tube was utilized for the reference electrode connection, while the other was used for electrolyte injection. A schematic representation of the cell is shown in Figure 34 and Figure 35 shows the components installed inside the TriboIndenter chamber.

A potentiostat was utilized to control the voltage difference between the working electrode and the reference electrode, from which current was introduced to the cell through the counter electrode. The current flow between the working and counter electrode was then measured by the potentiostat. The microcantilever bending experiment was performed by charging the sample with a cathodic current of -200µAcm$^{-2}$ at -1500mV potential versus the Hg/HgSO$_4$-reference electrode during the test. Usually, after charging for one hour, the potential was decreased to -1400mV.
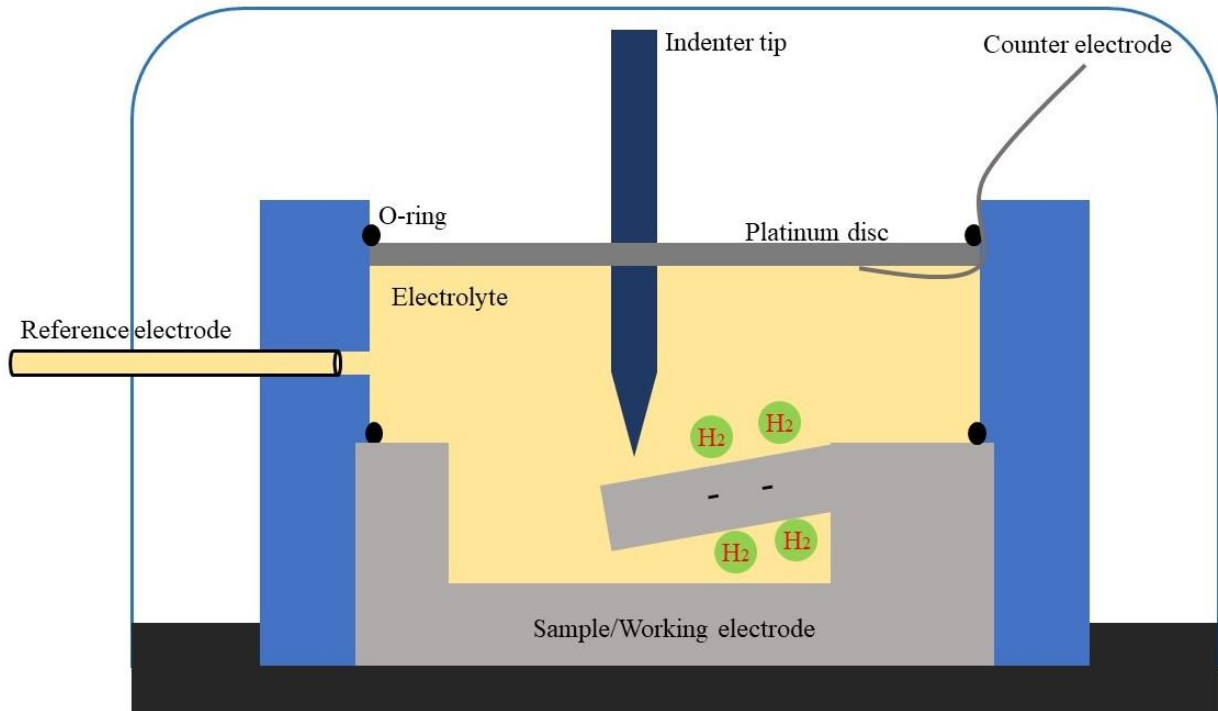
Figure 34: Schematic representation of the electrochemical cell for the in-situ microcantilever bending experiment.
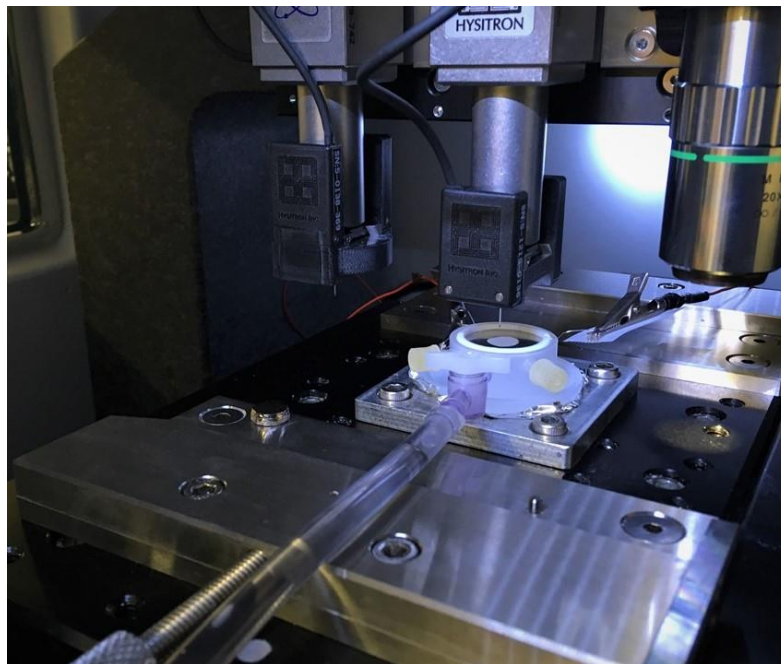


Figure 35: In-situ test setup inside TriboIndenter.

## 3.7 Thermal Drift Correction

One of the challenges during indentation was the irregular behavior of the indenter tip due to thermal drift. Thermal drift affects the overall precision of the indentation and varies, in most cases, according to temperature differences between the sample and indenter tip. During indentation, the thermal drift can be observed by the change in displacement signal even though the normal indenter force remains the same. Its effect arises due to changing thermal gradients from which the indenter tip expands or contracts. Consequently, the seemingly measured

displacement will not reflect the real force-displacement reaction of the sample material. In the case where the indenter tip initially has a higher temperature than the sample surface leads to a contraction of the indenter tip, resulting in a higher measured displacement than the true material reaction when loading is initiated. During the air bending tests at room temperature, the thermal drift was low, and it was expected that it would stabilize relatively rapid. However, when the sample was introduced to the electrochemical cell, there was a potential for elevated thermal gradients leading to expansion or contraction. This could then lead to higher drift rates, varying drift rates for each indentation and even increasing drift during testing. By scanning a surface region of the sample with the indenter tip for some time, the drift will decrease. This is because heat is transferred during the continuous contact between the sample surface and indenter tip, decreasing the temperature difference. It should, however, be mentioned that the temperatures may slightly vary from surface region to surface region, and the drift rate may therefore be affected if the indenter tip is moved to another area of the sample. Although scanning the sample surface with the indenter tip will decrease the drift, it will not be entirely removed.

To measure and monitor the thermal drift before the microcantilever air test and in-situ test a series of indents were performed on the sample surface, in the vicinity of the cantilever site, by using a conical tip. The indents were performed with a 1μN load and the drift was monitored for 200 seconds while the force was kept constant, before unloading followed. The last drift rate was then recorded before another indentation was performed. For each indentation a reduction in drift rate was desirable. Microcantilever testing was usually initiated when the drift rate had reached an acceptable value of ~ ± 0.1 nm/sec.

## 3.8 Cantilever Loading

The microcantilever bending test for both in-situ H charging and in air was carried out on the Hysitron TI950 TriboIndenter. To prevent sliding on the cantilever during testing, and thus enable larger displacements, the selected indentation tip was a specially designed conical tip with a long shaft and a nominal tip radius of 500nm.

As mentioned in section 3.5, to secure an accurate and safe approach to the cantilevers with the indenter tip a cross mark, aligned with the cantilever axis, was milled directly beneath the cantilever. By aiming the indenter at the center of this cross, the loading point on the cantilever could be safely accessed with a known vertical TriboIndenter stage movement. A vertical alignment of the cantilever axis according to the TriboIndenter optics was therefore essential, as shown in Figure 36 (a). In the case where the cantilevers have a small axis rotation relative to the vertical reference in the TriboIndenter optics, the approach from the cross mark to the cantilever loading point would have to be executed with an unknown vertical and unknown horizontal stage movement, as shown in Figure 36 (b), hence the approach would involve a much higher degree of uncertainty. Consequently, the cantilever axis orientation on the sample surface had to be determined. A microscope was used to determine the exact location and orientation of the cantilevers, from which the cantilever axis direction was indicated by marking the sample holder. The sample was then fixed on a magnetic stage and placed inside the TriboIndenter chamber according to the vertical alignment of the cantilever axis direction. The final air test setup inside the TriboIndenter chamber is shown in Figure 37.
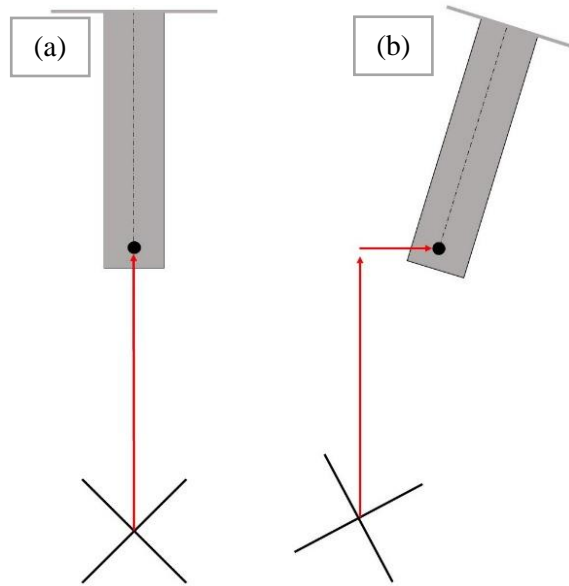
Figure 36: Cantilevers viewed in TriboIndenter optics. (a) Cantilever axis aligned in vertical direction for known vertical stage movement when approaching. (b) Cantilever axis rotated relative to vertical reference in optics, resulting in an unknown vertical and horizontal stage movement when approaching.
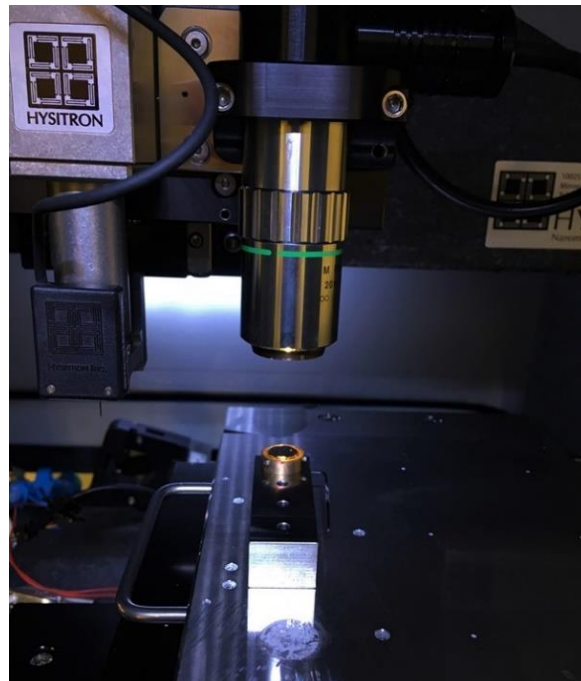


Figure 37: Test setup for microcantilever bending test in air

Before starting the tests, the indenter needed to be calibrated. First, the system was calibrated in order to verify that the transducer was operating properly and account for small alternations in transducer properties that may have been caused by temperature or humidity. Subsequently, the tip was calibrated according to the optics. The tip calibration was executed by seven, 4000μN indents in an H-pattern on a Ni calibration sample. After indentation, the calibration was finalized by shifting the center of the optics to the indent in the middle of the H-pattern.

The cantilevers on the sample were located with the TriboIndenter optics. Usually, when the cantilevers were located, a manual rotation of the sample on the magnetic stage was needed to perfectly align the cantilever axis with the vertical reference of the optics. The cantilever alignment in the TriboIndenter optics is shown in Figure 38. When the cross mark for the cantilever to be tested was centered in the optics, the surface was imaged using the indenter tip scanning probe. Initial scanning of the cross-mark area was executed with a relatively large scan size (20µm), and to secure that the tip did not drop into the cantilever pit during scanning, which potentially can damage the cantilever due to the tip's increasing thickness in the vertical direction, the scanning was set to move towards the pit with a scan rate of 1Hz. A gradual reduction in scan size allowed the indenter tip to be precisely positioned in the center of the cross. The loading point on the cantilever was then approached by a vertical stage movement according to the pre-defined distance between the cross-mark center and the cantilever loading point. To verify that the cantilever surface had been reached, a small surface scan of 0,1µm with a scan rate of 0,3Hz was performed. Loading was initiated once the indenter tip was accurately positioned in the center of the loading point.
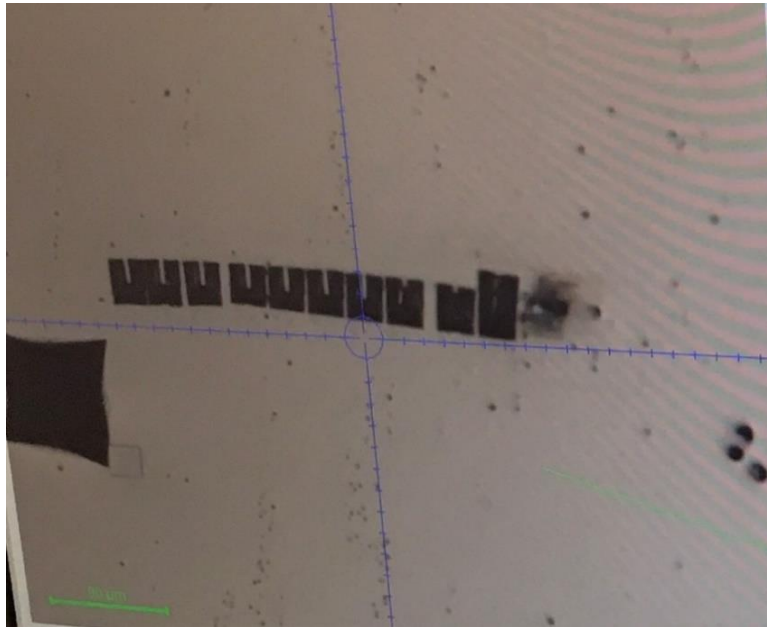


Figure 38: Cantilever alignment in the TriboIndenter optics.

For the in-situ experiment, the electrolyte was injected after the cantilevers had been aligned in the TriboIndenter optics and the indenter tip was positioned in the center of the cross-mark. Since the complex force transducer must be protected from the solution, it was necessary to remove any excess solution on top of the cell. After injection, the optics could no longer be used for navigation, as the electrolyte hindered visibility. All surface navigation had to be performed according to the indenter tip scanning and it was therefore essential to have an overview of which samples to test and their position relative to each other. Before the in-situ tests were initiated, the surface quality under the cathodic charging conditions had to be verified. The surface was imaged using the scanning probe and the recorded surface roughness was compared to the conditions during the air test. For all samples tested in-situ, the surface roughness was recorded to be intact when compared to the air test conditions, even under cathodic polarization.

The loading tests were performed under displacement-controlled indentation, with loading parameters defined in a load function. A displacement rate of 2nm/s with a segment time of 2475s was selected. For the corresponding peak displacement of 4950nm, the holding time was

set to 5s, followed by unloading with a constant displacement rate of 200nm/s. A partial load function with a displacement rate 2nm/s and peak displacement of 4950nm was also utilized in order to verify the material behavior. Each loading cycle had a segment time of 250s and thus ended after a displacement of 500nm. Similarly, a constant displacement rate of 200nm/s was used for each cycle unloading. After testing, a SEM was used to image the microstructure evolution in the vicinity of the notch of the SC cantilevers, while SEM images of the BC cantilevers allowed evaluation of the crack propagation path relative to the GB position.

The in-situ loading of cantilevers was carried out at different time intervals during the H sample charging. Additionally, to measure the effect of H trapping some of the cantilevers were tested in air after the H charging. An overview of the tested cantilevers for each sample and their respective test conditions are listed in Table 5. The cantilevers that are not mentioned was not tested due to damage or inaccurate dimensions.

Table 5: Test conditions of each cantilever and the respective sample.

| NiS | | | | |
|-----|-----|-----|-----|-----|
| **Bi-crystalline** | **Potential [mV]** | **Cathodic current [µAcm⁻²]** | **Displacement rate [nm/s]** | **Test specification** |
| Cantilever 3 | _ | _ | 2 | In air, 17 hours after H charge |
| Cantilever 4 | -1400 | -70 | 2 | In-situ, 2 hours of H charging |
| Cantilever 5 | -1400 | -70 | 2 | In-situ, 3 hours of H charging |
| Cantilever 6 | _ | _ | 4,5 | In air, 2 hours after H charge |
| Cantilever 7 | _ | _ | 2 | In air, 5 hours after H charge |
| Cantilever 8 | _ | _ | 2 | Air |
| Cantilever 9 | _ | _ | 2 | Air |
| **Ni** | | | | |
| **Bi-crystalline** | **Potential [mV]** | **Cathodic current [µAcm⁻²]** | **Displacement rate [nm/s]** | **Specification** |
| Cantilever 3 | _ | _ | 2 | Air |
| Cantilever 4 | _ | _ | 2 | Air |
| Cantilever 5 | _ | _ | 2 | Air |
| Cantilever 6 | -1450 | -80 | 2 | In-situ, 2 hours of H charging |
| Cantilever 7 | -1500 | -90 | 2 | In-situ, 3,5 hours of H charging |
| **Ni725 pre. hardened** | | | | |
| **Single-crystalline** | **Potential [mV]** | **Cathodic current [µAcm⁻²]** | **Displacement rate [nm/s]** | **Specification** |
| Cantilever 1 | - | - | 2 | Air |
| Cantilever 2 | - | - | 2 | Air |

# 4. Results and Discussion

A great number of cantilevers were milled in this project, as presented in Table 3 in section 3.5. Preparing and milling high-quality cantilevers is a time-consuming process and the access to the instruments needed for their preparation, fabrication and testing is limited due to their high demand. Consequently, the time frame of this project was unfortunately not enough to test all of them. This chapter will therefore focus on the cantilevers that were tested.

## 4.1 The Quality and Dimensions of The Cantilevers

The cantilever milling procedure was divided into several steps, as presented in detail in Table 4 in section 3.5. During milling, especially when the amount of material to remove was small, it was hard to control the exact material removal, and thus the material removal was hard to predict. Due to the small dimensions of the cantilevers, milling patterns had to be positioned with high precision, when even small pattern misalignments could promote significant deviation from the desired geometry. It was also essential to include safety margins in order to prevent excessive material removal. In other words, the final cantilever dimensions were principally a result of discreet milling adaptation. Therefore, each cantilever requires different handling, thus after each step in the milling procedure, the cantilevers must be carefully evaluated and modified. Despite handling each cantilever with precaution, the beam control complications resulted in some differences in the final dimensions of the cantilevers. Final dimensions of each cantilever are listed in Table 6. Images of the finished cantilevers, before bending, are presented in Appendix C: Cantilever images before and after bending. The height measurement of the cantilevers is based on the highest side edge, while the cross-section area is determined by the height, width, and the triangular bottom part. The length is measured from the notch to the loading point while the notch distance is measured from the cantilever base to the notch.

As discussed in section 3.5, different complications emerge when the cantilevers are pre-notched. Although pre-notching was executed with care and followed the same procedure it was not possible to prevent a slight difference in the notch depth on each cantilever side edge. An average notch depth was therefore determined by measuring the notch depth on each side. It should be mentioned that the sputtering rate influences the notch depth, in which sputtered material can freely depart from the areas close to the free cantilever edge. Consequently, the notch becomes deeper on the side edges than in the center of the cantilever. Furthermore, the crack tip could also be slightly affected by the beam control complications, from which the notch tip might get a small radius instead of being perfectly sharp.

Table 6: Final cantilever dimensions.

| NiS | | | | | |
|---|---|---|---|---|---|
| | Width [µm] | Height [µm] | Length [µm] | Notch distance [µm] | Average notch depth [µm] | Cross-section area [µm$^2$] |
| Cantilever 3 | 3,135 | 2,902 | 11,6 | 1,565 | 0,30235 | 11,8552 |
| Cantilever 4 | 3,038 | 2,897 | 11,98 | 1,538 | 0,3514 | 10,7645 |
| Cantilever 5 | 3,058 | 2,879 | 11,9 | 1,775 | 0,4466 | 11,0823 |
| Cantilever 6 | 3,077 | 2,835 | 11,71 | 1,583 | 0,327 | 11,1955 |
| Cantilever 7 | 2,962 | 3,065 | 11,9 | 1,602 | 0,66315 | 11,3145 |
| Cantilever 8 | 3,221 | 2,903 | 11,92 | 1,625 | 0,5198 | 11,8431 |
| Cantilever 9 | 3,087 | 3,101 | 11,85 | 1,558 | 0,49045 | 11,974 |

| Ni | | | | | |
|---|---|---|---|---|---|
| | Width [μm] | Height [μm] | Length [μm] | Notch distance [μm] | Average notch depth [μm] | Cross-section area [μm²] |
| Cantilever 3 | 3,462 | 3,125 | 12,10 | 2,018 | 0,2855 | 12,6208 |
| Cantilever 4 | 3,365 | 3,133 | 11,96 | 2,057 | 0,3593 | 12,5442 |
| Cantilever 5 | 3,365 | 3,069 | 12,04 | 1,999 | 0,28455 | 12,3317 |
| Cantilever 6 | 3,385 | 3,085 | 11,94 | 2,095 | 0,3678 | 12,5690 |
| Cantilever 7 | 3,385 | 3,077 | 11,94 | 2,114 | 0,3056 | 12,4894 |
| **Ni725 pre. hardened** | | | | | |
| | Width [μm] | Height [μm] | Length [μm] | Notch distance [μm] | Average notch depth [μm] | Cross-section area [μm²] |
| Cantilever 1 | 3,425 | 2,982 | 12,095 | 1,507 | 0,2725 | 12,3694 |
| Cantilever 2 | 3,423 | 2,998 | 12,195 | 1,975 | 0,2778 | 12,2041 |
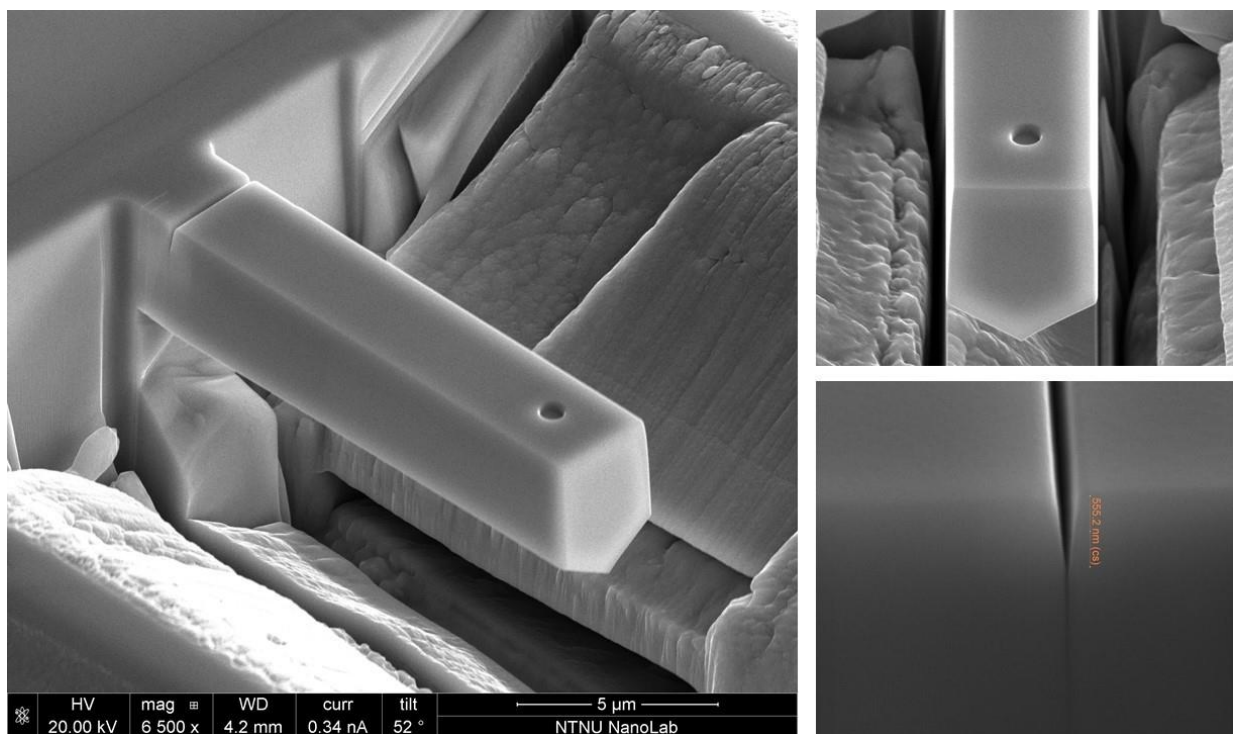


Figure 39: SEM image of finished cantilever with desired quality.

## 4.2 Loading

As the cantilevers are loaded, there is a possibility that the indent tip will pierce the surface of the sample. This can potentially influence the loading test as the resulting indentation depth becomes a significant part of the recorded displacement. Thus, the measured displacement might be a combination of indentation displacement and cantilever deflection. By investigating the cantilevers after bending in the SEM with corresponding load-displacement curves (L-D curves), it was, however, found that no surface penetration took place during loading.

In the following, the results from the cantilever loading test will be presented. SEM images after bending are shown for representative cantilevers, while images of all cantilevers after bending are presented in Appendix C: Cantilever images before and after bending.

### 4.2.1 Bi-crystalline Cantilevers

The load-displacement curves (L-D curves) of NiS microcantilever 8 and 9 bent in air is shown in Figure 40 and 41, respectively. L-D curves of the cantilevers charged by H are shown in Figure 42. Cantilevers in both test conditions display similar elastic behavior, while distinct differences are observed in the plastic regime. To highlight the effect of H, the plastic regime of the L-D curve will therefore be described in more detail.

Air and H tested cantilevers display continuous yielding but there is no observable difference in the yield point of ~200µN, except for cantilever 4 which starts to yield at ~160µN and is deformed under rather low loads. This might be due to a dimensional effect as cantilever 4 has a relatively small cross-section area compared to the others. After yield, the curves for the air tested cantilevers propagate until the load stabilizes at ~3µm displacement to the final displacement of 4.95µm, with a slight hardening rate recorded for cantilever 8. For both cantilevers, crack growth is indicated by small and sudden load reductions in the flow curve. Comparing the curves from air bending with the curves of the H-charged cantilevers shows a significant difference in material behavior. After yield, all H-charged curves propagate similarly (except cantilever 4), until a dramatic decrease in the flow curve occurs. The rapid decrease in load is most likely associated with a rapid crack propagation and reduction in the sample cross-section, which strongly indicates brittle failure. This occurs after a displacement of ~0.75µm for cantilever 4, 5 and 6, ~1µm for cantilever 7 and ~2.5µm for cantilever 3. Thus, a noticeable difference in fracture points is observed for the H-charged cantilevers, from which there is a clear relation between the fracture points and the level of H-charging. Cantilevers tested during H charging (4 and 5) shows limited deformation, while for cantilevers tested in air after H charging (6, 7 and 3) the amount of deformation increases with the time of air exposure after charging. As GBs are known trap sites for H [10], this behavior could be due to a varying amount of H trapped in the GB. During cathodic charging, H will continuously be trapped in the GB, whereas air exposure will allow the trapped H to escape, thus reducing the total amount of H present in the GB. Consequently, the longer the sample is exposed to air, the more H will escape from the GB. Assuming that H reduces the cohesive strength of the GB, lower amounts of H will therefore allow more deformation. Nonetheless, effects of H are observed for cantilever 3 by a rapid decrease in load even after 17 hours of air exposure after charging, presumably caused by H still trapped in the GB. Furthermore, results from the bending experiment of H-charged NiS cantilevers clearly indicate that the longer the sample is exposed to air after it has been charged by H result in increasing fracture loads. For cantilever testing in air 17 hours after H-charging, the fracture load reaches a value of ~650µN, at which immediate fracture occurs. This value is significantly higher than ~450µN, which is the highest load value recorded from the H-free condition. Usually, it is expected that the flow curve of H-charged cantilevers, at some displacement, will start to decrease rapidly until final failure occurs

at load values lower than for cantilevers bent in air [56]. The reason the flow curves of the H-charged NiS cantilevers do not rapidly decrease to lower load values before final failure is hard to verify and explain from the observations of only one test. At first, this behavior was thought to be a consequence of thermal drift, where the indenter was compensating the deviation in displacement by applying additional force onto the cantilever. However, this is most likely an unreasonable explanation. Although the recorded displacement can be wrong, this should not affect the recorded loads since load is defined by the indenter and measured directly on the cantilevers. Therefore, the observations from the NiS H testing could be due to an underlying mechanism caused by H.
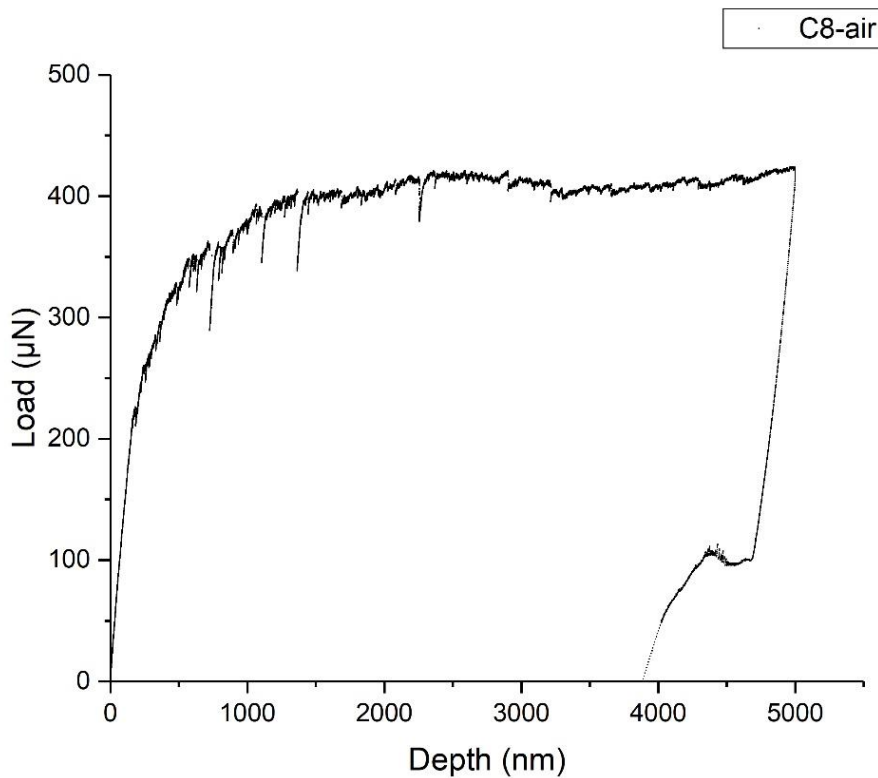


Figure 40: L-D curve for NiS cantilever 8 tested in air.
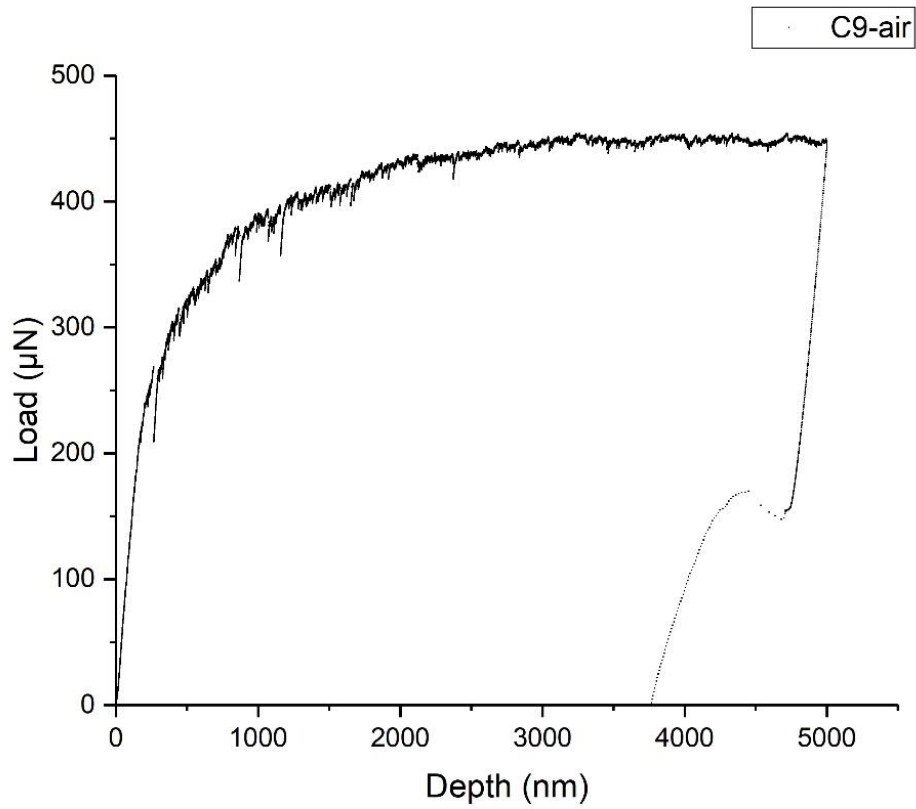
Figure 41: L-D curve for NiS cantilever 9 tested in air.
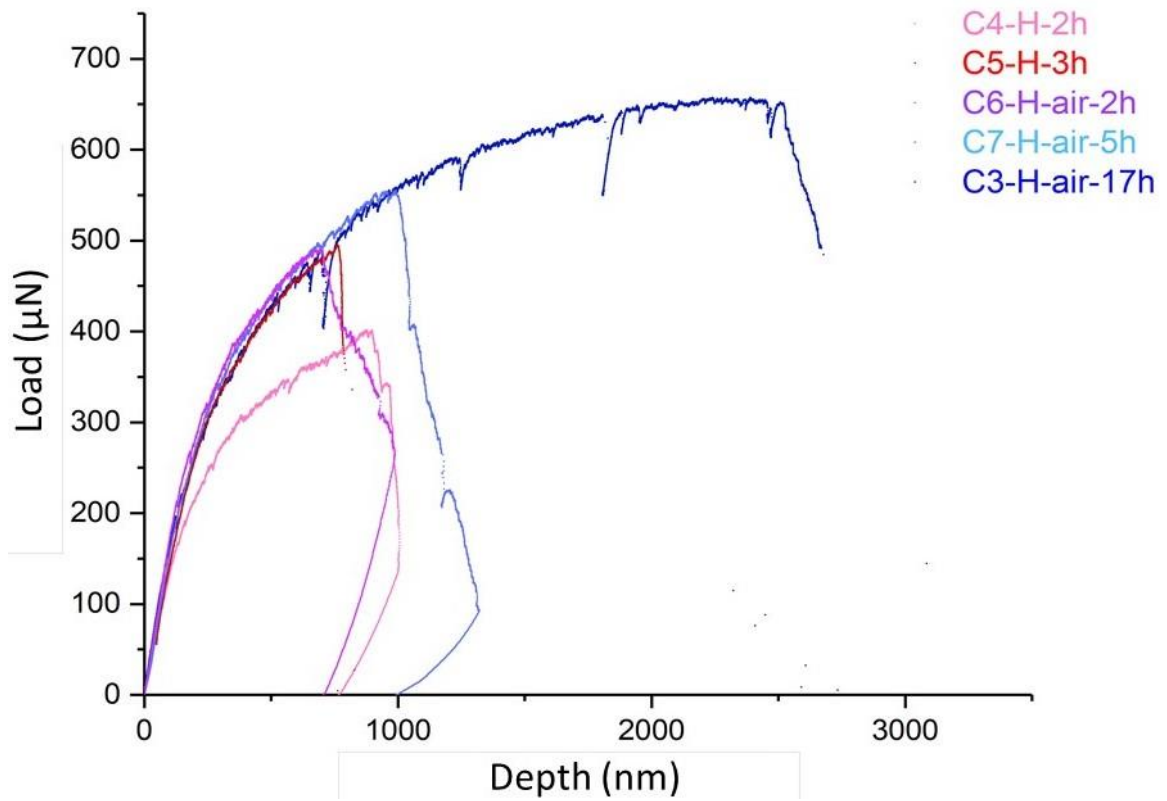


Figure 42: L-D curves for NiS cantilevers tested during cathodic charging (4 and 5), and in air with increasing air exposure times after H charging (6, 7 and 3).

The SEM images in Figure 43 shows a representative NiS cantilever that was bent in air (a) and one that was charged by H (b). For cantilevers bent in air, there is a crack blunting at the notch tip and several slip traces are observed on the deflecting region of the cantilever, while no distinct slip traces are present on the support region. The interesting observation is the slight opening of the GB some distance away from the notch tip. However, for the H charged cantilevers, the GB has completely opened and there is no sign of crack propagation from the notch tip. Slip traces are also not as evident when compared to the cantilevers bent in air.
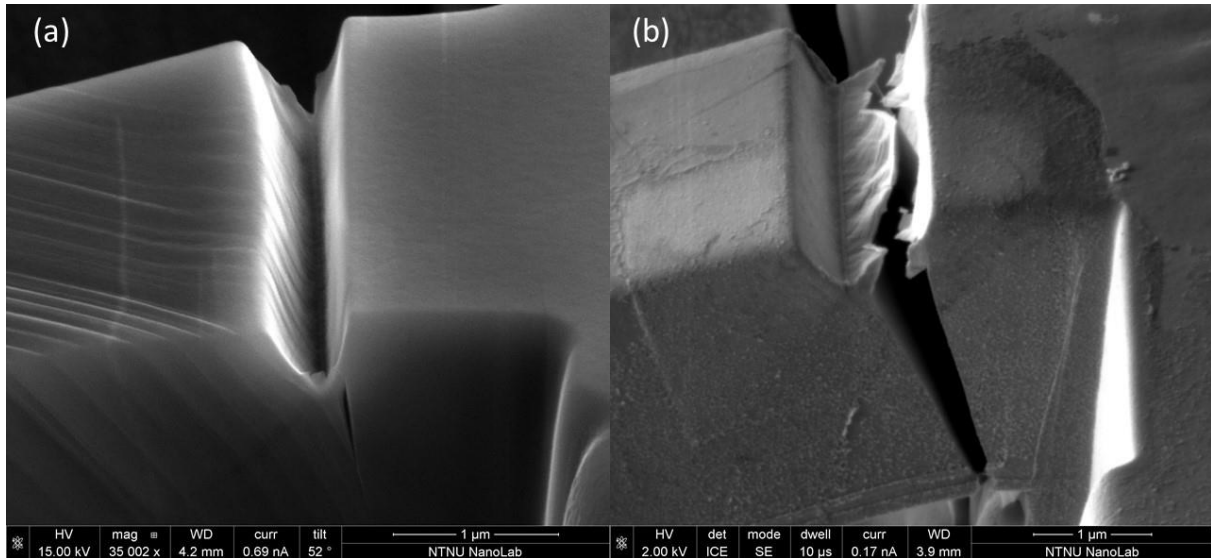


Figure 43: Representative NiS cantilevers after bending test in air (a) and after H charging (b).

A closer view of the notch area and the crack propagation path relative to the GB is shown in Figure 44. After the air test (a), the crack propagation follows the GB plane and leads to a sharp and straight GB opening, and when the crack approximately reaches the neutral axis of the cantilever the propagation ends. This is most likely due to the accumulative dislocations caused by the high compressive stresses in the zone beneath the neutral cantilever axis. Interestingly, the observed crack propagation along the GB plane shows no dependence on the notch position. The crack for the cantilevers bent in the H environment (b) shows clean and consistent cleavage along the GB plane, from which the GB has completely opened. For this case, it is also observed an independent relationship between the crack propagation path along the GB plane and the position of the notch. This implies that there is no distinct dependency of the stress concentration position relative to the GB plane. Normally, when a crack is initiated it selects the plane with the lowest energy as favorable for crack propagation. Consequently, the crack path can be interrupted which results in a zig-zag formed pathway [56]. Since the observed crack paths in both cases are consistent along the GB, indicates that the GB plane is the plane with the lowest energy and is thus favorable for crack growth.
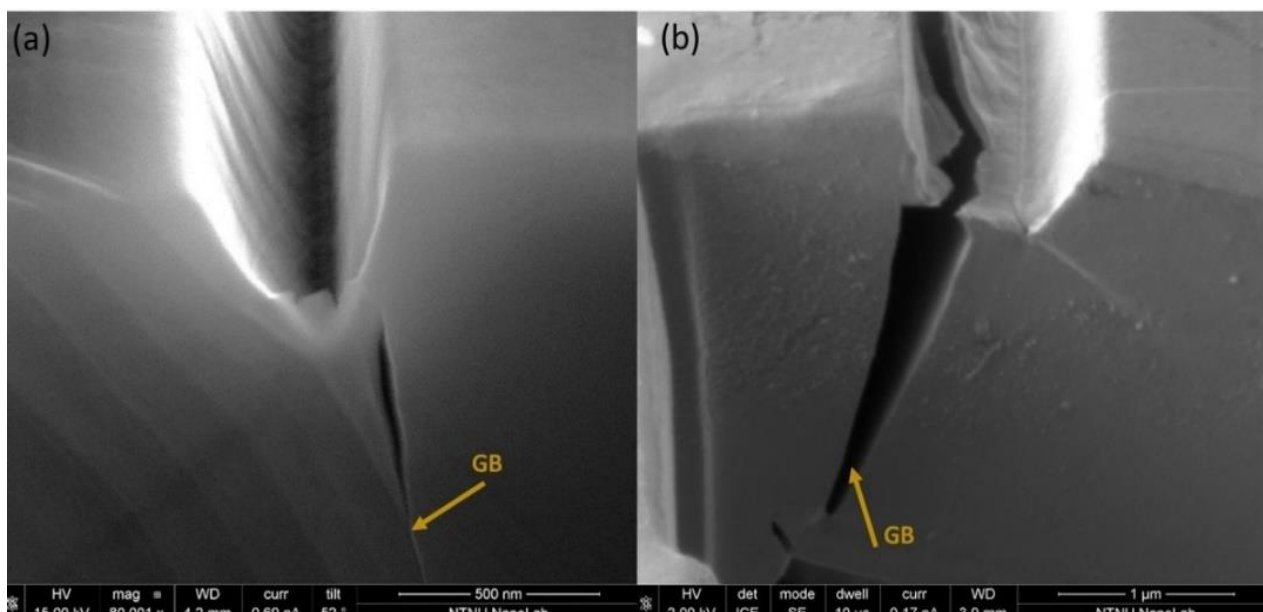
Figure 44: Notch area of NiS cantilever bent in air (a) and charged by H (b).

Figure 45 shows the L-D curves of the pure Ni BC cantilevers bent in air and under H charging. The air tested cantilevers 3 and 4 yields at ~250µN followed by a continuous increase of work hardening until a displacement of ~2.5µm. Then, the slope of cantilever 4 slowly decrease until unloading at 4,95µm, while the slope of cantilever 3 remains constant with lower load values. Although the difference is small, it is most likely related to some small differences in the cross-sectional notch depth or caused by indenter tip gliding on the cantilever surface during indentation. Partial loading of cantilever 5 was conducted in order to verify the material behavior from the air tests with constant loading. For this curve, a continuous increase of work hardening until a displacement of ~0.5µm is observed. Then a rapid decrease in load occurs, which might be due to crack propagation. However, when the cantilever was examined in the SEM after bending there was no observation of crack growth, from which the crack might have propagated within the cross-section of the cantilever and a cross-section cut will therefore be necessary to observe the crack path. After a displacement of ~2µm, the curve propagates under a constant load with a slight work hardening rate to the final 4,95µm displacement. There is a slight difference when comparing the flow curves of the partial and constant loading tests in air. This is most likely due to the extensive amount of unloading after each load cycle which almost causes a total load release. As the material is repeatably exposed to these large load intervals, it is slowly fatigued and will thus deform under slightly lower loads. The L-D curves for H charged cantilevers shows a similar yield point as the air curves, but after yielding the H charged curves reaches slightly higher loads. For the H-charged cantilever 7, crack propagation is indicated by a drastic decrease in load after a displacement of ~2µm. Although charged by H, cantilever 6 do not display a similar load drop. The load starts to drop at ~1µm and stabilizes at ~400µN after a displacement of ~2µm. However, at displacements of ~2.5µm and ~3µm a sudden increase and drop in load is observed in the flow curve, before the load stabilizes again. This is most likely due to dislocation pile-ups pinning further dislocation movement and in order to "unlock" these dislocations the stress needs to be raised to a certain value. When the load reaches the value that corresponds to this required stress the dislocations are unpinned, and the dislocations will again move at the stabilized load.
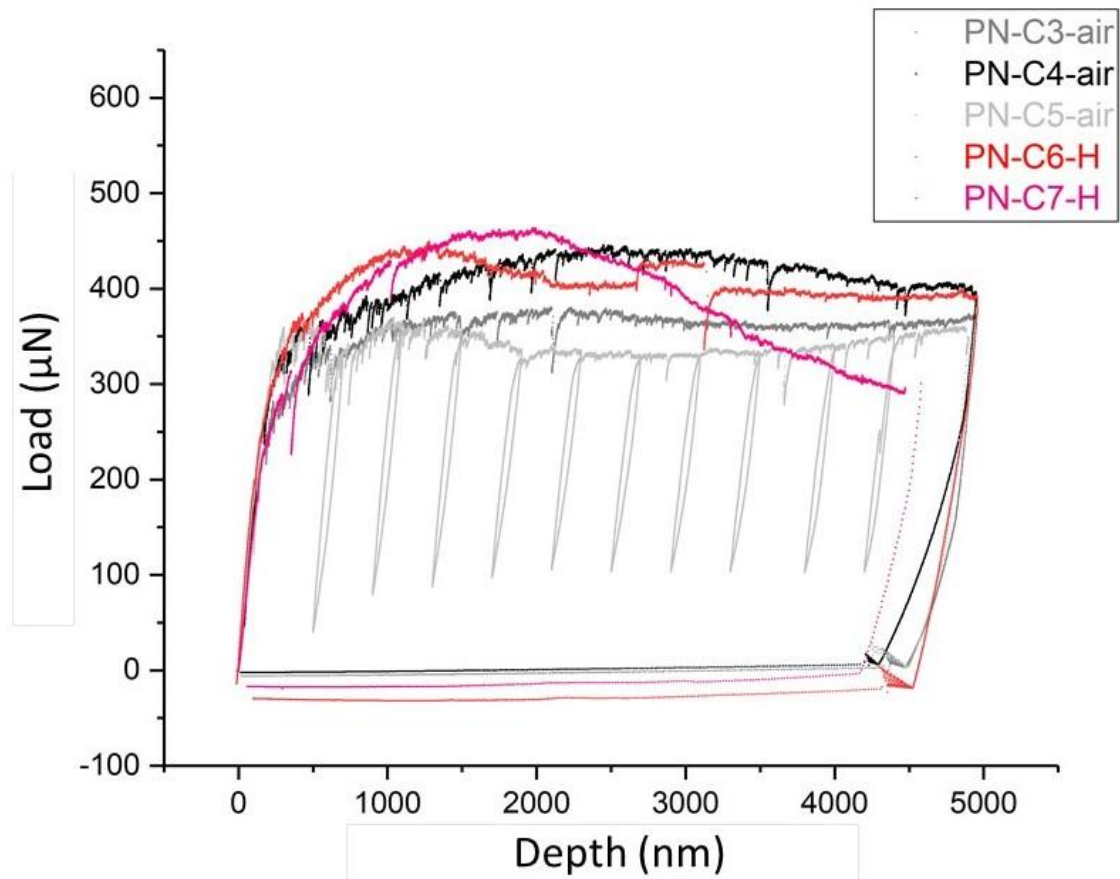
Figure 45: L-D curves for pure Ni cantilevers tested in air and charged by H.

Figure 46 shows one representative pre-notched pure Ni cantilever bent in air (a) and one pre-notched charged by H (b). Crack blunting at the notch tip together with distinctive slip traces in both support and deflect regions are observed for the pre-notched cantilevers bent in air. In contrast, a very sharp crack is observed for the pre-notched and H charged cantilevers, while slip traces are not as clear as that of the cantilevers bent in air.
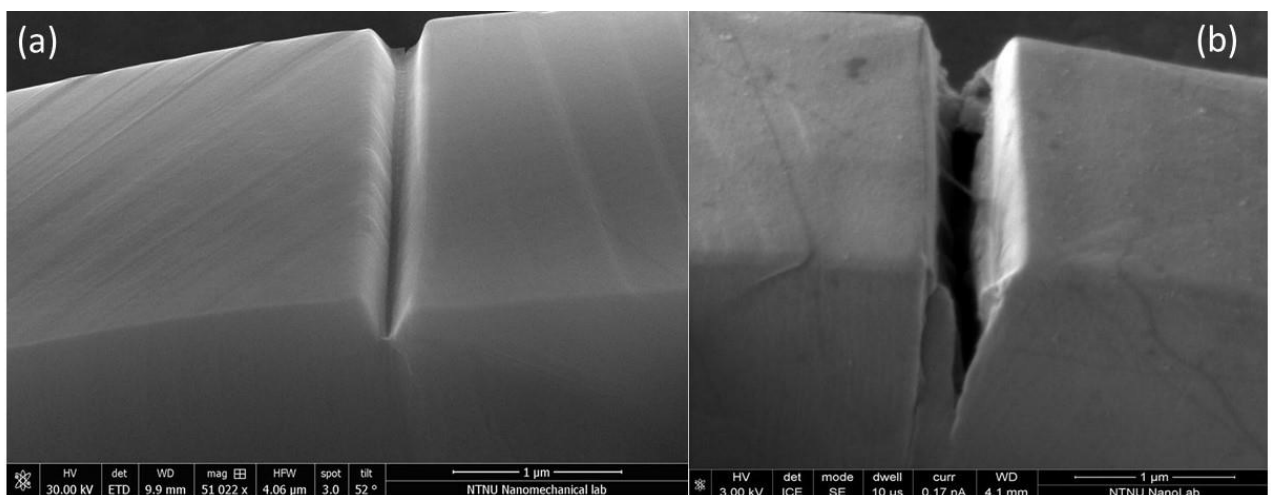


Figure 46: Ni cantilevers: representative bent in air (a) and representative after H charging (b).

The crack path relative to the GB for a representative pre-notched cantilever charged by H is shown in detail in Figure 47. As shown, the crack propagation results in a sharp opening. It stops after a distance of ~500nm from the notch tip, which implies that tensile stresses after this

point are not high enough to promote further crack growth. However, when comparing the propagation path to that of the NiS cantilevers, a clear difference is observed. While propagation paths for NiS cantilevers clearly follow the GB plane, there is no observation of crack growth along the GB for the Ni cantilevers. Instead, the crack grows with a deviation from the GB towards the deflecting region of the cantilever. The observed path deviation from the GB plane might be due to a dependency of the notch position relative to the GB. Consequently, if the notch is milled a small distance off the GB, the propagation path will deviate from the GB plane [56], while a more accurate notch positioning on the GB might promote crack growth along the GB plane. Clearly, the crack is initiated from the notch tip and grows in the crystal along the favorable plane with the lowest energy. This could explain why the crack pathway seems slightly interrupted and has a zig-zag form.
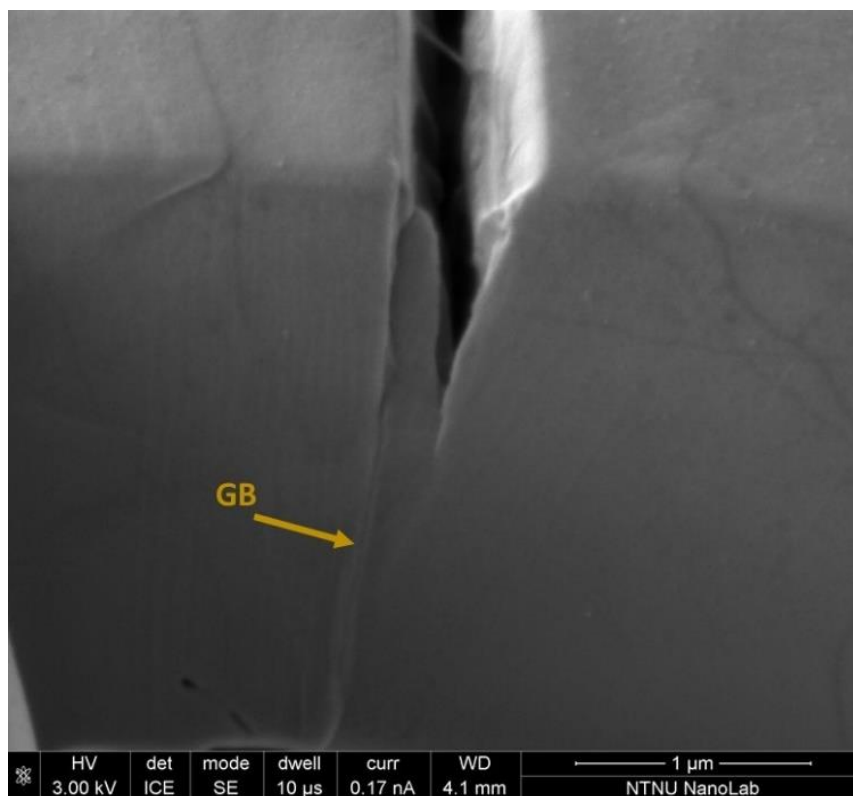


Figure 47: Notch area of Ni cantilever charged by H.

SEM images after the NiS and Ni air experiments display that there is a difference in the material behaviors. When comparing the L-D curves from the air tests, the recorded yield point for pure Ni is slightly higher than for NiS, but the flow curves are rather similar. In the literature, it is discussed that the segregation of S (sulfur) to GBs will alter the mechanical properties of Ni. Lee et al. [57] proposed that the failure mechanism of NiS when S segregates at the GB will be a combination of intergranular and transgranular fracture in which intergranular fracture is the dominant mechanism. It was stated that the main effect of segregated S at GBs exposed to stress involves the change in failure mode from transgranular failure along slip bands to intergranular failure along GBs. There is a competitive relation between the slip transfer across the GB, leading to ductile transgranular failure, and intergranular failure. One or the other can cause a reduction of the stresses that are developed by pile-ups at the GB. When S is segregated to the GB, dislocations will be blocked at the GB. This results in a dislocation pile-up and cracks will then nucleate at the junction of the pile-ups with the GB and start to grow along the GB. If S segregation at the GB leads to a reduction of slip transmission through GBs, the failure mode becomes intergranular. However, this is not an entirely brittle process due to the involvement

of dislocations in the initiation of the crack which are ejected from the region of the crack tip during crack propagation. The predominance of intergranular failure in the experiments was understood if the segregation of S leads to a reduction in the GB's cohesive strength and thus reduces the stress needed for intergranular failure below the stress needed to manage GB dislocation sources i.e. transgranular failure. A distinct difference was observed when pure Ni was deformed. This deformation was said to be purely transgranular since GBs provided little resistance to deformation bands and to the transgranular cracks propagating along them. A similar S effect on the GB was reported by Yamaguchi et al. [58]. From first-principles calculations, it was found that densely segregated and neighboring S atoms leads to a large GB expansion. They explained that as the amount of S increases, the GB expansion will increase and thus result in a drastic GB decohesion which significantly reduces the GB's tensile strength. In general, these observations are in good agreement with the experimental results of bending tests performed in air for the NiS and Ni samples. According to the report, the reason for crack propagation along the GB plane in the NiS sample is due to a sufficient amount of S segregation in the GB, which might reduce the GB's cohesive strength and promote the intergranular cracking.

There is also a marked difference of the test results when the two samples are introduced to H. For the NiS sample, the cantilever fracture has resulted in a clear opening of the GB. As discussed in section 2.1.3.1, it is well known that GBs become trap sites for H when H is introduced to a polycrystalline metal [10]. Furthermore, it is a reason to believe that this trapping effect becomes more significant in a metal with an FCC structure, such as Ni, than a metal with a BCC structure since the FCC structure has lower H diffusivity [5], as discussed in section 2.1.2. Consequently, it is harder for H to enter the FCC structure, but when it enters it does not escape as easily as in BCC structures. However, when comparing the L-D curves of the H-charged pure Ni and NiS there is a clear difference in the flow curve reduction. The reduction is much more pronounced and sudden for the H-charged NiS sample than for the pure Ni sample. Furthermore, the flow curve reduction of the NiS cantilevers tested during cathodic charging occurs at much lower displacements than for the in-situ tested cantilevers of pure Ni. In the literature, it has been discussed that H not only restrains the mechanical properties of a material but might also change the failure mode from ductile micro-void coalescence to a more brittle intergranular fracture [59]. Bruemmer et al. [60] investigated the effect of sulfur in promoting intergranular embrittlement in combination with H on Ni. In the experiments, it was found that the Ni ductility and failure mode depended on the cathodic test potential as well as the composition of the GB. A more rapid loss in ductility was observed with increasing coverage of S in the GB and increasing cathodic potential promoting more H. S was established as the element responsible for the intergranular embrittlement and a synergetic interaction between the S segregant in the GB and H was said to promote the change in failure mode to intergranular and rapidly decrease the ductility of the material. Furthermore, HEDE was suggested as the driving HE mechanism for the H enhanced cracking. H and S act individually to decrease the GB's cohesive strength, and when the effects of these elements cause the cohesive strength to fall beneath a critical value the transition from transgranular to intergranular failure will occur. The amount of each element needed to promote this brittle transition was explained by a direct cooperative relationship between H and S, in which an increase of H will reduce the necessary amount of S, and vice versa. While the driving HE mechanism for the transition in failure mode to intergranular failure is not conclusive, similar observations of intergranular failure in the presence of H has been reported [61]. McMahon [20] also reported that H-assisted intergranular brittleness largely depends on the amount of segregated impurities in the GB. It is claimed that when there is not a sufficient amount of segregated impurities at the GB, H will lead to increased cracking at elevated stress levels by concentrated plastic flow. Hence, since this is not observed in the results of the NiS cantilever

tests in H, there is a reason to believe that the observed intergranular brittle failure is enhanced by the presence of H and that there is a sufficient amount of S segregants in the GB. In other words, HE and intergranular failure seems to be more likely when S is segregated to the GB. The reason for this might be explained by comparing the observations of the NiS sample and the pure Ni sample. Similar crack growth observations as in this work were reported by Robertson et al. [62] after investigating the effect of H on the dislocation structure in pure Ni. When the sample was deformed in an H environment, the failure occurred in the vicinity of the GB. The crack did not grow along the GB plane, instead, it propagated within the boundaries of deformation lines that followed the outline of the GBs. From these observations, it was stated that when H was introduced to pure Ni, the transgranular failure mode was not as clear as that for pure Ni in an H-free environment, suggesting that H might influence the transition in failure mode. However, through an atomistic study of HE of various GBs in pure Ni, Tehranchi and Curtin [63] stated that the presence of H at the GB has a negligible effect on cohesion. In fact, no tendency for H to cause a transition from ductile to brittle cracking along GBs was found. It was concluded that HE observed in pure Ni is presumably not associated with the segregation of H along GBs, hence embrittlement is most likely connected with processes in which H is transported through the bulk of the material or along GBs. Similar effects have also been reported for H segregation to GBs in pure iron [64]. On the other hand, the effect of H on the failure mode might be dependent on the amount of H present at the GB. Wang et al. [59] used density functional theory calculations to study the separation energy on different types of GBs in iron. It was shown that for low chemical potentials of H only a small portion of the potential sites within the GB would be filled with H. Consequently, with limited site filling i.e. little amount of H present in the GB, the failure mode would usually be transgranular.

The results from the experiment in this work are in good agreement with the observations in the literature. The reason the crack path in the H charged NiS cantilevers consistently follows the GB plane is due to the synergetic relationship between S and H, resulting in a reduction in the GB's cohesive strength. Clearly, there is a critical amount of either H or S present in the GB, which might explain why the intergranular cracking is the dominant failure mode in the NiS experiments. When comparing the results from the air test and during cathodic charging, it is strongly suggested that H contributes to the transition from ductile to brittle cracking along the GB and the effect seems be reinforced by the segregation of S. Furthermore, among the proposed HE models, it is reason to believe that the H-enhanced decohesion (HEDE) mechanism is the most relevant when including a GB in the cantilever test. For the pure Ni charged by H, the absence of intergranular failure might be explained by an insufficient H amount within the GB in which only a small fraction of the potential sites in the GB has been filled with H, and thus resulting in transgranular failure.

4.2.2 Single-crystalline Cantilevers

The L-D curves of air tested cantilevers on the precipitation hardened Ni725 super-alloy are shown in Figure 48. Cantilever 1 was constantly loaded, while cantilever 2 was partially loaded. Both L-D curves exhibit continuous yielding with a yield point of ~1100µN. After yielding, there is a continuous increase of work hardening until a displacement of ~1.5µm, at which the flow curves propagate with a slight softening rate until the final displacement of 4.95µm. When cantilever 2 reaches the maximum load, sudden load drops are observed followed by deformation under slightly lower loads than cantilever 1. Usually, one would consider this as an indication for crack propagation. However, there is no decreasing tendency in the curve inclinations after each unloading, thus there is no indication of accelerated cracking. Since the dimensional parameters of the two cantilevers are similar, the sudden load drops are most likely associated with the cyclic loading that slowly causes fatigue and gradually weakens the material, resulting in deformation under lower loads.
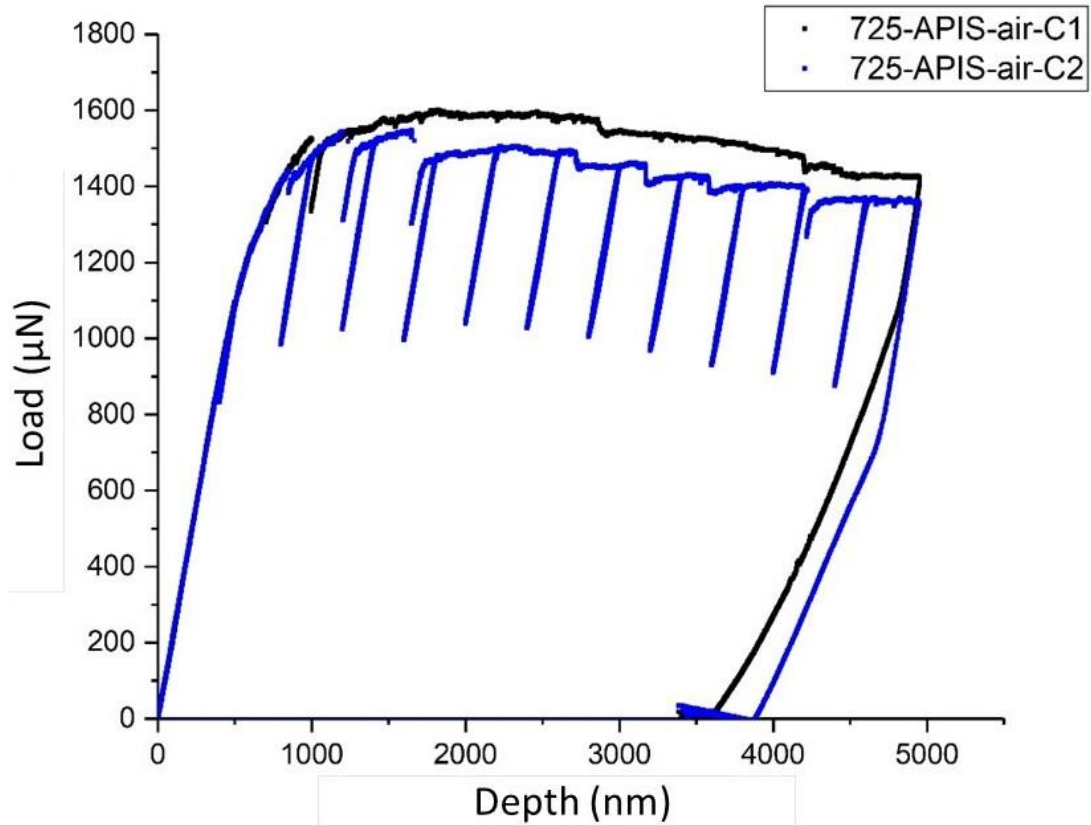
Figure 48: L-D curves for precipitation hardened Ni725 cantilevers tested in air.

Figure 49 shows one representative precipitation hardened Ni725 cantilever bent in air. Only a slight notch blunting is observed after the test, while distinct slip traces are visible in both the deflect and support regions of the cantilever. Closer examination of the notch area reveals that the slip bands are significantly elevated relative to the surface. This phenomenon is associated with the interstitial precipitation elements pinning the existing dislocations, which will cause the dislocations to pile up. Subsequently, the dislocation pile-up will prevent further dislocation movement i.e. deformation, and a certain level of stress in the cantilever has to be reached in order for the dislocations to be unlocked. When this stress level is reached, the dislocations are released, and they will thus start to move. However, since the recorded loads of the precipitation hardened Ni725 cantilevers are significantly high, the stress levels involved in the cantilever bending will be high. Consequently, as the dislocations are released under such high stresses, there will be a marked elevation in the slip bands, as observed in Figure 49.

| HV | mag ⊞ | WD | curr | tilt | ⊢———— 1 µm ————⊣ |
| 20.00 kV | 35 000 x | 4.2 mm | 0.69 nA | 52 ° | NTNU NanoLab |
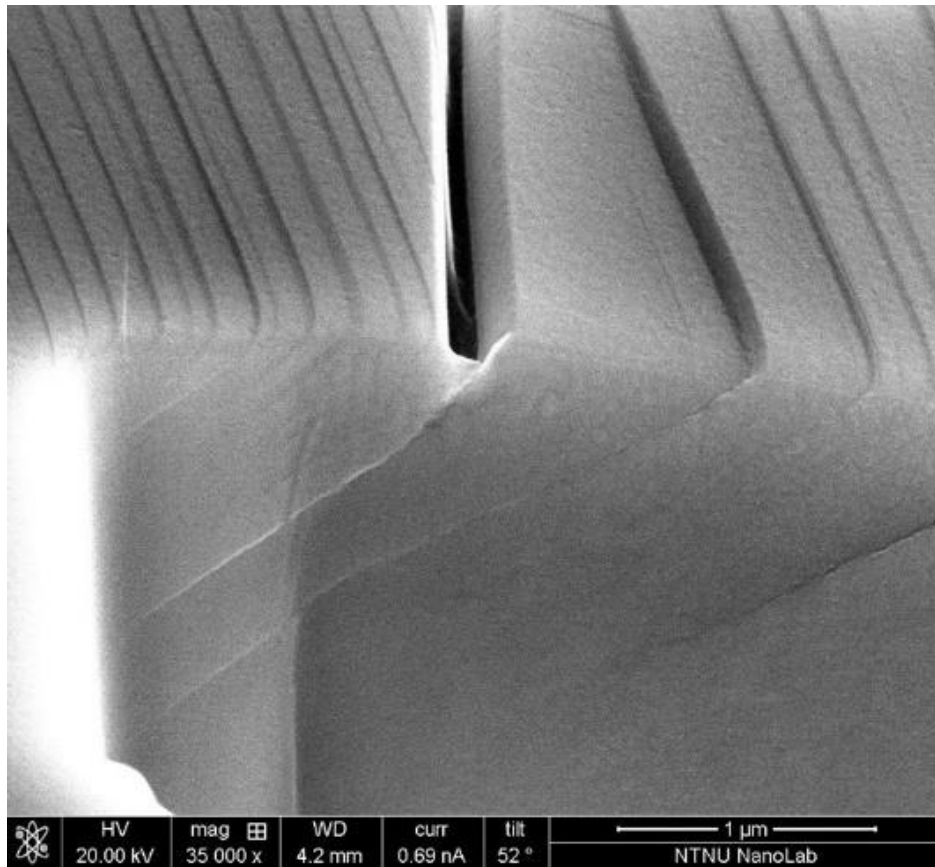
Figure 49: Representative precipitation hardened Ni725 cantilever bent in air with elevated slip bands caused by dislocation pile-ups.

The precipitation elements significantly strengthen the Ni725 alloy. Compared to the BC pure Ni cantilevers bent in air, the SC cantilevers on the precipitation hardened Ni725 clearly deforms at much higher loads, in which the yield point is ~850µN higher for Ni725. However, the flow curve of the super-alloy displays a slow but consistent load drop from ~1600µN to ~1400µN at the final displacement, while a more stable load behavior is observed for pure Ni. Xiao et al. [65] studied the effect of precipitates on a Ni-containing Inconel 718 alloy during cyclic loading. In this work, it was found that fatigue at room temperature caused the formation of planar deformation bands and that coherent and ordered precipitates was sheared by paired dislocations during cyclic deformation. Formation of planar slip in alloys are often attributed to their low stacking-fault energy (SFE). Low SFE result in wider extended dislocations with a decreased ability of screw dislocations to cross-slip to other slip planes. It is therefore stated that planar slip in alloys are often dependent on their SFE. The planar deformation bands were observed to have a great slip concentration occurring within the slip bands on all slip planes, where the slip bands penetrated the whole grains. It was observed that the cyclic deformation reduces the size of the precipitates and it was stated that as the cyclic deformation proceeds, the strengthening precipitation elements which are situated in the slip bands will be sheared by the leading dislocations. After these dislocations have cut the precipitates, the following dislocations in the same slip plane will shear the precipitates again. As this process is repeated for each cycle, the size of the precipitate will be reduced to a critical size at which they will contribute to little or no resistance to dislocation movement. Hence, as the shearing of particles by dislocations continues, the needed stress to shear the resulting small particles decreases. The favorable paths for dislocation slip are the paths with lower critical stress and will consequently

be established during the progressive material deformation. This will ultimately result in the production of precipitation-free planar bands. Furthermore, it was stated that deformation can take place by further emission of dislocations from the same dislocation sources or by the activation of new sources on parallel planes. It was also found that the width and spacing of the planar slip bands were almost independent of the amplitude of the cyclic plastic strain, and that the paired dislocations cannot cross-slip, which implies that slip is primarily concentrated within planar slip bands.

Based on the reported observations and statements in the literature, the slight softening in the flow curve for the precipitation hardened Ni725 cantilever might be due to the repeated shearing of precipitation elements by paired, leading and trailing, dislocations within the slip bands. This will cause the size of the precipitates to decrease, which will reduce the required stress for further precipitate shearing and thus establish favorable paths for dislocation slip during the deformation. Furthermore, the observed planar slip bands could be due to the alloy having a low SFE, which leads to wider extended dislocations with a reduced capability of screw dislocations to cross-slip to other slip planes.

# 5. Conclusion

In this project, fabrication and testing of microcantilevers have been conducted to study the effects caused by the introduction of H in Ni and Ni alloys. Samples were thoroughly prepared and electropolished to obtain high-quality sample surfaces, while EBSD analysis was conducted to characterize the surfaces and locate ideal sites for cantilever fabrication. A total of 7 samples were prepared, and, depending on the grain size, a number of 6, 8 or 10 bi-crystalline or single-crystalline cantilevers were milled on each sample. Among the 7 samples, only BC cantilevers on the pure Ni and NiS samples and SC cantilevers on the precipitation hardened Ni725 were tested, due to time limitations. Cantilever loading was successfully conducted in air and during cathodic charging in a TriboIndenter, and the electrochemical cell for the in-situ nanomechanical testing is an effective method, suitable for analyzing the effect of H at the microscale.

A microcantilever production procedure has been established by utilizing a dual beam. High-quality surfaces and low geometry variations were obtained by gradually reducing the ion beam current throughout the milling process, in which high currents were used for the initial rough milling, while low currents were used in the final milling steps. Furthermore, the effect of re-deposition was significantly reduced by gradually decreasing the material removal. The use of a dual beam, which combines a FIB and SEM, has shown to be a valuable tool for the micro- and nanoscale material removal, offering the opportunity to observe the local material behavior and increase the understanding of the underlying mechanisms of HE. To maintain the progress of the current industry and research, such advanced nano instruments is a clear necessity, and being able to conduct material fabrication trough precise nanomachining is important to the progress of material science.

Mechanical loading of BC cantilevers has studied failure mechanisms as a function of the alloying element, the presence of H and the GB. Fracture did not occur for BC NiS cantilevers tested in air, but cracks propagated along the GB plane, suggesting that there is a critical amount of S segregants in the GB. S segregation to the GB causes a reduction in the GB's cohesive strength, which will reduce the stress needed for intergranular failure below the stress needed to operate GB dislocation sources i.e. transgranular failure. With increasing amounts of H present in the GB, the intergranular failure is accelerated. It is therefore proposed that H accommodates the transition from ductile to brittle cracking along GBs. However, since the H-charged pure Ni cantilevers do not exhibit intergranular failure, it is found that the H-induced intergranular brittleness is strongly dependent on the amount of impurities segregated to the GB. There exists a synergetic relationship between S and H leading to GB decohesion, and when there is a critical amount of either S or H present in the GB the intergranular cracking will be accelerated. Thus, when GBs are involved, the H-enhanced decohesion (HEDE) mechanism is the most relevant among the proposed mechanisms for H-assisted cracking.

# 6. Further work

In this project, an extensive number of cantilevers have been produced for bending experiments in air and in the presence of H. As mentioned earlier, the time frame of the project was unfortunately not enough to test all of them. In the following, a list of further research will be proposed based on the production and results obtained in the project.

- There are still 4 sample materials with cantilevers that should be compared by bending tests in both air and H. The samples include; solution annealed Ni725 with SC cantilevers, solution annealed Ni725 with BC cantilevers, over-aged Ni725 with SC cantilevers and solution annealed Ni718 with SC cantilevers. The number of cantilevers on each sample are 6 or 8 (see Table 3 in section 3.5).

- The remaining cantilevers on the precipitation hardened Ni725 need to be tested in-situ. In this way, it becomes possible to observe and quantify the effect of H in the super-alloy. The results should be compared with the results obtained from the air test in this work to see if the introduction of H alters the deformation behavior and to observe a potential ductile to brittle transition.

- It is also suggested to conduct further H testing on the NiS sample in order to quantify and verify the experimental findings in this work. A consistent increase in load values is observed for the cantilevers that have been exposed to air for longer periods after being charged by H. These values are significantly higher than the load values recorded during the air bending, at which fracture occurs suddenly without any warning in the form of a rapid decrease in the flow curve. Usually, it is expected that the flow curve for H-charged cantilevers, at some deflection, will start to decrease to load values which are lower than for cantilevers bent in air. The possible underlying mechanism that causes this material behavior in NiS when H is present should be investigated further. Cantilevers should be tested after even longer air exposure times after H charging, to see if this effect is persistent.

- Representative cantilevers from the bending tests should be selected for further cross-sectional EBSD characterization. By obtaining a kernel misorientation (KAM) map from the EBSD analysis, it is possible to observe the sudden changes in the geometrically necessary dislocations density and can provide valuable information on how H alters the cantilever deformation.

# 7. Acknowledgements

This project has been a fascinating and very interesting journey, allowing me to acquire a great amount of knowledge in a short period of time. It has also been challenging and I would like to take this opportunity to thank the people that have guided me along the way.

- First, I will thank my supervisor professor Afrooz Barnoush for his enthusiasm and encouragement. He has shown great interest in this project and guided med throughout the work.
- I would also like to thank Ph.D candidate Tarlan Hajilou for her guidance and availability. Her great knowledge of hydrogen embrittlement and expertise within nanomechanical testing has offered the opportunity for productive discussions that provided new ideas and challenged my thinking.
- Employees at NTNU NanoLab and at the Department of Engineering Design and Materials are also gratefully acknowledged for guidance with the laboratory equipment.

# 8. Bibliography

1.  Barnoush, A., *Hydrogen embrittlement, revisited by in situ electrochemical nanoindentation*.
2.  Oriani, R.A.H.J.P. and M. Smialowski, *Hydrogen Degradation of Ferrous Alloys*. William Andrew Publishing/Noyes. p. 52-77.
3.  Züttel, A., *Materials for hydrogen storage*. Materials Today, 2003. **6**(9): p. 24-33.
4.  *Phase Diagrams and Statistical Thermodynamics of Binary M-H Systems*, in *The Metal-Hydrogen System: Basic Bulk Properties*, Y. Fukai, Editor. 2005, Springer Berlin Heidelberg: Berlin, Heidelberg. p. 9-53.
5.  He, Y., et al., *Diffusion coefficient of hydrogen interstitial atom in alpha-Fe, gamma-Fe and epsilon-Fe crystals by first-principle calculations*. International Journal of Hydrogen Energy, 2017. **42**(44): p. 27438-27445.
6.  DosSantos, D.S. and P.E.V. DeMiranda, *Hydrogen diffusivity and solubility in crystalline and amorphous alloys*. Journal of Materials Science, 1997. **32**(23): p. 6311-6315.
7.  Kirchheim, R. and A. Pundt, *25 - Hydrogen in Metals A2 - Laughlin, David E*, in *Physical Metallurgy (Fifth Edition)*, K. Hono, Editor. 2014, Elsevier: Oxford. p. 2597-2705.
8.  Mutschele, T. and R. Kirchheim, *Segregation and Diffusion of Hydrogen in Grain-Boundaries of Palladium*. Scripta Metallurgica, 1987. **21**(2): p. 135-140.
9.  Arantes, D.R., et al., *Hydrogen Diffusion and Permeation in Microcrystalline and Nanocrystalline Nickel*. Acta Metallurgica Et Materialia, 1993. **41**(11): p. 3215-3222.
10. Oudriss, A., et al., *Grain size and grain-boundary effects on diffusion and trapping of hydrogen in pure nickel*. Acta Materialia, 2012. **60**(19): p. 6814-6828.
11. Cao, L. and G.Y. Zhou, *Intergranular fracture of low-alloy cast steel*. Materials Characterization, 1996. **36**(2): p. 65-72.
12. Lu, G.H., et al., *Origin of intergranular embrittlement of Al alloys induced by Na and Ca segregation: Grain boundary weakening*. Physical Review B, 2006. **73**(22).
13. Wert, J.A. and J.B. Lumsden, *Intergranular Fracture in an Al-Li-Cu-Mg-Zr Alloy*. Scripta Metallurgica, 1985. **19**(2): p. 205-209.
14. Ebrahimi, F., et al., *Fracture of bulk face centered cubic (FCC) metallic nanostructures*. Reviews on Advanced Materials Science, 2006. **13**(1): p. 33-40.
15. Zhu, X.K. and J.A. Joyce, *Review of fracture toughness (G, K, J, CTOD, CTOA) testing and standardization*. Engineering Fracture Mechanics, 2012. **85**: p. 1-46.
16. Gao, H.J. and Y.G. Huang, *Geometrically necessary dislocation and size-dependent plasticity*. Scripta Materialia, 2003. **48**(2): p. 113-118.
17. Motz, C., T. Schoberl, and R. Pippan, *Mechanical properties of micro-sized copper bending beams machined by the focused ion beam technique*. Acta Materialia, 2005. **53**(15): p. 4269-4279.
18. Demir, E., D. Raabe, and F. Roters, *The mechanical size effect as a mean-field breakdown phenomenon: Example of microscale single crystal beam bending*. Acta Materialia, 2010. **58**(5): p. 1876-1886.
19. Lynch, S., *Hydrogen embrittlement phenomena and mechanisms*. Corrosion Reviews, 2012. **30**(3-4): p. 105-123.
20. McMahon, C.J., *Hydrogen-induced intergranular fracture of steels*. Engineering Fracture Mechanics, 2001. **68**(6): p. 773-788.
21. Huang, H.Y. and M. Wu, *First principles calculations of hydrogen-induced decrease in the cohesive strength of alpha-Al2O3 single crystals*. Computational Materials Science, 2012. **54**: p. 81-83.

22. Vehoff, H. and W. Rothe, *Overview .30. Gaseous-Hydrogen Embrittlement in Fesi-Single and Ni-Single Crystals.* Acta Metallurgica, 1983. **31**(11): p. 1781-1793.

23. Martin, M.L., I.M. Robertson, and P. Sofronis, *Interpreting hydrogen-induced fracture surfaces in terms of deformation processes: A new approach.* Acta Materialia, 2011. **59**(9): p. 3680-3687.

24. Beachem, C.D., *New Model for Hydrogen-Assisted Cracking (Hydrogen Embrittlement).* Metallurgical Transactions, 1972. **3**(2): p. 437-+.

25. Barrera, O., et al., *Modelling the coupling between hydrogen diffusion and the mechanical behaviour of metals.* Computational Materials Science, 2016. **122**: p. 219-228.

26. Depover, T. and K. Verbeken, *The detrimental effect of hydrogen at dislocations on the hydrogen embrittlement susceptibility of Fe-C-X alloys: An experimental proof of the HELP mechanism.* International Journal of Hydrogen Energy, 2018. **43**(5): p. 3050-3061.

27. Robertson, I.M. and H.K. Birnbaum, *An Hvem Study of Hydrogen Effects on the Deformation and Fracture of Nickel.* Acta Metallurgica, 1986. **34**(3): p. 353-366.

28. Birnbaum, H.K. and P. Sofronis, *Hydrogen-Enhanced Localized Plasticity - a Mechanism for Hydrogen-Related Fracture.* Materials Science and Engineering a-Structural Materials Properties Microstructure and Processing, 1994. **176**(1-2): p. 191-202.

29. Ferreira, P.J., I.M. Robertson, and H.K. Birnbaum, *Hydrogen effects on the interaction between dislocations.* Acta Materialia, 1998. **46**(5): p. 1749-1757.

30. Song, J. and W.A. Curtin, *Mechanisms of hydrogen-enhanced localized plasticity: An atomistic study using alpha-Fe as a model system.* Acta Materialia, 2014. **68**: p. 61-69.

31. Novak, P., et al., *A statistical, physical-based, micro-mechanical model of hydrogen-induced intergranular fracture in steel.* Journal of the Mechanics and Physics of Solids, 2010. **58**(2): p. 206-226.

32. Djukic, M.B., et al., *Hydrogen embrittlement of low carbon structural steel.* 20th European Conference on Fracture, 2014. **3**: p. 1167-1172.

33. Djukic, M.B., et al., *Towards a unified and practical industrial model for prediction of hydrogen embrittlement and damage in steels.* 21st European Conference on Fracture, (Ecf21), 2016. **2**: p. 604-611.

34. Fukai, Y., *Superabundant vacancies formed in metal-hydrogen alloys.* Physica Scripta, 2003. **T103**: p. 11-14.

35. Xie, D.G., et al., *Hydrogenated vacancies lock dislocations in aluminium.* Nature Communications, 2016. **7**.

36. Lynch, S.P., *Environmentally Assisted Cracking - Overview of Evidence for an Adsorption-Induced Localized-Slip Process.* Acta Metallurgica, 1988. **36**(10): p. 2639-2661.

37. Kirchheim, R., *Revisiting hydrogen embrittlement models and hydrogen-induced homogeneous nucleation of dislocations.* Scripta Materialia, 2010. **62**(2): p. 67-70.

38. Lynch, S.P., *Mechanisms and Kinetics of Environmentally Assisted Cracking: Current Status, Issues, and Suggestions for Further Work.* Metallurgical and Materials Transactions a-Physical Metallurgy and Materials Science, 2013. **44A**(3): p. 1209-1229.

39. Volkert, C.A. and A.M. Minor, *Focused ion beam microscopy and micromachining.* Mrs Bulletin, 2007. **32**(5): p. 389-395.

40. Yao, N., *Introduction to the focused ion beam system*, in *Focused Ion Beam Systems: Basics and Applications*, N. Yao, Editor. 2007, Cambridge University Press: Cambridge. p. 1-30.

41.     Bhavsar, S.N., S. Aravindan, and P.V. Rao, *Machinability Study of Cemented Carbide Using Focused Ion Beam (FIB) Milling.* Materials and Manufacturing Processes, 2012. **27**(10): p. 1029-1034.

42.     Armstrong, D.E.J., et al., *Small-scale characterisation of irradiated nuclear materials: Part II nanoindentation and micro-cantilever testing of ion irradiated nuclear materials.* Journal of Nuclear Materials, 2015. **462**: p. 374-381.

43.     Chan, H., S.G. Roberts, and J. Gong, *Micro-scale fracture experiments on zirconium hydrides and phase boundaries.* Journal of Nuclear Materials, 2016. **475**: p. 105-112.

44.     Hajilou, T., et al., *In situ electrochemical microcantilever bending test: A new insight into hydrogen enhanced cracking.* Scripta Materialia, 2017. **132**: p. 17-21.

45.     Kupfer, B.Z., et al., *Fabrication and characterisation of triangle-faced single crystal diamond micro-cantilevers.* Diamond and Related Materials, 2010. **19**(7-9): p. 742-747.

46.     Zhao, X., et al., *Mechanical properties of SiC coatings on spherical particles measured using the micro-beam method.* Scripta Materialia, 2008. **59**(1): p. 39-42.

47.     Darnbrough, J.E., D. Liu, and P.E.J. Flewitt, *Micro-scale testing of ductile and brittle cantilever beam specimens in situ with a dual beam workstation.* Measurement Science and Technology, 2013. **24**(5).

48.     Liu, L., et al., *Micro-mechanical and fracture characteristics of Cu6Sn5 and Cu3Sn intermetallic compounds under micro-cantilever bending.* Intermetallics, 2016. **76**: p. 10-17.

49.     Massl, S., et al., *Investigation of fracture properties of magnetron-sputtered TiN films by means of a FIB-based cantilever bending technique.* Acta Materialia, 2009. **57**(6): p. 1768-1776.

50.     McCarthy, J., et al., *FIB micromachined submicron thickness cantilevers for the study of thin film properties.* Thin Solid Films, 2000. **358**(1-2): p. 146-151.

51.     Takashima, K., et al., *Fatigue crack growth behavior of micro-sized specimens prepared from an electroless plated Ni-P amorphous alloy thin film.* Materials Transactions Jim, 2001. **42**(1): p. 68-73.

52.     Wurster, S., C. Motz, and R. Pippan, *Characterization of the fracture toughness of micro-sized tungsten single crystal notched specimens.* Philosophical Magazine, 2012. **92**(14): p. 1803-1825.

53.     Schwarzer, R.A., et al., *Present State of Electron Backscatter Diffraction and Prospective Developments*, in *Electron Backscatter Diffraction in Materials Science*, A.J. Schwartz, et al., Editors. 2009, Springer US: Boston, MA. p. 1-20.

54.     Iqbal, F., et al., *In situ micro-cantilever tests to study fracture properties of NiAl single crystals.* Acta Materialia, 2012. **60**(3): p. 1193-1200.

55.     Tarzimoghadam, Z., et al., *Hydrogen-assisted failure in Ni-based superalloy 718 studied under in situ hydrogen charging: The role of localized deformation in crack propagation.* Acta Materialia, 2017. **128**: p. 365-374.

56.     Hajilou, T., et al., *Hydrogen enhanced cracking studies on Fe-3wt%Si single and bi-crystal microcantilevers.* Philosophical Transactions of the Royal Society a-Mathematical Physical and Engineering Sciences, 2017. **375**(2098).

57.     Lee, T.C., I.M. Robertson, and H.K. Birnbaum, *An Hvem Insitu Deformation Study of Nickel Doped with Sulfur.* Acta Metallurgica, 1989. **37**(2): p. 407-415.

58.     Yamaguchi, M., M. Shiga, and H. Kaburaki, *Grain boundary decohesion by impurity segregation in a nickel-sulfur system.* Science, 2005. **307**(5708): p. 393-397.

59.     Wang, S., et al., *Hydrogen-induced intergranular failure of iron.* Acta Materialia, 2014. **69**: p. 275-282.

60. Bruemmer, S.M., et al., *Influence of Sulfur, Phosphorus, and Antimony Segregation on the Intergranular Hydrogen Embrittlement of Nickel.* Metallurgical Transactions a-Physical Metallurgy and Materials Science, 1983. **14**(2): p. 223-232.

61. Jones, R.H., et al., *Hydrogen Pressure-Dependence of the Fracture Mode Transition in Nickel.* Metallurgical Transactions a-Physical Metallurgy and Materials Science, 1983. **14**(8): p. 1729-1736.

62. Robertson, I.M. and H.K. Birnbaum, *Effect of Hydrogen on the Dislocation-Structure of Deformed Nickel.* Scripta Metallurgica, 1984. **18**(3): p. 269-274.

63. Tehranchi, A. and W.A. Curtin, *Atomistic study of hydrogen embrittlement of grain boundaries in nickel: I. Fracture.* Journal of the Mechanics and Physics of Solids, 2017. **101**: p. 150-165.

64. Tahir, A.M., R. Janisch, and A. Hartmaier, *Hydrogen embrittlement of a carbon segregated Sigma 5(310)[001] symmetrical tilt grain boundary in alpha-Fe.* Materials Science and Engineering a-Structural Materials Properties Microstructure and Processing, 2014. **612**: p. 462-467.

65. Xiao, L., D.L. Chen, and M.C. Chaturvedi, *Shearing of gamma '' precipitates and formation of planar slip bands in Inconel 718 during cyclic deformation.* Scripta Materialia, 2005. **52**(7): p. 603-607.

66. W T Becker and S Lampman. "Fracture Appearance and Mechanisms of Deformation and Fracture". [Online]. http://jpkc.fudan.edu.cn/picture/article/348/1b/ee/6dce0ae740cf8673b53e4e96abb8/6ad0c8ee-53c3-4790-a931-211df202df69.pdf

67. W D Callister Jr., *"Material Science and Engineering" chapter 9*, 2nd ed. USA: John Wiley & Sons, Inc, 2005.

68. T L Anderson, *"Fracture Mechanics - Fundamentals and applications" page 61-64*, 3rd ed.: Taylor and Francis Group, LLC, 2005.

69. *C.* Thaulow, "Brittle to ductile Transition" Lecture notes TMM4162, Atomistic and Multiscale Material Modeling and Testing, NTNU. 2014

70. "Electrochemical double layer." *Electrochemical Nanoscience Lab,* Universität Bern, 07.12.2007. [Online]. http://wandlowski.dcb.unibe.ch/research/edl.html].

71. Merrill, J.M. and R.C. Wilcox, *Determination of cleavage planes and fracture characterization of Ni-based single crystal superalloys.* NASA, 1992. p. 1-25.

# Appendices

=

# Appendix A: Risk assessment

**NTNU**

| | Utarbeidet av | Nummer | Dato |
|---|---|---|---|
| | HMS-avd. | HMSRV2601 | 22.03.2011 |
| HMS | Godkjent av | | Erstatter |
| | Rektor | | 01.12.2006 |

## Kartlegging av risikofylt aktivitet

**Dato: 26.09.17**

**Enhet: IPM**

**Linjeleder:**

**Deltakere ved kartleggingen (m/ funksjon): Sondre Fossheim (Student), Afrooz Barnoush (Supervisor).**
*(Ansv. veileder, student, evt. medveiledere, evt. andre m. kompetanse)*

**Kort beskrivelse av hovedaktivitet/hovedprosess: Milling of micro-sized cantilevers with a FIB microscope at the NTNU nanolab**

**Er oppgaven rent teoretisk? (JA/NEI): NEI**   *«JA» betyr at veileder innestår for at oppgaven ikke inneholder noen aktiviteter som krever risikovurdering. Dersom «JA»: Beskriv kort aktiviteten i kartleggingskjemaet under. Risikovurdering trenger ikke å fylles ut.*

**Signaturer:**   *Ansvarlig veileder:*   **Student:** *Sondre Fossheim*

| ID nr. | Aktivitet/prosess | Ansvarlig | Eksisterende dokumentasjon | Eksisterende sikringstiltak | Lov, forskrift o.l. | Kommentar |
|---|---|---|---|---|---|---|
| 01 | Working in cleanroom | Sondre Fossheim | Cleanroom course, Trygg handtering av nanomaterialer (Arbeidstilsynet) | Alarms and evacuation procedures for dangerous levels of toxic gases or similar hazards. Need training and courses to enter lab and chemical areas. Buddy rule (follower). Recordings of exposure to nanoparticles. | Arbeidsmiljoloven, §3-1, §4-1, §4-5, §5-4, Internkontrollforskriften, §5, Arbeidsmiljøforskriftene, §1-4, §3-1, §2-1, CLP og merkeforskriften, REACH, Forskrift om gjenvinning og behandling av avfall kap. 11-farlig avfall | |
| 02 | Milling of bicrystal cantilevers in specimens using Focused Ion Beam (FIB) | Sondre Fossheim | Instrument course, manual (on site), risk assessment (on site), protocol for general usage (on site) | Follow protocol for usage printed on A4-paper on site, users are not allowed to remove covers from the instrument or parts of it, maintenance and repair is done by trained engineers only, the instrument will be disconnected from power and the person who will do the work have to wait some minutes prior work that requires the removal of covers, users do not have access source, chamber door only allowed to be opened for brief moments for exchange of sample, warning labels for hazardous parts of the equipment | Law regarding service at and work with electrical constructions and equipment, law regarding ionizing radiation (strålevernloven) | |

| NTNU | | Utarbeidet av | Nummer | Dato |
|---|---|---|---|---|
| ⬛ | **Risikovurdering** | HMS-avd. | HMSRV2601 | 22.03.2011 |
| HMS | | Godkjent av | | Erstatter |
| | | Rektor | | 01.12.2006 |

**Enhet: IPM**

**Linjeleder:**

**Dato: 26.09.2017**

**Deltakere ved kartleggingen (m/ funksjon): Sondre Fossheim (Student), Afrooz Barnoush (Supervisor)**
*(Ansv. Veileder, student, evt. medveiledere, evt. andre m. kompetanse)*

**Risikovurderingen gjelder hovedaktivitet:** A03-01, 755896, Advanced nano-scale characterization of hydrogen embrittlement

**Signaturer:** Ansvarlig veileder: _(signature)_   Student: _Sondre Fossheim (signature)_

| ID nr | Aktivitet fra kartleggings-skjemaet | Mulig uønsket hendelse/ belastning | Vurdering av sannsyn-lighet (1-5) | Vurdering av konsekvens: | | | | Risiko-Verdi (menn-eske) | Kommentarer/status Forslag til tiltak |
|---|---|---|---|---|---|---|---|---|---|
| | | | | Menneske (A-E) | Ytre miljø (A-E) | Øk/ materiell (A-E) | Om-dømme (A-E) | | |
| 01 | Working in cleanroom | Discharge/spill of toxic chemicals (HF, PDMS or other toxic substances) | 2 | C | A | B | B | C2 | Chemical spill is mainly a concern for those working in the chemical lab. sections, as the evacuation alarm will initiate when dangerous levels of a gas is detected in this area |
| 01 | Working in cleanroom | Spread of nanoparticles | 2 | B | A | B | B | B2 | The effect of nanoparticles on humans are uncertain. Can cause inflammation or sickness |
| 02 | Milling of bicrystal cantilevers in specimens using Focused Ion Beam (FIB) | Potential dangerous voltages | 1 | E | - | - | C | E1 | Potentially dangerous electrical currents might be present while power is connected. Capacitators might keep high voltage for some minutes after the power is unplugged |
| 02 | Milling of bicrystal cantilevers in specimens using Focused Ion Beam (FIB) | UV/IR and X-ray hazard | 1 | A | - | - | B | A1 | An optical light source for illuminating the process is contained in the chamber. The light source is a UV/IR hazard. The X-ray limit is 1 µS/h at 10 cm distance from the surface |
| 02 | Milling of bicrystal cantilevers in specimens using Focused Ion Beam (FIB) | Failure of cardiac pacemaker | 1 | E | - | - | B | E1 | System uses strong magnets on the ion column. A hazard occurs when using magnetizable prosthesis and other metal objects within 5 cm of the cold cathode gauge. A permanent magnet causes the effect, meaning it is affective even if the equipment is not powered. There is however no need for users to go near the ion pump |

NTNU
HMS

Risikovurdering

| | Utarbeidet av | Nummer | Dato |
|---|---|---|---|
| | HMS-avd. | HMSRV2601 | 22.03.2011 |
| | Godkjent av | | Erstatter |
| | Rektor | | 01.12.2006 |

## Sannsynlighet vurderes etter følgende kriterier:

| Svært liten 1 | Liten 2 | Middels 3 | Stor 4 | Svært stor 5 |
|---|---|---|---|---|
| 1 gang pr 50 år eller sjeldnere | 1 gang pr 10 år eller sjeldnere | 1 gang pr år eller sjeldnere | 1 gang pr måned eller sjeldnere | Skjer ukentlig |

## Konsekvens vurderes etter følgende kriterier:

| Gradering | Menneske | Ytre miljø Vann, jord og luft | Øk/materiell | Omdømme |
|---|---|---|---|---|
| E Svært Alvorlig | Død | Svært langvarig og ikke reversibel skade | Drifts- eller aktivitetsstans >1 år. | Troverdighet og respekt betydelig og varig svekket |
| D Alvorlig | Alvorlig personskade. Mulig uførhet. | Langvarig skade. Lang restitusjonstid | Driftsstans > ½ år Aktivitetsstans i opp til 1 år | Troverdighet og respekt betydelig svekket |
| C Moderat | Alvorlig personskade. | Mindre skade og lang restitusjonstid | Drifts- eller aktivitetsstans < 1 mnd | Troverdighet og respekt svekket |
| B Liten | Skade som krever medisinsk behandling | Mindre skade og kort restitusjonstid | Drifts- eller aktivitetsstans < 1uke | Negativ påvirkning på troverdighet og respekt |
| A Svært liten | Skade som krever førstehjelp | Ubetydelig skade og kort restitusjonstid | Drifts- eller aktivitetsstans < 1dag | Liten påvirkning på troverdighet og respekt |

## Risikoverdi = Sannsynlighet x Konsekvens

Beregn risikoverdi for Menneske. Enheten vurderer selv om de i tillegg vil beregne risikoverdi for Ytre miljø, Økonomi/materiell og Omdømme. I så fall beregnes disse hver for seg.

## Til kolonnen "Kommentarer/status, forslag til forebyggende og korrigerende tiltak":

Tiltak kan påvirke både sannsynlighet og konsekvens. Prioriter tiltak som kan forhindre at hendelsen inntreffer, dvs. sannsynlighetsreduserende tiltak foran skjerpet beredskap, dvs. konsekvensreduserende tiltak.

# MATRISE FOR RISIKOVURDERINGER ved NTNU

| | Svært liten | Liten | Middels | Stor | Svært stor |
|---|---|---|---|---|---|
| **Svært alvorlig** | E1 | E2 | E3 | E4 | E5 |
| **Alvorlig** | D1 | D2 | D3 | D4 | D5 |
| **Moderat** | C1 | C2 | C3 | C4 | C5 |
| **Liten** | B1 | B2 | B3 | B4 | B5 |
| **Svært liten** | A1 | A2 | A3 | A4 | A5 |
| | | | **SANNSYNLIGHET** | | |

**Prinsipp over akseptkriterium. Forklaring av fargene som er brukt i risikomatrisen.**

| Farge | | Beskrivelse |
|---|---|---|
| Rød | | Uakseptabel risiko. Tiltak skal gjennomføres for å redusere risikoen. |
| Gul | | Vurderingsområde. Tiltak skal vurderes. |
| Grønn | | Akseptabel risiko. Tiltak kan vurderes ut fra andre hensyn. |

# Appendix B: EBSD maps and selected milling sites

In this section, the EBSD maps and selected milling sites for each sample that was treated in this work is presented. The selected milling sites are marked with a circle and it is also indicated whether the cantilevers were milled to include a GB (BC) or was milled within a grain (SC). The EBSD map for pure Ni spans over the whole sample surface due the large average grain size.



**Ni718 Solution annealed (SC)**

**Pure Ni (BC)**

**NiS (BC)**
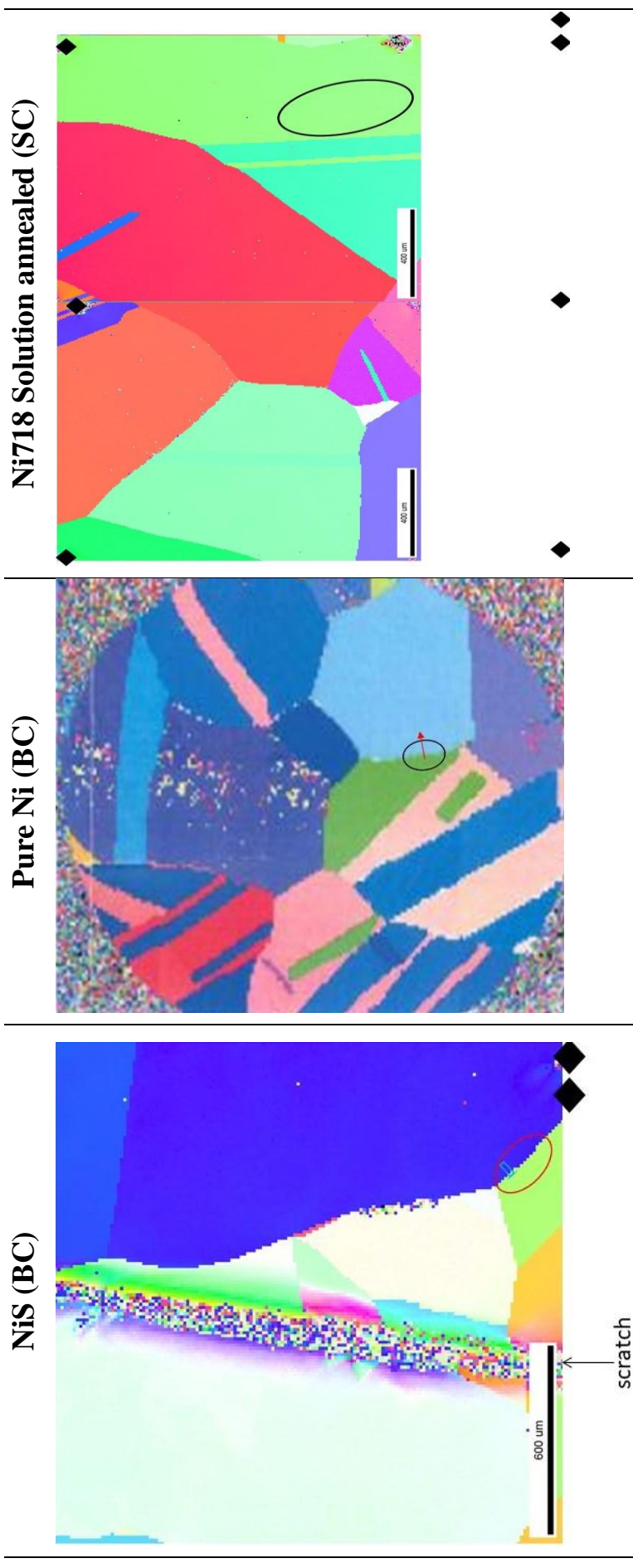
**Ni725 Solution annealed 2 (BC)**

500 um
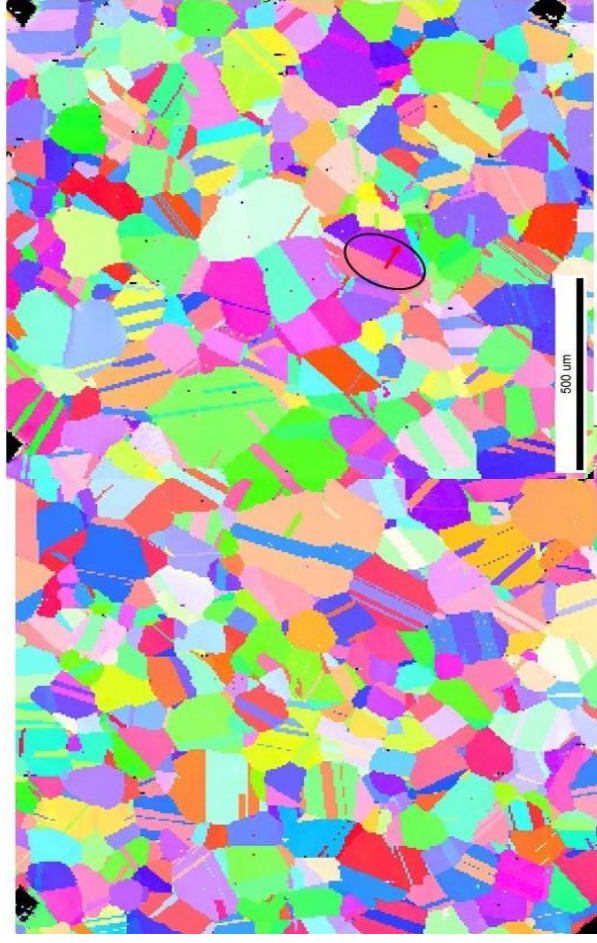
**Ni725 Solution annealed 1 (SC)**

300 um
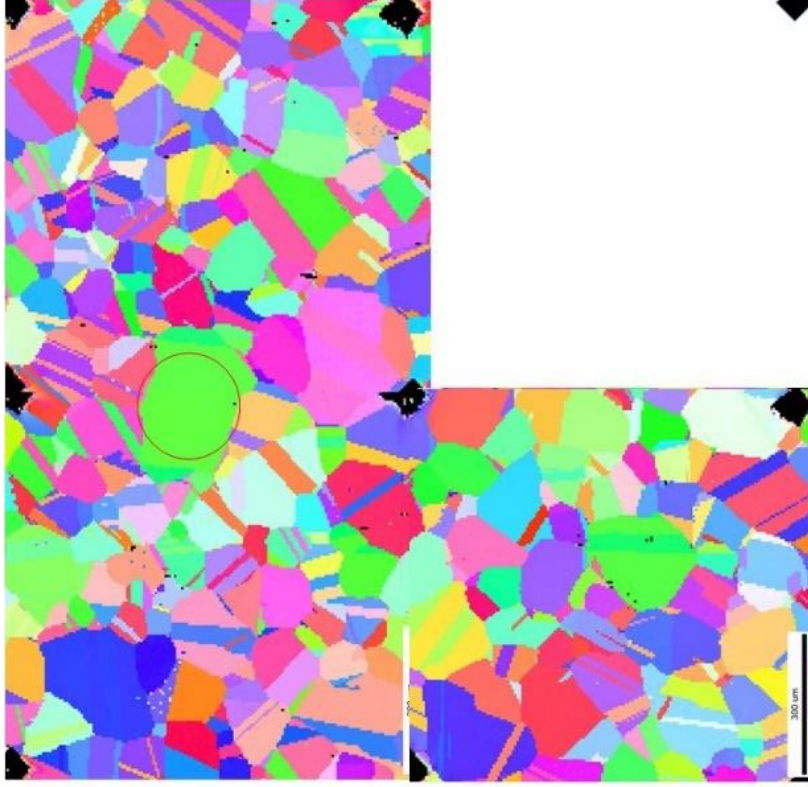
**Ni725 Over aged (SC)**



**Ni725 Participation hardened (SC)**
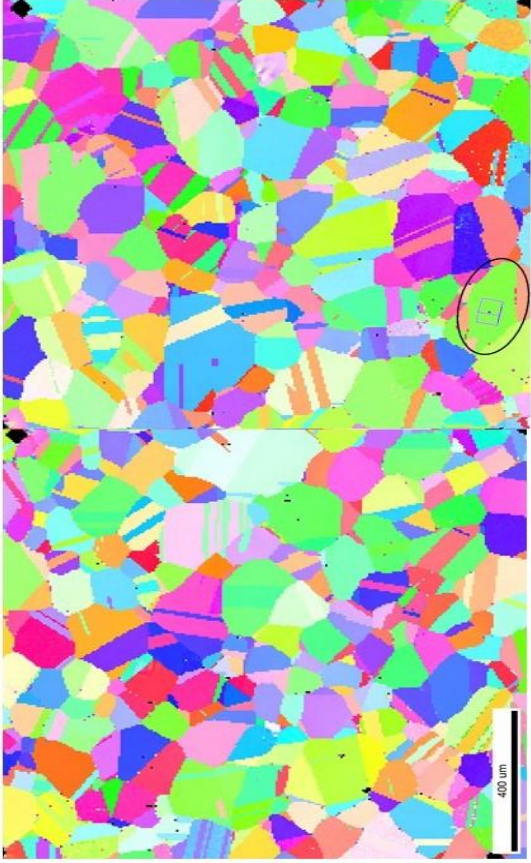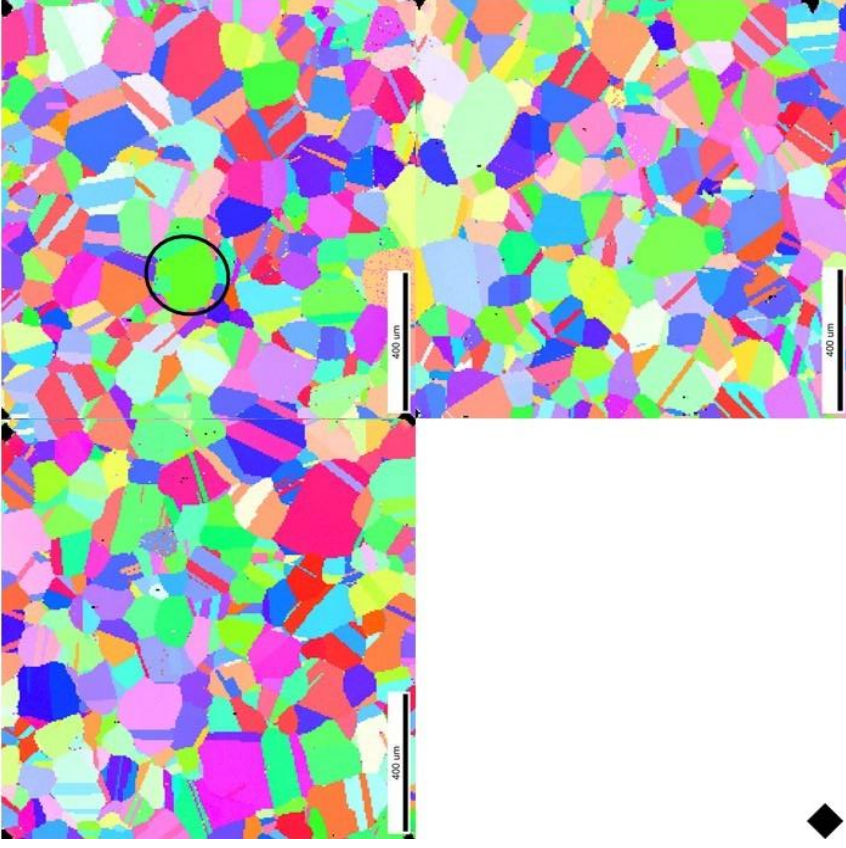
# Appendix C: Cantilever images before and after bending

The images presented here are only for the cantilevers that were tested.

## NiS

Cantilever 3: Before bending
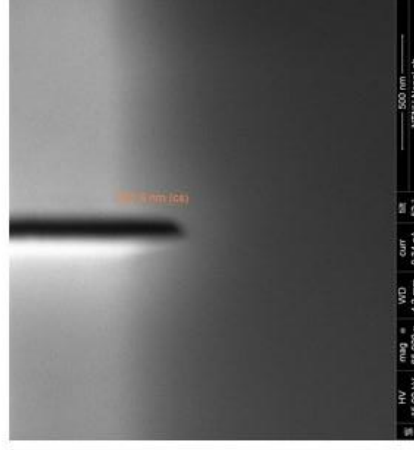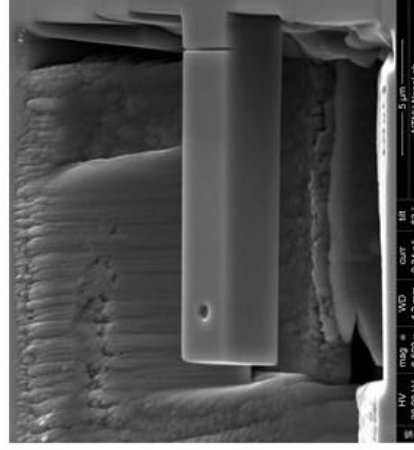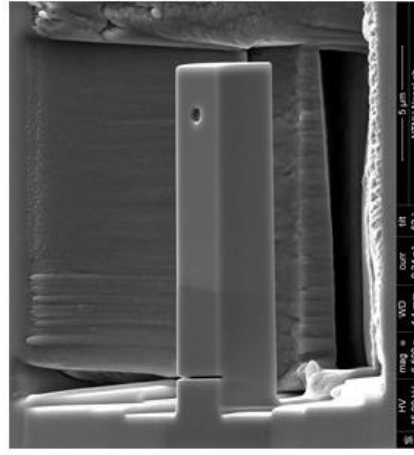


Cantilever 3: After bending (In air, 17 hours after H charge)
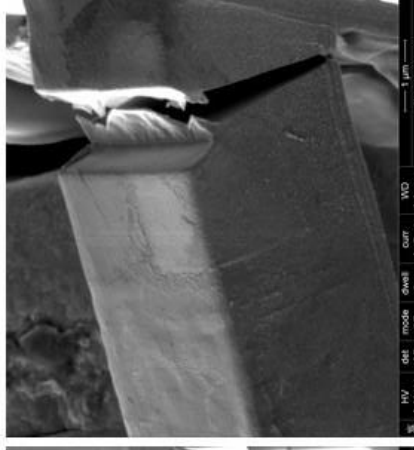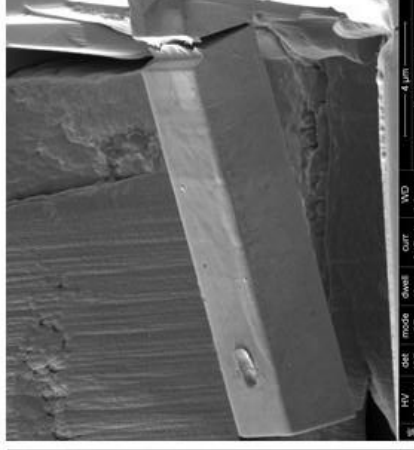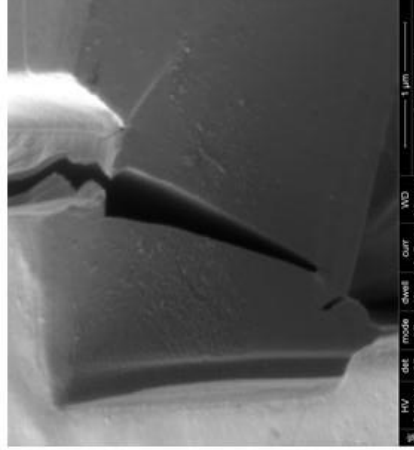
Cantilever 4: Before bending



Cantilever 4: After bending (In-situ, 2 hours of H charging)

Cantilever 5: Before bending
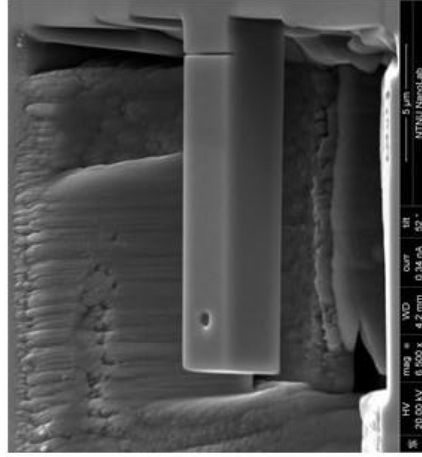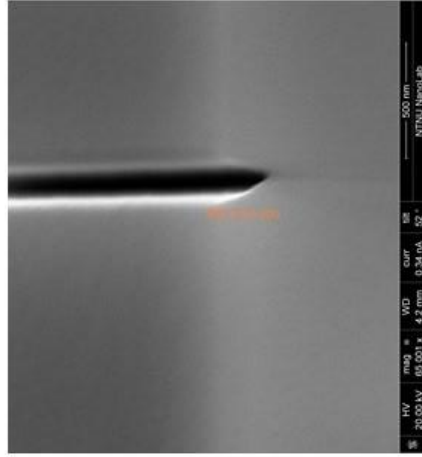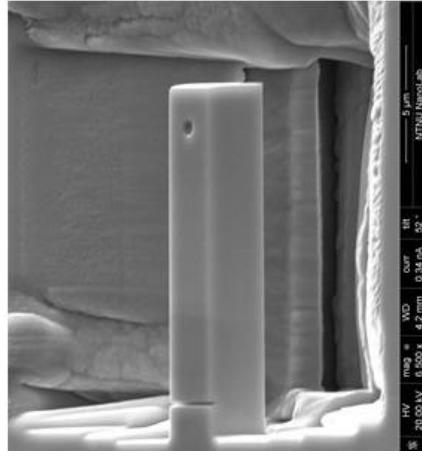
Cantilever 5: After bending (In-situ, 3 hours of H charging)
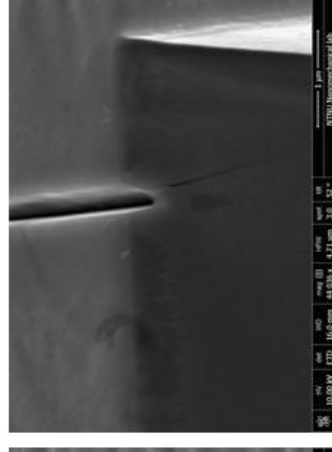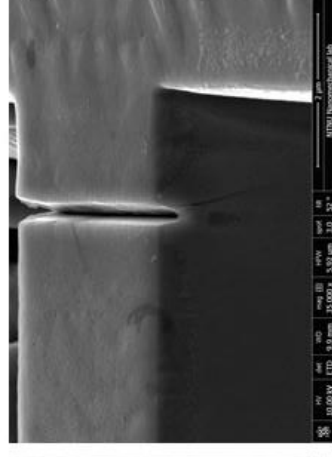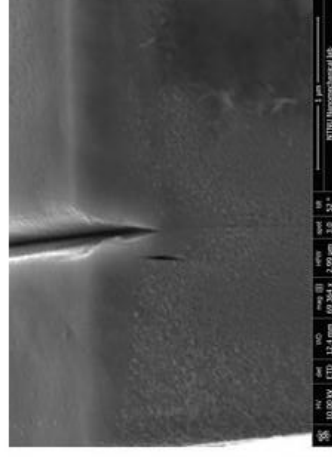
Cantilever 6: Before bending
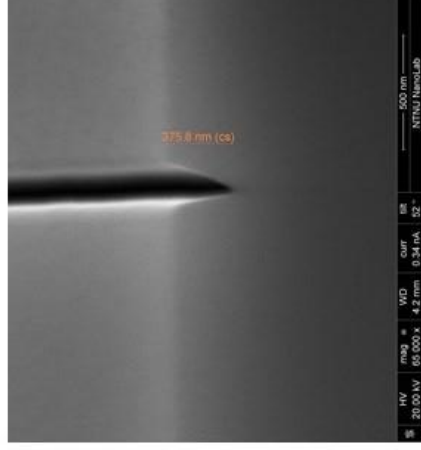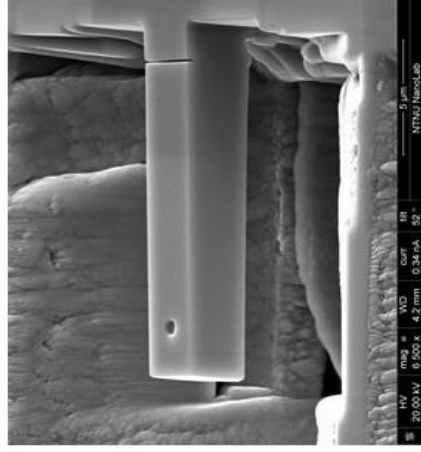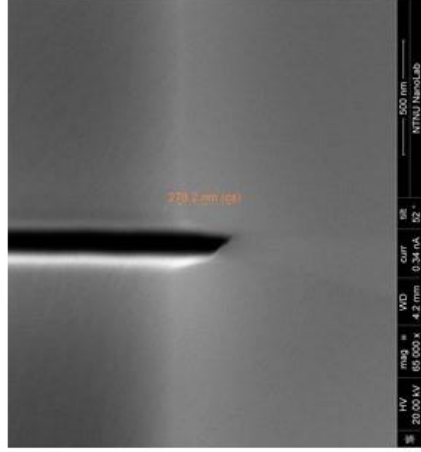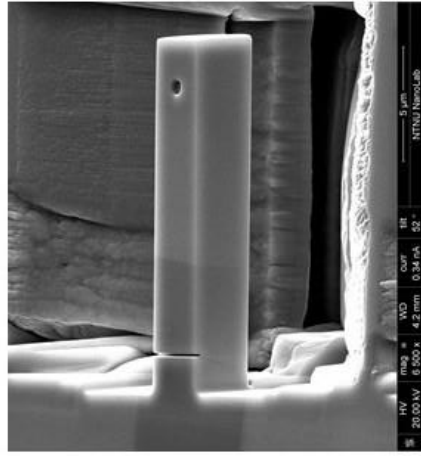
Cantilever 6: After bending (In air, 2 hours after H charge, 4,5nm/s)
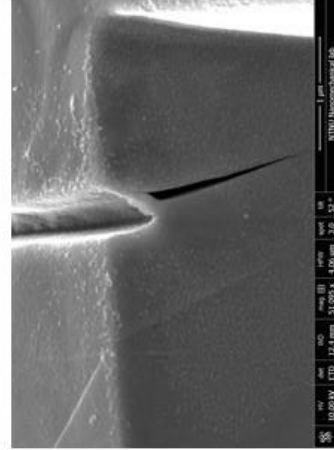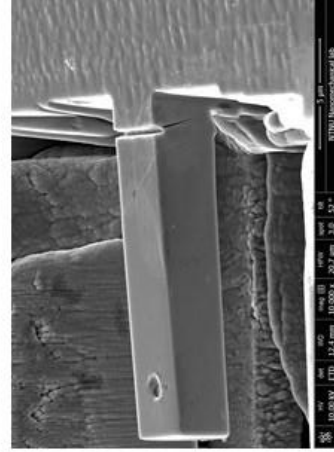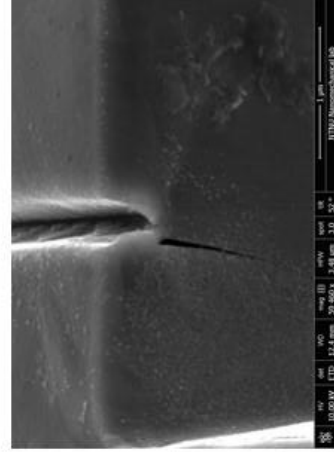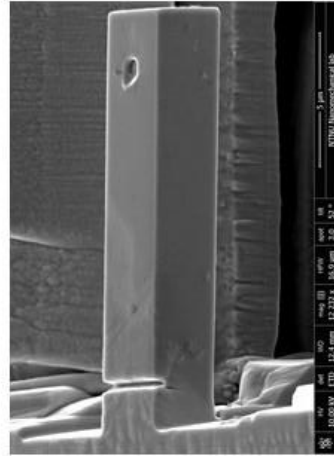
Cantilever 7: Before bending
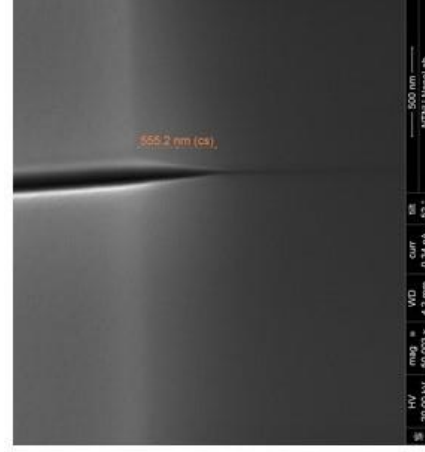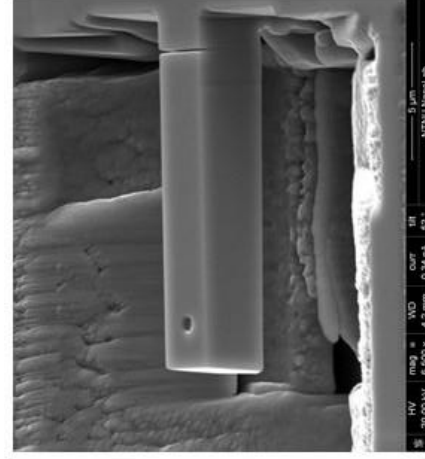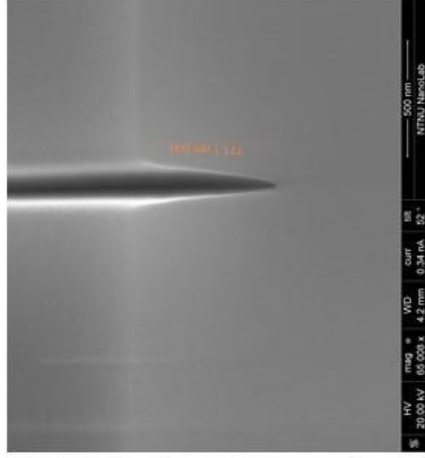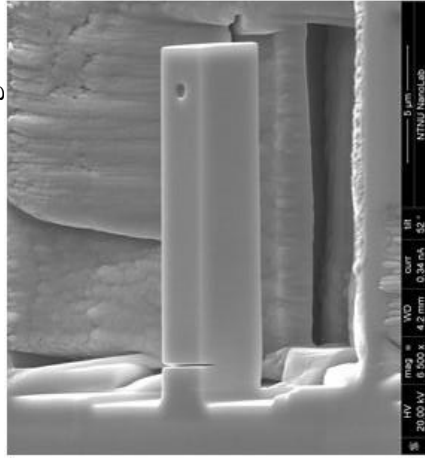
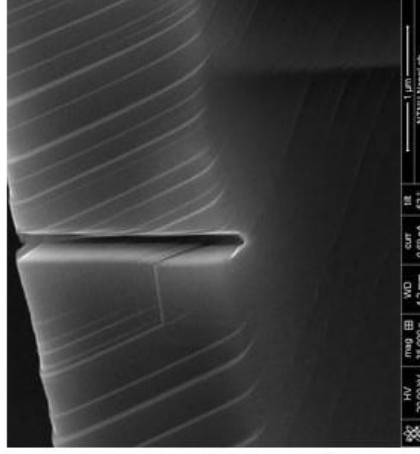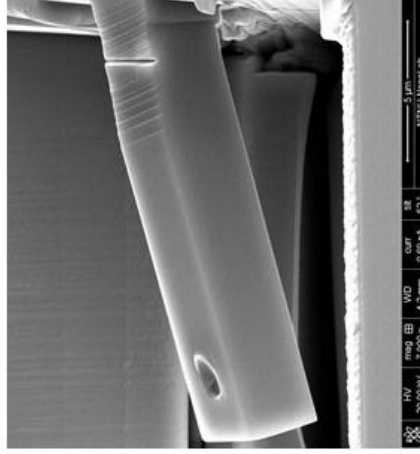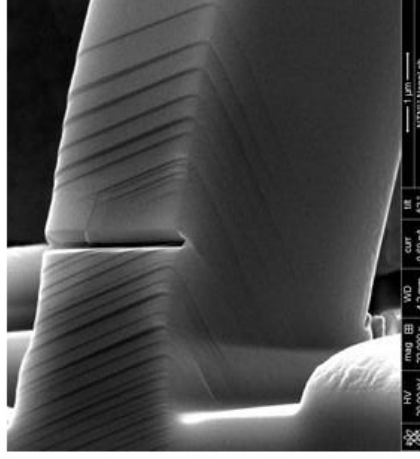Cantilever 7: After bending (In air, 2 hours after H charge)
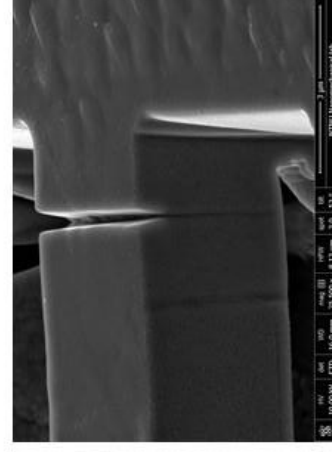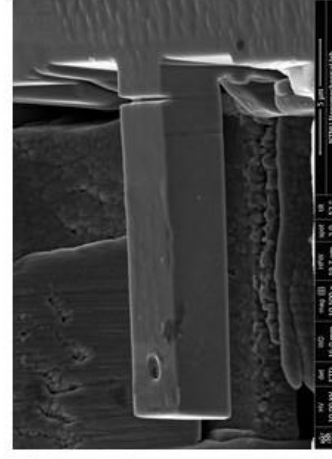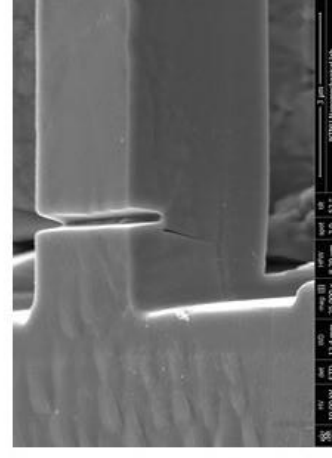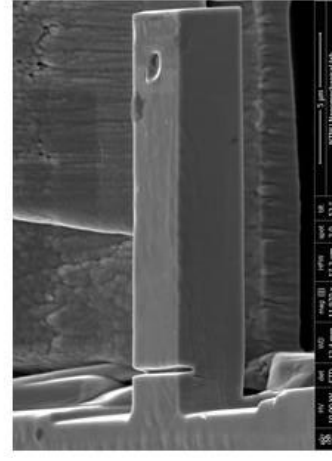
Cantilever 8: Before bending
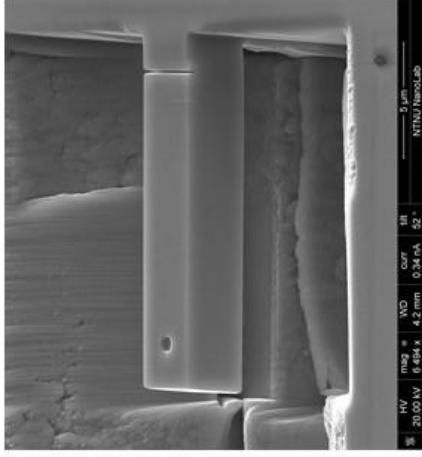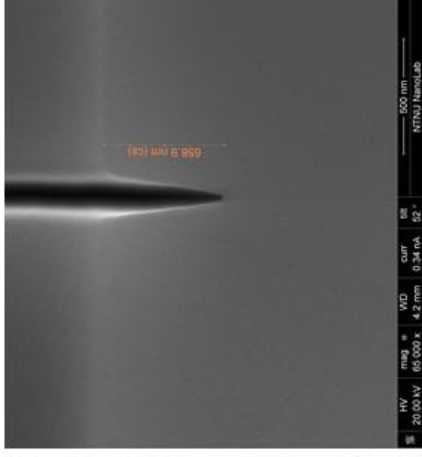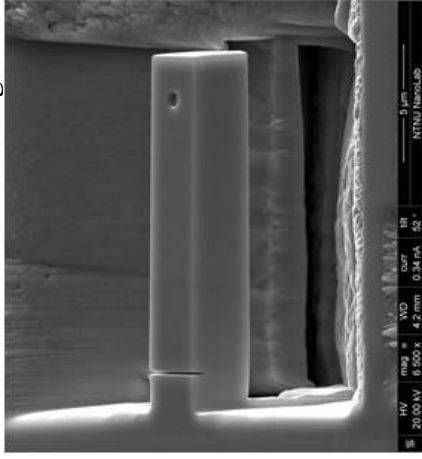
Cantilever 8: After bending (Air)
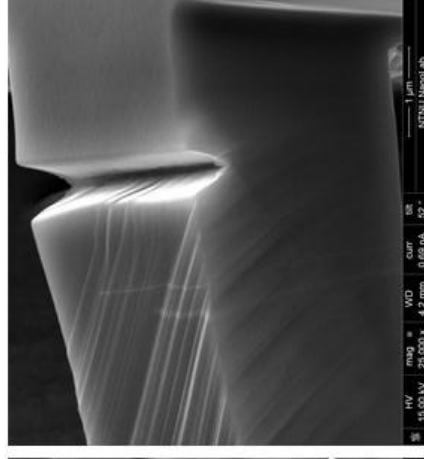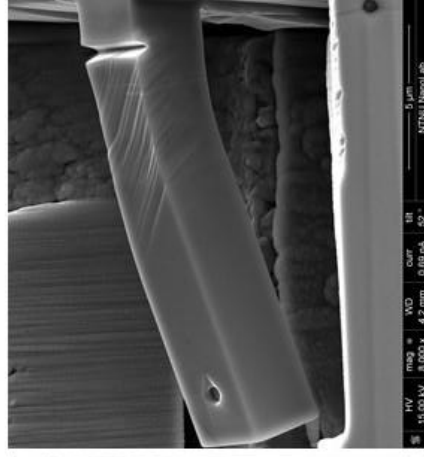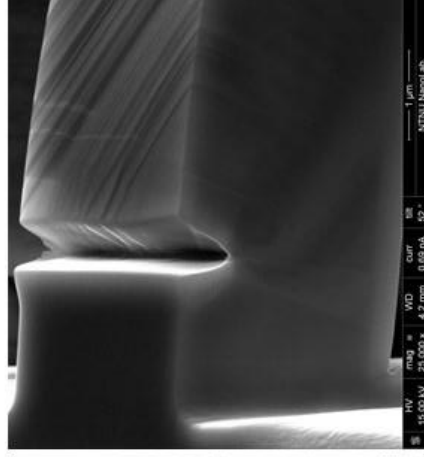
Cantilever 9: Before bending
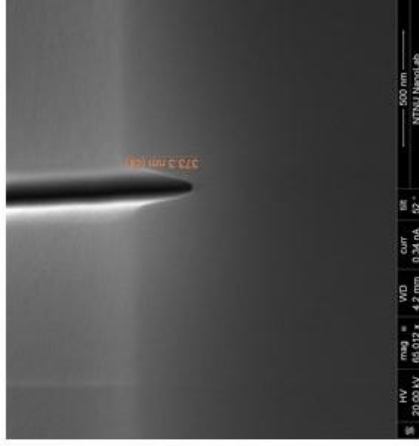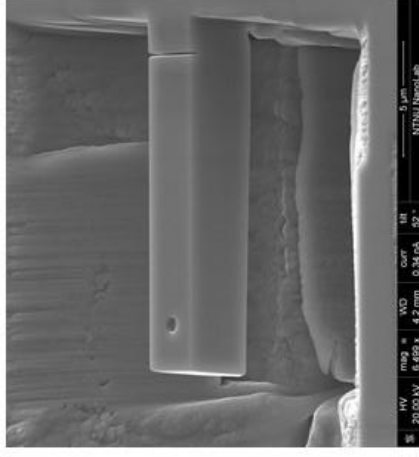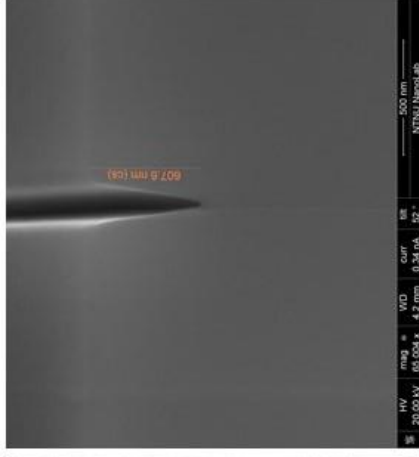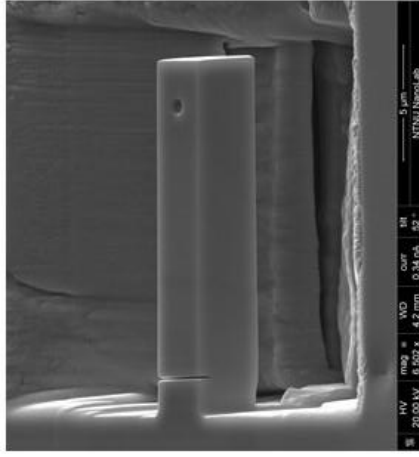


Cantilever 9: After bending (Air)
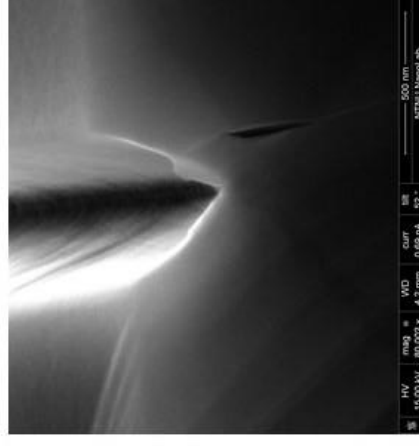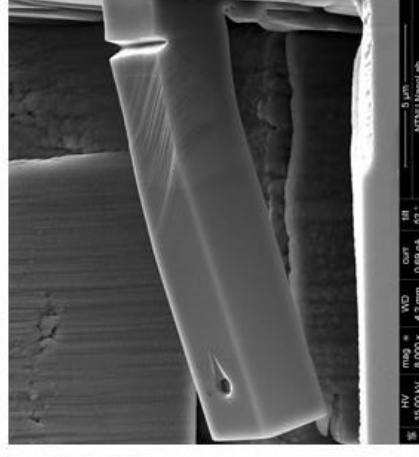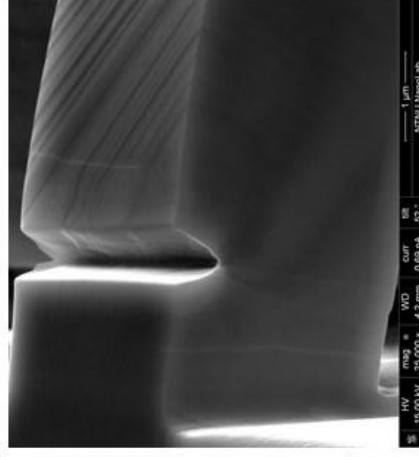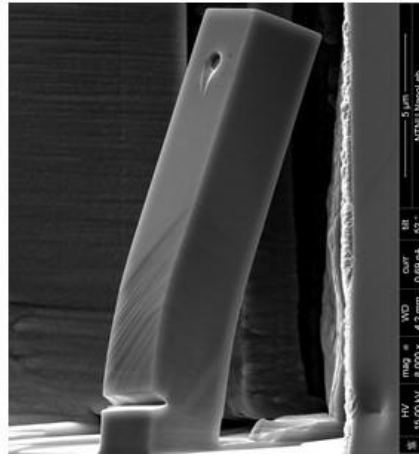
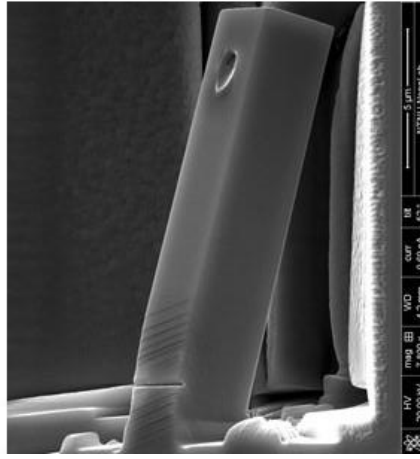Cantilever 10: Before bending
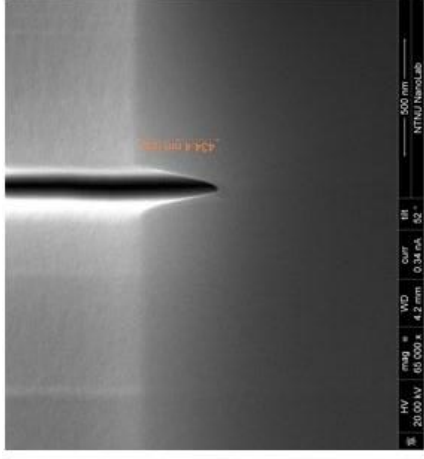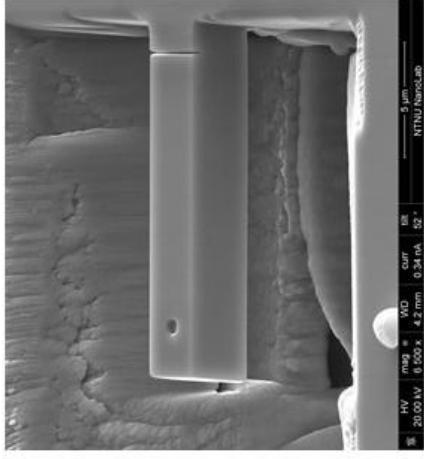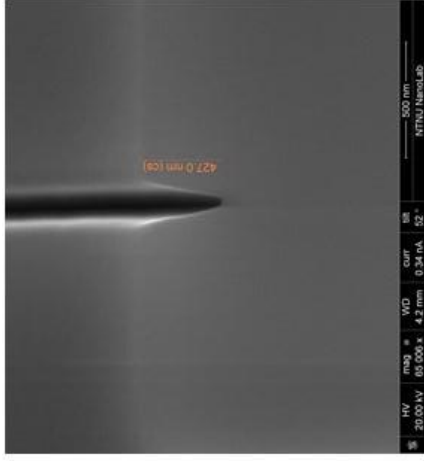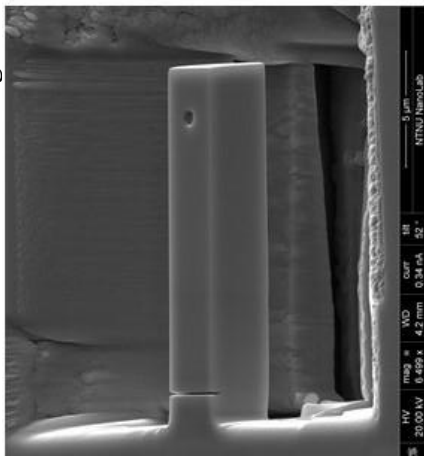
Cantilever 10: After bending (Air)
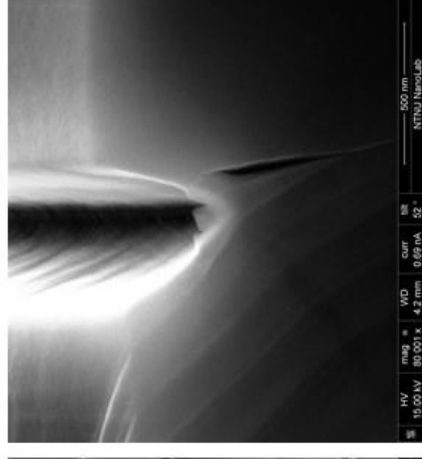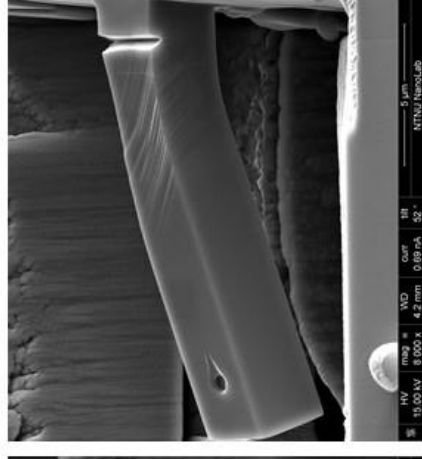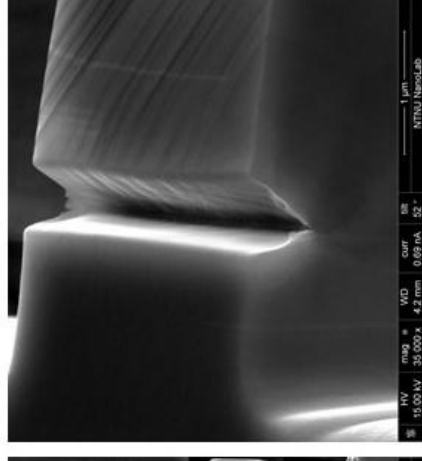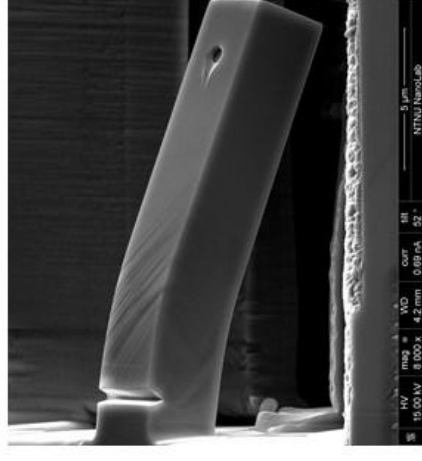
**Pure Ni**

Cantilever 1: Before bending
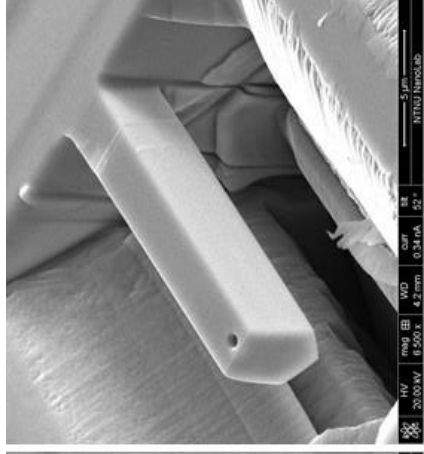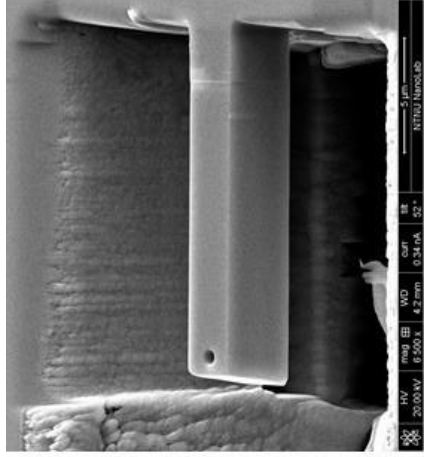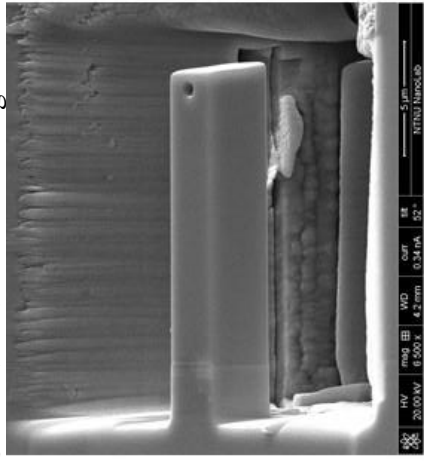


Cantilever 1: After bending (Air)
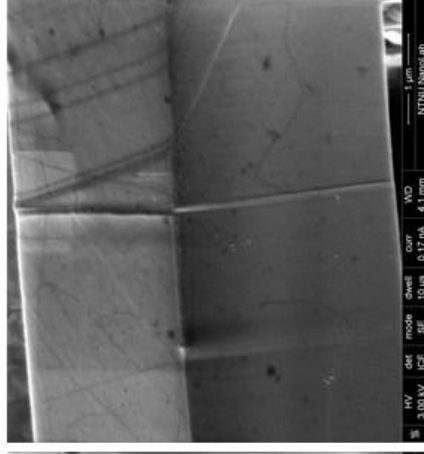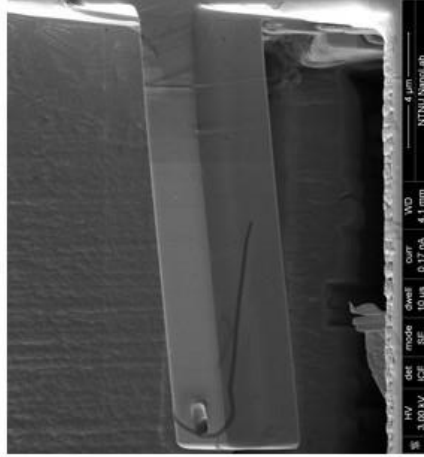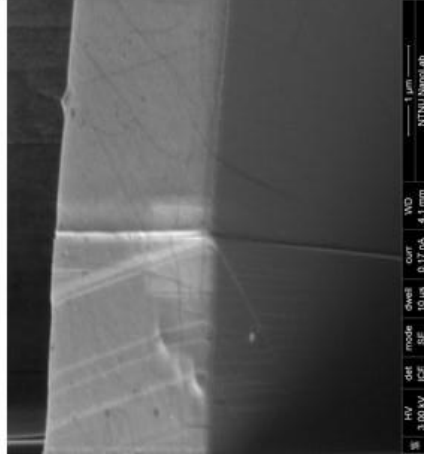
Cantilever 2: Before bending
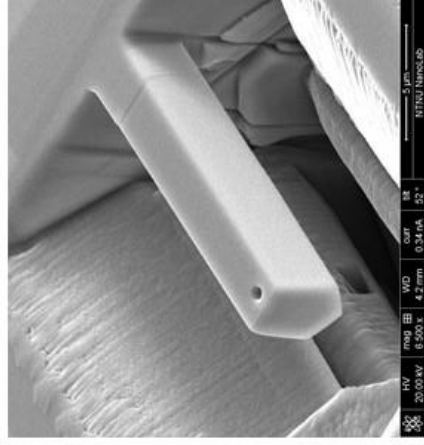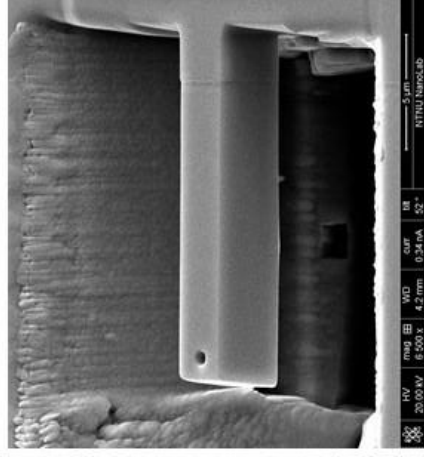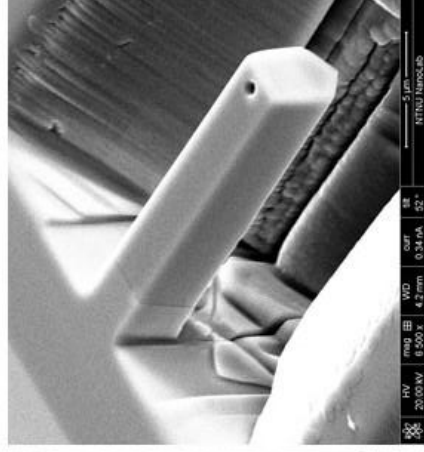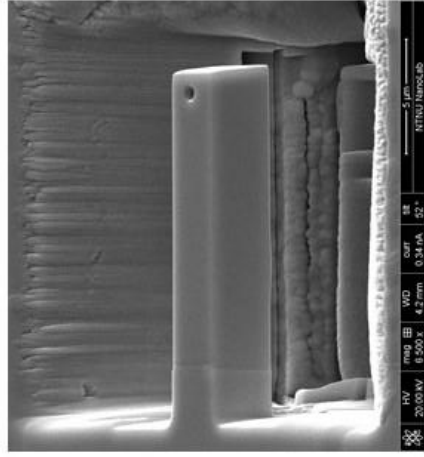
Cantilever 2: After bending (In-situ, 1 hour of H charging)
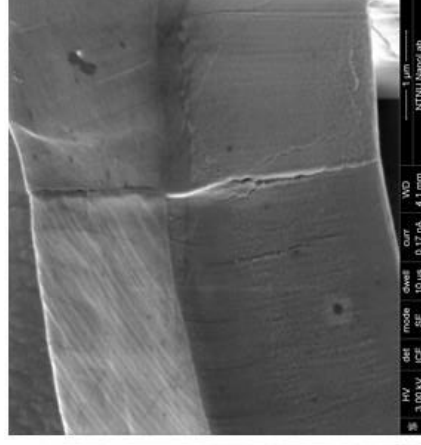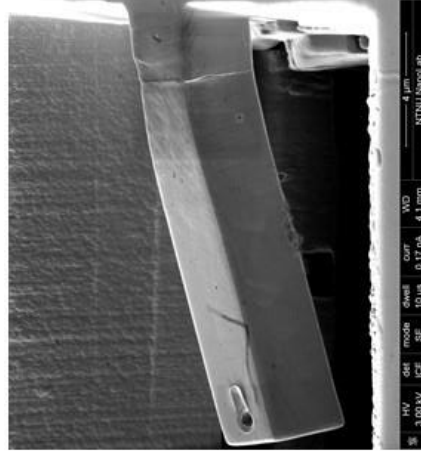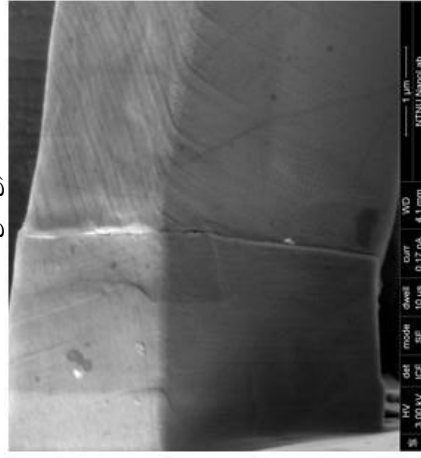
Cantilever 3: Before bending
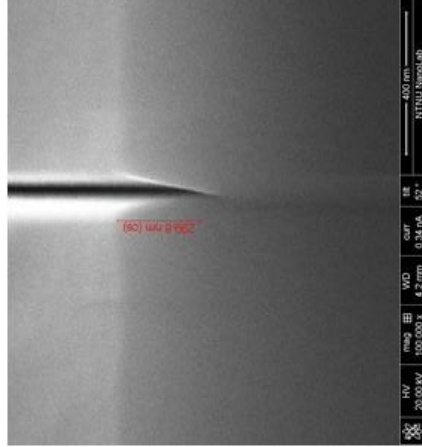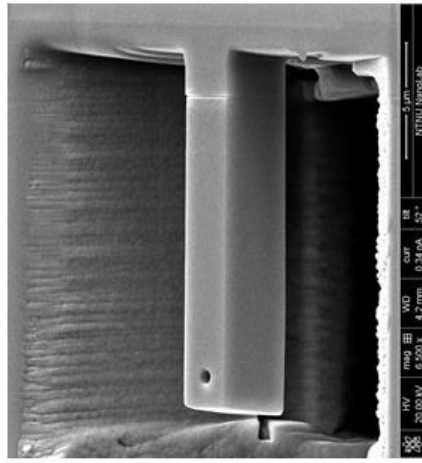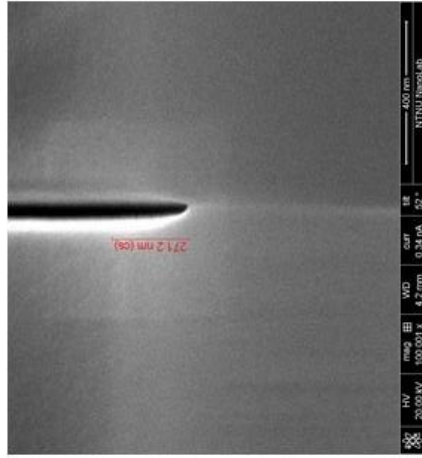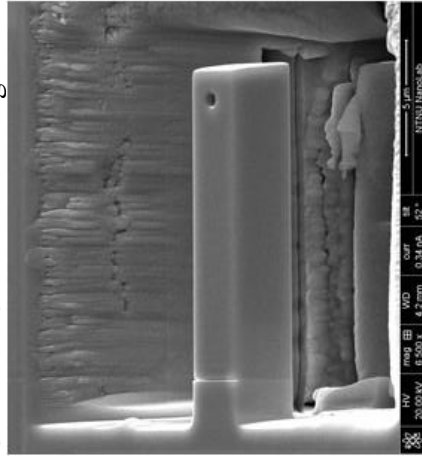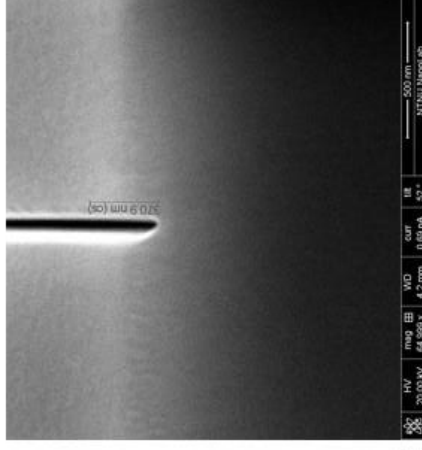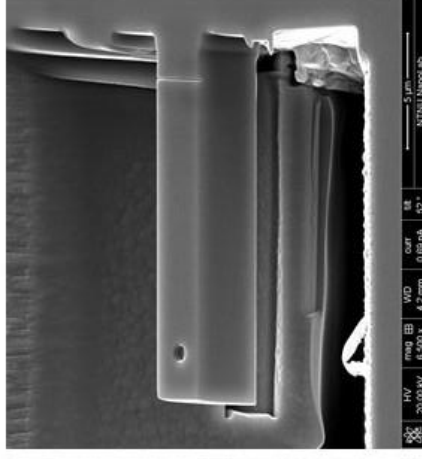


Cantilever 3: After bending (Air)
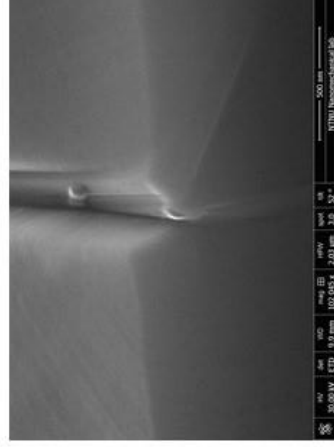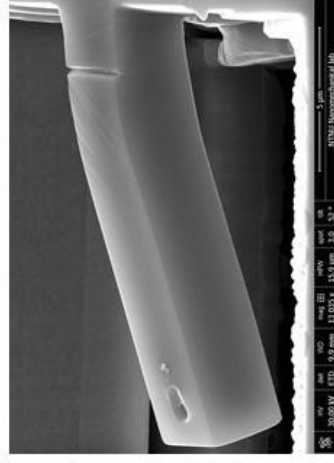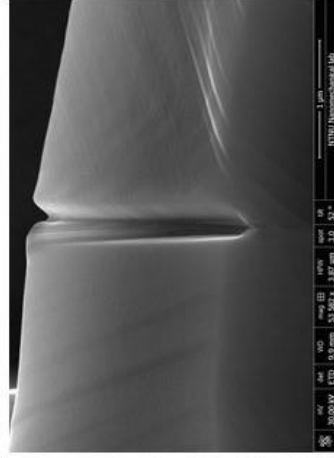
Cantilever 4: Before bending
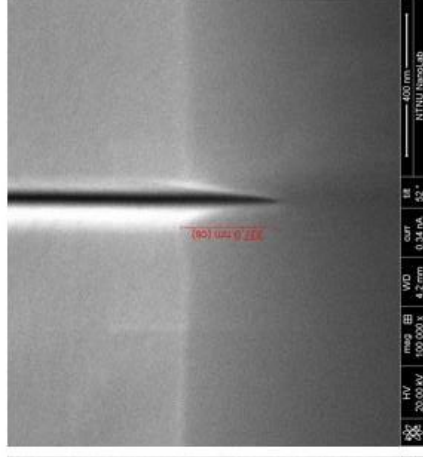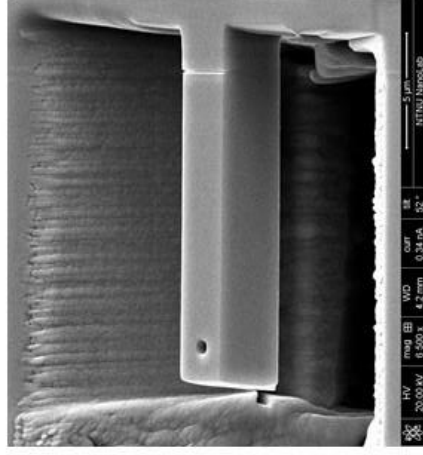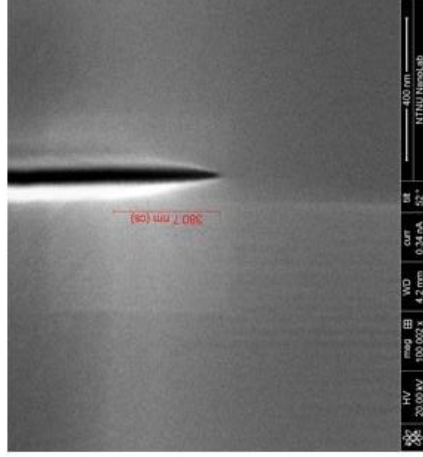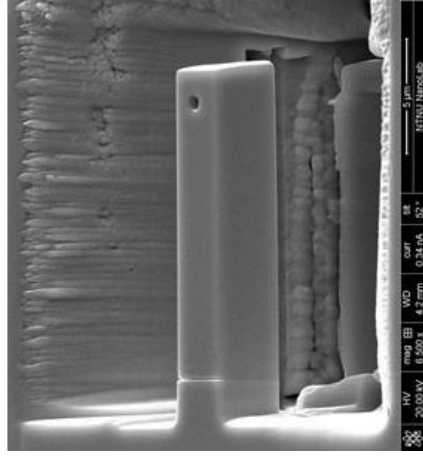
Cantilever 4: After bending (Air)
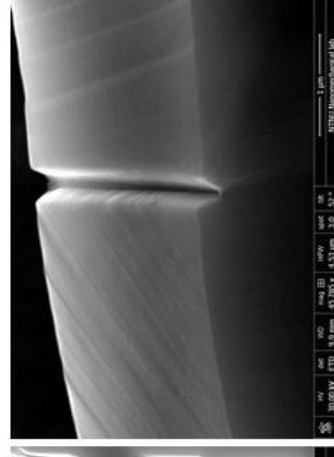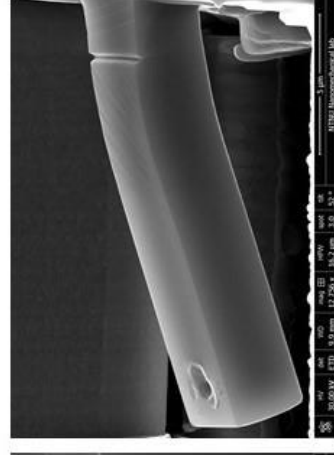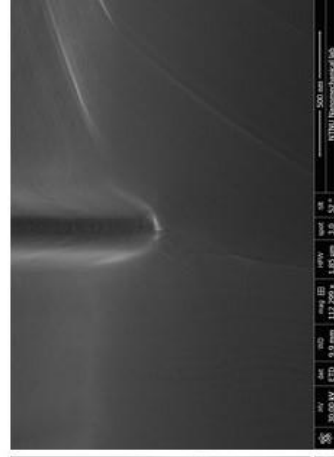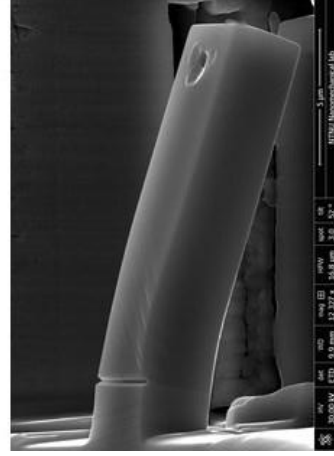
Cantilever 5: Before bending
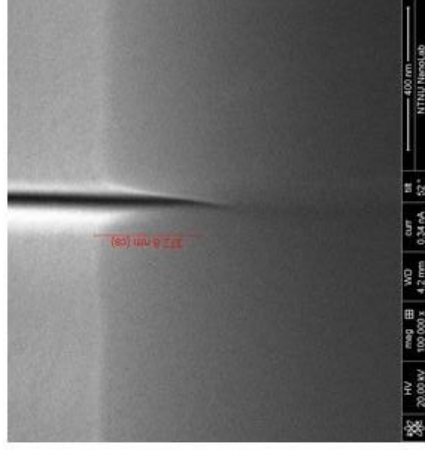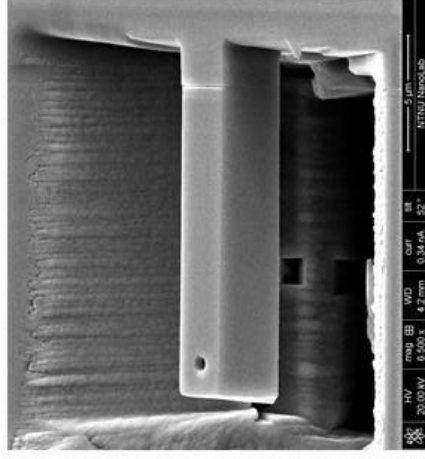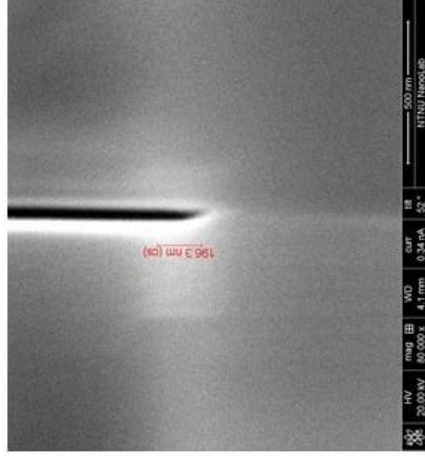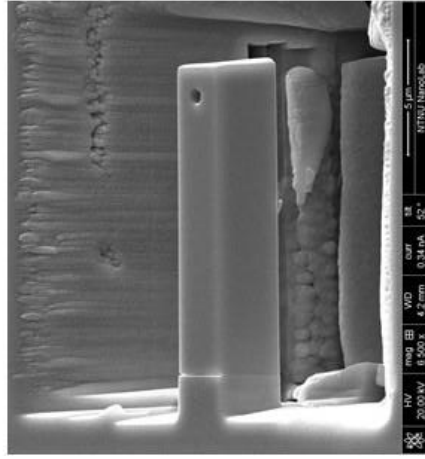


Cantilever 5: After bending (Air)
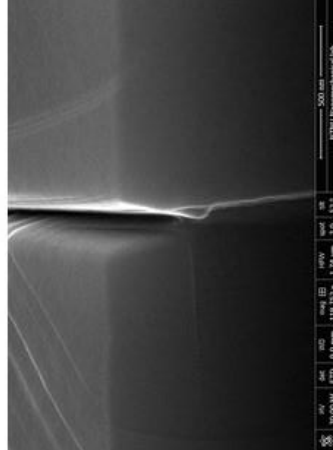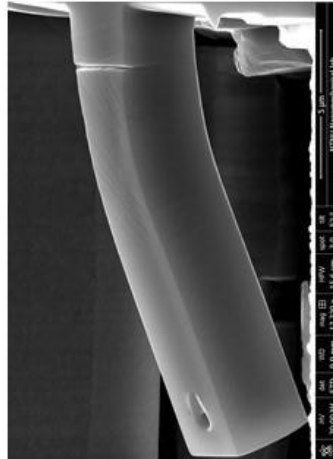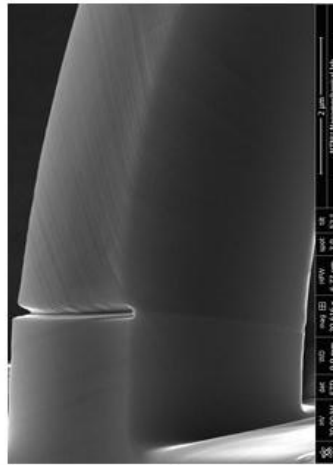
Cantilever 6: Before bending
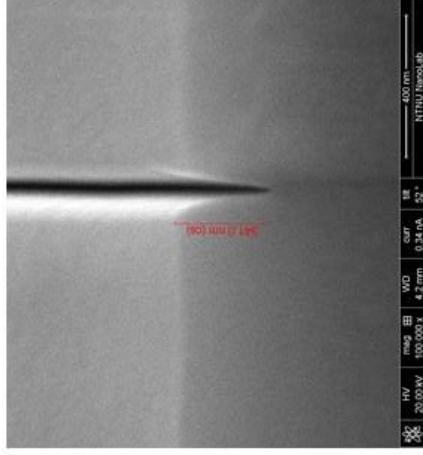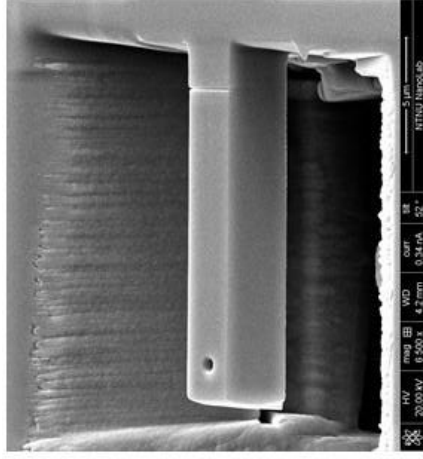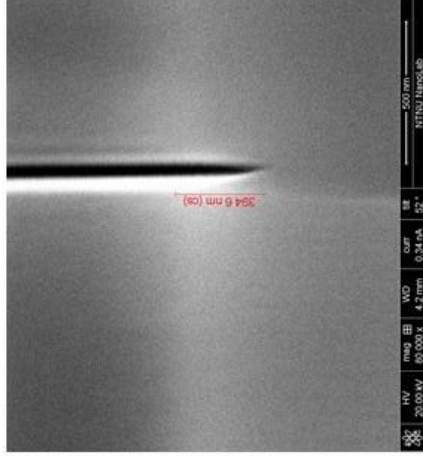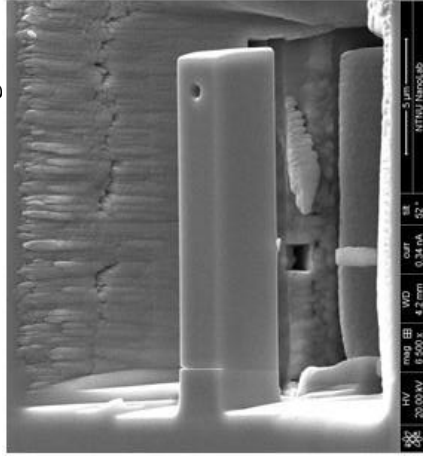


Cantilever 6: After bending (In-situ, 2 hours of H charging)
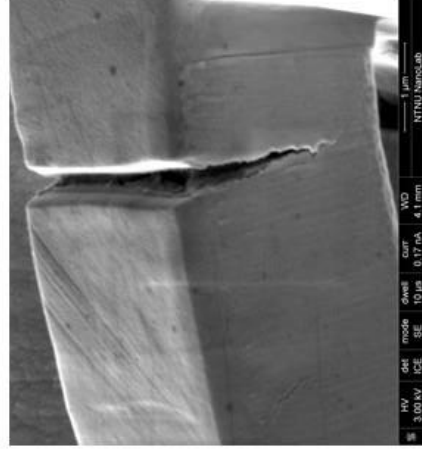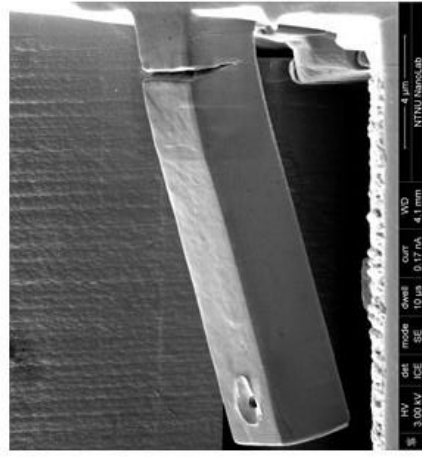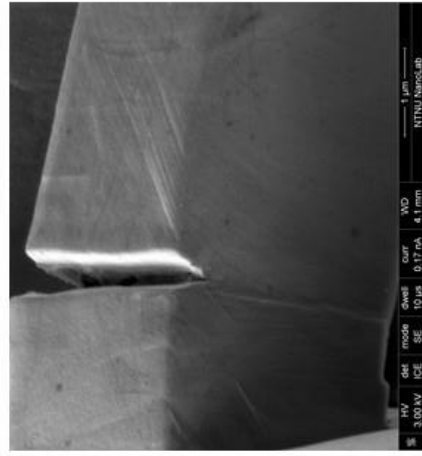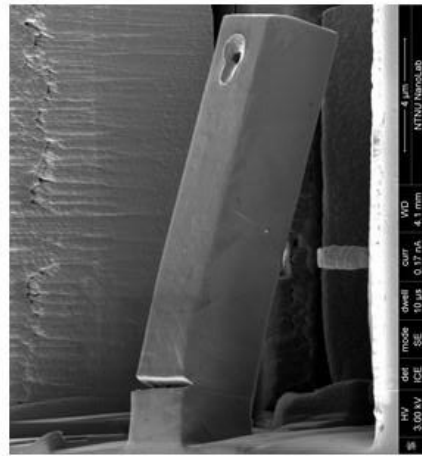
Cantilever 7: Before bending
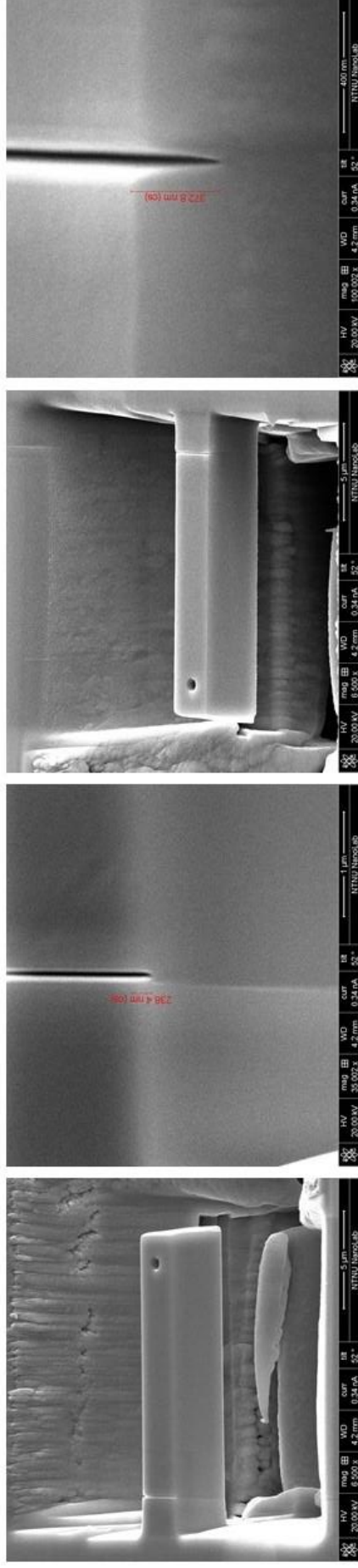


Cantilever 7: After bending (In-situ, 3,5 hours of H charging)
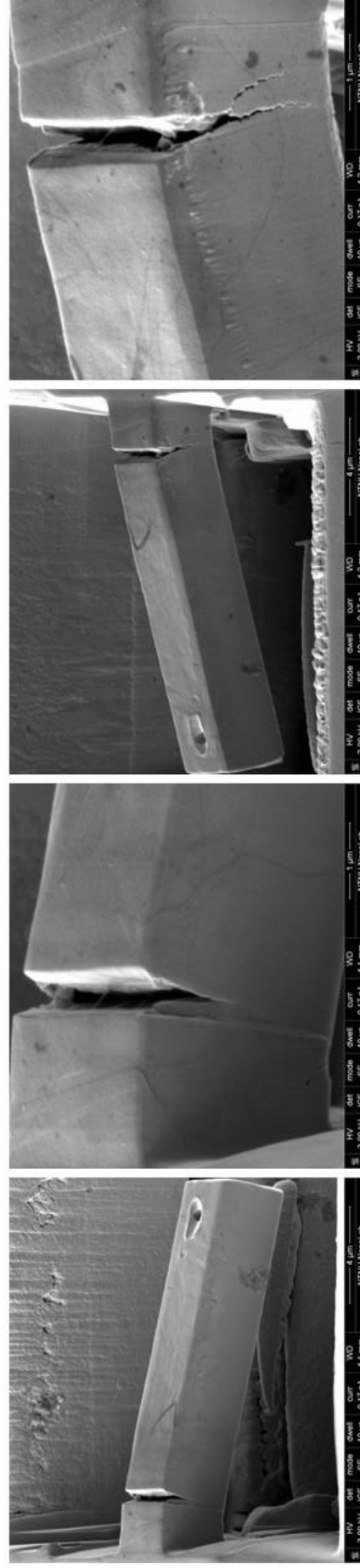
# Ni725 Precipitation hardened

Cantilever 1: Before bending
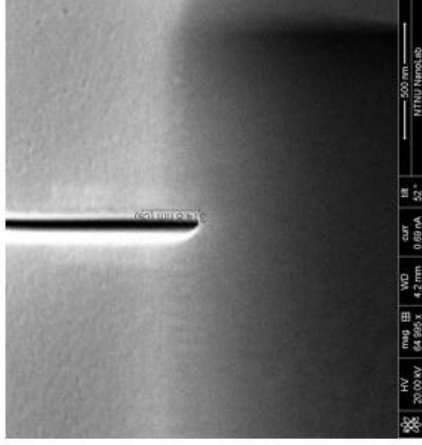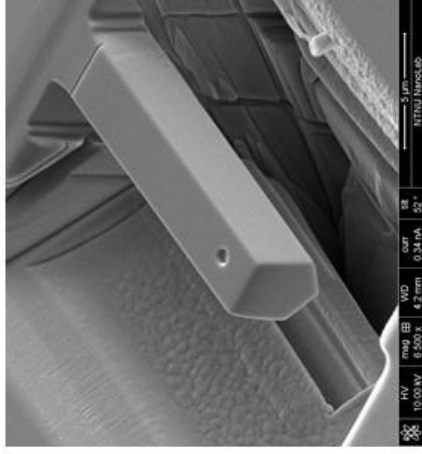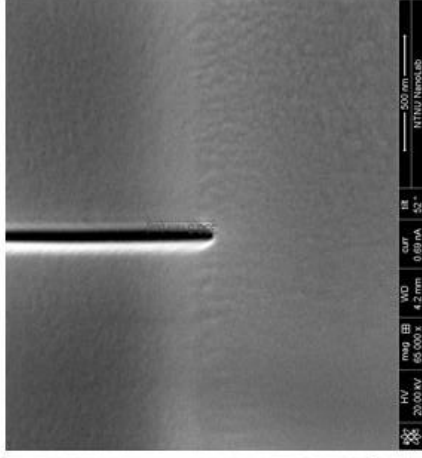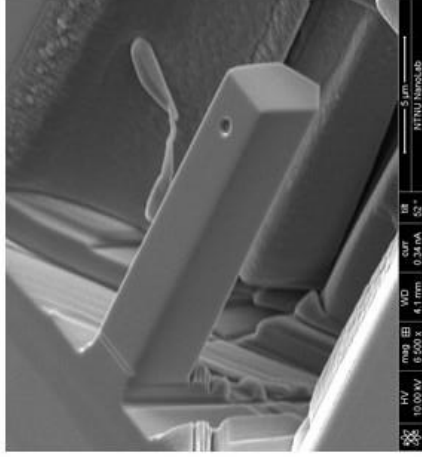


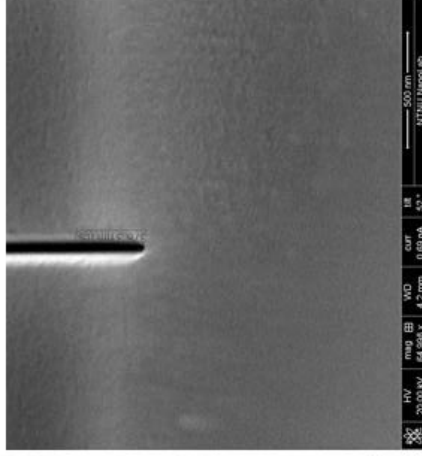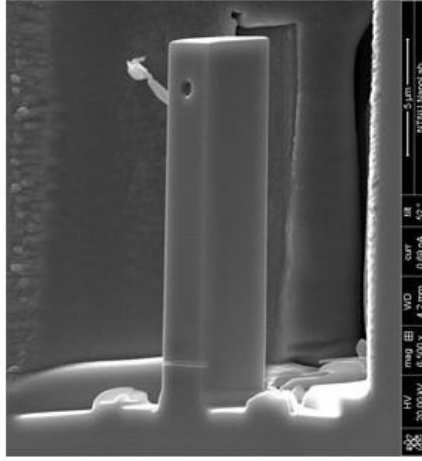Cantilever 1: After bending (Air)
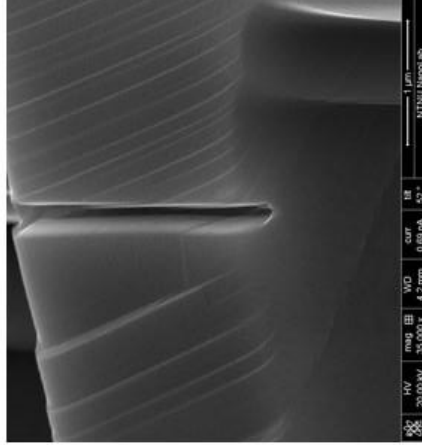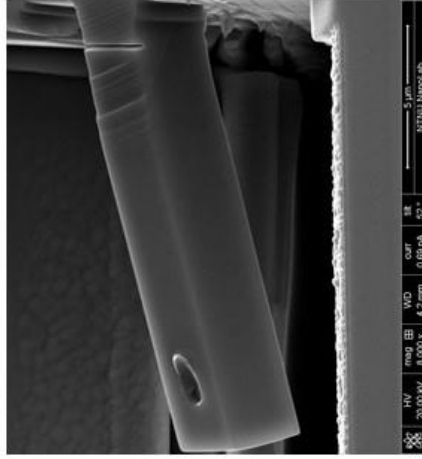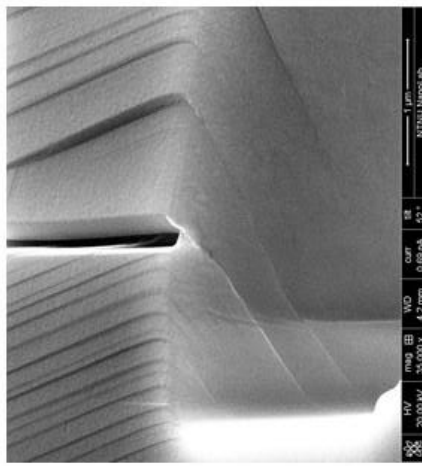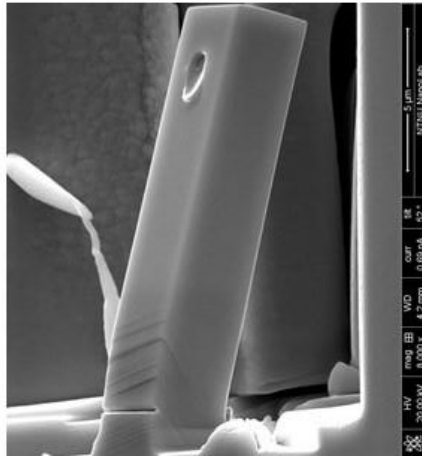
Cantilever 2: Before bending
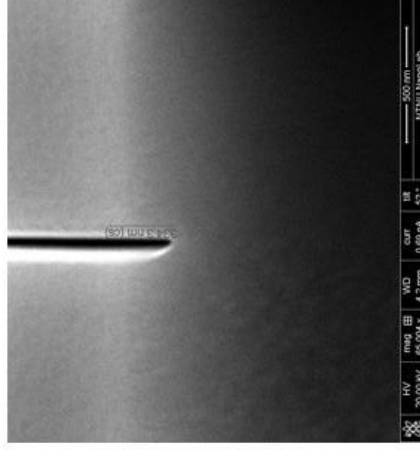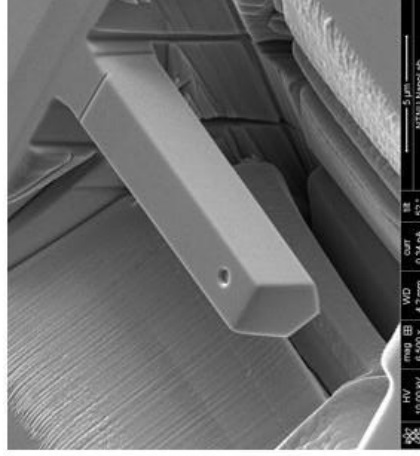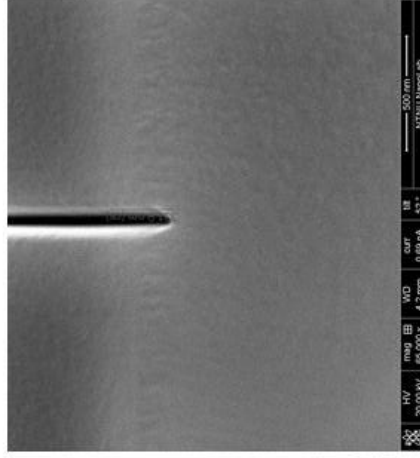
Cantilever 2: After bending (Air)

Cantilever 3: Before bending

Cantilever 3: After bending (Air)